STUDIES OF ICE FORMATION BEHAVIORS OF UPPER TROPOSPHERIC AEROSOL AND THEIR CHEMICAL COMPOSITIONS BY CONTINUOUS FLOW THERMAL DIFFUSION CHAMBER

By

Yalei Chen
and
Sonia M. Kreidenweis

Funding Agency:
National Science Foundation (NSF)
National Aeronautics and Space Administration (NASA)
NASA Earth System Science Fellowship

Colorado State University

DEPARTMENT OF ATMOSPHERIC SCIENCE

PAPER NO. 688

STUDIES OF ICE FORMATION BEHAVIORS OF UPPER TROPOSPHERIC AEROSOL AND THEIR CHEMICAL COMPOSITIONS BY CONTINUOUS FLOW THERMAL DIFFUSION CHAMBER

by

Yalei Chen

Department of Atmospheric Science

Colorado State University

Fort Collins, Colorado

NSF

under grant # NSF ATM 93-11606 and ATM 96-32917

NASA

under grant # NAG-2-924

NASA Earth System Science Fellowship

under contract # NGT5-30001

October, 1999

Atmospheric Science Paper No. 688

ABSTRACT

STUDIES OF ICE FORMATION BEHAVIORS OF UPPER TROPOSPHERIC AEROSOL AND THEIR CHEMICAL COMPOSITIONS BY CONTINUOUS FLOW THERMAL DIFFUSION CHAMBER ABSTRACT

Studies were conducted to investigate ice formation by aerosol particles at upper tropospheric conditions. The continuous flow thermal diffusion chamber (CFD) was used in both field and lab experiments to determine the conditions for the onset of ice formation in ambient and lab aerosols. After confirming the capability of the CFD to separate ice nucleating particles (IN) from non-IN, we collected samples of both IN and non-IN from the upper troposphere (UT) and the lower stratosphere during the 1996 NASA SUCCESS airborne field campaign. The chemical compositions of these particles were measured by electron microscopy, an individual particle analysis technique. From these results, as well as previous studies, ammoniated sulfates, sulfuric acid, and soot particles with different coatings were selected as representative UT aerosols for further laboratory investigation of their ice formation behaviors.

In controlled laboratory studies, the phase states of $(NH_4)_2SO_4$ and NH_4HSO_4 particles were found to have important impacts on their ice formation capabilities. Dry $(NH_4)_2SO_4$ particles nucleated ice only at high relative humidity with respect to water at temperatures between -40°C and -60°C. Ammonium sulfate particles that entered the diffusion chamber in a liquid state froze by homogenous freezing at relative humidities that were 10% lower than where ice nucleated on dry particles. Likewise, crystalline or partially crystallized (as letovicite) NH_4HSO_4 particles required higher relative humidities for ice nucleation than did initially liquid bisulfate particles. Based on our observations, 0.2 μm particles composed of either ammonium sulfate or bisulfate in a liquid solution

freeze at lower RH at UT temperatures than do 0.05 μm sulfuric acid aerosol particles. The results indicate that, for liquid droplets, the size effect may be more important than the degree of ammoniation of the sulfate compound.

Soot particles with different coating treatments were investigated in a similar manner as the sulfates. Submicron particles of commercial soot were coated with H_2SO_4 in amounts of zero to several percent by weight. Untreated soot particles showed activity as deposition/sorption ice nuclei; and soot particles with approximately one monolayer equivalent coating of sulfuric acid froze at humidities slightly higher than those of untreated soot. These observations suggest that dilution of sulfuric acid was required before homogeneous freezing. Heterogeneous freezing was observed on particles with multilayer coverage at cold temperatures ($<$ -53°C). We also generated soot particles by combustion of jet fuels and examined the freezing behavior of 0.05 μm monodisperse particles. The jet fuel soot particles contain about 10% by weight soluble matter, and did not freeze below 95% RH. Similarities existed in the ice formation behaviors of these jet fuel soot particles and 0.016 μm pure sulfuric acid particles.

These laboratory results suggest that small solution droplets, with diameters of several hundredths of microns, require relatively high humidity to freeze homogeneously, and are therefore unlikely to be the particles that form cirrus clouds with continental origins. Dry crystals of sulfate form ice near water saturation. Sulfuric acid coating changes the ice formation properties of soot particles dramatically. With multilayer sulfuric acid coating, soot particles initiate homogeneous freezing at cirrus cloud conditions at cold temperatures. This suggests a heterogeneous nucleation pathway for continental cirrus formation. Pure soot particles and those with a small amount of sulfuric acid coating, like fresh aircraft exhaust, only form contrails near water saturation.

ACKNOWLEDGMENTS

Over the last five years, so many people have helped me in some way that to list them all here individually would take several pages. First and foremost, my advisor Sonia Kreidenweis has been a tremendous source of support, scientific ideas, and encouragement over the years. I received full support and lots of advice from Dave Rogers and Paul DeMott to explore the field which I initially was not familiar with. Without their inputs, the collaborative work presented in this dissertation would not have been accomplished.

My committee members, Jeff Collett, Wayne Schubert, and Terry Lenz must also be thanked for undertaking the enormous task of reviewing this dissertation and providing the feedback necessary to greatly improve the quality of this research. The invaluable assistance of Brian Jesse, Lynn McInnes, and Ann Middlebrook through the construction of the CFD, electron microscopy analysis and construction of the sulfuric acid generator are greatly appreciated.

This research would not have been possible without the generous support of several funding agencies. Over the last five years, my work has been supported by the National Science Foundation (Grants ATM93- 11606 and ATM96-32917), the US National Aeronautics and Space Administration (Grant number NAG-2-924) and between 1996 and 1999 by the NASA Earth System Science Fellowship (#NGT5-30001).

TABLE OF CONTENTS

LIST OF FIGURES

LIST OF TABLES

Chapter 1

INTRODUCTION

Atmospheric aerosol particles, also called airborne particulate matter, may be solid or liquid phase. The definition generally excludes hydrometeors, *i.e.*, raindrops and ice particles. Most particles are invisible to the naked eye, ranging from clusters of a few molecules to particles 100 μm and larger [Pruppacher and Klett, 1997]. Atmospheric aerosol particles play important roles in visibility degradation and climate change [Baker, 1997]. The direct impact on climate is the reflection of significant portions of solar radiation back to space. Indirectly, they are important for the formation of clouds, and their optical properties [Charlson *et al.*, 1992]. The indirect effect of aerosols on cloud coverage and cloud optical properties, especially in the upper troposphere and lower stratosphere, still remains a large uncertainty in atmospheric global climate modeling. In high clouds, low temperatures require relatively less water vapor pressure to create a high relative humidity environment, and super-cooled water droplets cannot exist at equilibrium under such conditions, while the ice phase predominates. Ice formation by aerosol particles and the associated effects on climate have received considerable attention in atmospheric science research recently.

This work focuses on the experimental study of ice formation behavior in the upper troposphere and lower stratosphere. First, a proof-of-concept experiment was used to test the capability of the instrument to be used, the continuous flow thermal diffusion chamber (CFD), in detecting ice crystals. Then this technique was combined with other chemical analysis techniques to conduct field measurements of heterogeneous ice nuclei in the upper troposphere and lower stratosphere. Based on the field measurements of cirrus clouds, contrails(condensation trail), and aircraft exhausts, experiments were conducted using ammoniated sulfate, sulfuric acid, and soot particles in our laboratory instruments, including both heterogeneous and homogeneous ice formation behaviors. Therefore this

dissertation is organized as follows. This chapter discusses aerosol production processes in the upper troposphere, particle physical and chemical characteristics, and their relationship with cirrus cloud formation. Studies of aircraft exhaust and contrail ice formation are also reviewed. Section 1.1 presents the theories, observations and questions about upper tropospheric aerosols in previous studies. Heterogeneous ice formation nuclei, cirrus clouds, and aircraft exhausts and contrails will be discussed in sections 1.2, 1.3, and 1.4. Since this dissertation mainly focuses on laboratory studies, a brief description of the instrumentation is included in Chapter 2, primarily the CFD. The CFD was used for all the field observations and the laboratory measurements. Individual particle analysis by electron microscopy and the design of a five-jet impactor for ice crystal collection are also discussed in that chapter.

In Chapter 3, results from the proof-of-concept experiments are discussed. The experiments validate the capability of the CFD to separate ice nucleating particles (IN) from non-IN aerosol particles. Chapter 3 also describes procedures for operating the instrument, and how to collect, handle and measure the ice crystals/IN. In Chapter 4, the results of individual particle analyses of IN and total ambient aerosol particles are presented for the samples collected during the SUCCESS (SUbsonic aircraft: Contrail and Cloud Effects Special Study) field campaign. Chapter 5 presents the results of ice formation studies on ammoniated sulfate and sulfuric acid particles, designed to clarify how cloud condensation nuclei (CCN) particles behave under cirrus cloud conditions. Chapter 6 describes experiments using soot particles under upper tropospheric conditions. The purpose of this study is to simulate the formation of aircraft contrails in the upper troposphere, and to provide more laboratory evidence for assessing their impacts on global climate.

Some numerical calculations are included in this work, such as model simulation of ice formation inside the CFD and the homogeneous nucleation rate of solution drops under the experimental conditions. The calculations are presented in individual chapters as needed. In Appendix B, the precision and uncertainty analyses are conducted on the technique we used in all our experiments. The results are summarized and suggestions are given for future work in Chapter 7.

1.1 Properties of aerosols and individual particle analysis

In the atmosphere, sources of aerosol particles can be categorized into two types, natural and anthropogenic or man-made sources. Natural sources are the major ones by mass, and include sea salt and continental soils. Anthropogenic sources have become more significant since the Industrial Revolution and the rapid growth of pollution. In most cases, aerosol particles represent a mixture of substances from several sources; any specific component may have more than one origin. The roles aerosols play in the atmosphere are decided by many factors, including the phase state, sizes, number concentrations, and chemical compositions, as well as the source locations. Through convection and turbulent diffusion, aerosols from surface sources in the boundary layer can be brought up to different altitudes in the troposphere. A recent study [Chen *et al.*, 1998] shows that some aerosol particles in the upper troposphere can be identified as originating from the surface. With gas-to-particle conversion, new aerosol particles are formed in the atmosphere.

Aerosol particles are one of the essential factors in the cloud formation process since they serve as nuclei for drop and ice crystal formation [Pruppacher and Klett, 1997]. In the absence of CCN or IN, much higher humidities or lower temperatures are required for homogeneous nucleation, droplet growth, and ice formation. Therefore, an understanding of cloud forming processes in the atmosphere requires knowledge of the physical and chemical characteristics of the atmospheric aerosol.

The concentration of aerosol particles varies from time to time and place to place. Besides the rate of emission from the source, the strength of convective and turbulent diffusive transfer rates, the efficiency of removal mechanisms, and the meteorological parameters strongly change the vertical and horizontal distribution patterns. Observations indicate that the concentration usually decreases with altitude. 80% of the total aerosol mass is estimated to be within 1,000 m of the earth surface. This is the combined result of distance from the surface as the major source, as well as varying intensity of removal processes through the atmosphere. In the horizontal dimension, the concentration of aerosols tends to decrease away from the continents because there are more and stronger production processes over land. The overall distribution of aerosols shows the concentration in the

northern hemisphere is higher than that in the southern hemisphere, and the maximum concentration occurs in the area between 30° and 60°N [Pruppacher and Klett, 1997].

Studies on the detailed vertical structure of the number concentration of aerosol particles can be traced back to the 1960s by Selezneva [1966] on the continental aerosols over U.S.S.R, and by Isaac and Daum [1987] over Ontario, Canada. For altitudes above 5 to 6 km, the tropospheric concentration tends to be stable between 50 to 500 cm^{-3}. Pruppacher and Klett [1997] define these concentrations as the tropospheric background.

The vertical patterns of chemical species are complicated because of the complexity of production and removal pathways. One example is that the cloud condensation process removes the soluble particles through precipitation as the cloud is formed. Average conditions can be complicated by emissions from anthropogenic sources that alter the vertical profile regionally. Generally, aerosol particles can be distinguished into three broad categories: (1) water-soluble inorganic salts (electrolytes); (2) water-insoluble minerals of crustal origin; and (3) organic compounds, both water-soluble and insoluble [Warneck, 1988].

Starting from almost the same time as the concentration measurements of vertical profiles of total aerosol particles, sulfate and chloride were measured over different locations [Twomey, 1955; Byers *et al.*, 1957; Georgii *et al.*, 1971] on the earth surface. These observations confirm the efficient removal of soluble aerosol particles by clouds, as well as the sulfate production process inside cloud droplets. Most of the early measurements were based on the wet-chemical analyses of aqueous extracts of aerosol samples, therefore the results were reported as the presence of anions such as sulfate, nitrate and the halides, and of cations such as ammonium and the ions of the alkali and alkaline earth elements. Sulfate is the most conspicuous constituent of all continental aerosols with mass fractions from 22-45%. Of the cations, ammonium is the principal one associated with sulfate in the continental aerosols, corresponding to a composition intermediate between NH_4HSO_4 and $(NH_4)_2SO_4$ [Reiter *et al.*, 1975a,b, 1976, 1978]. Similar high fractions of sulfate occur in the Antarctic [Maenhaut and Zoller, 1997]. In the atmospheric chemistry program of the International Arctic Ocean Expedition 1991 (IAOE-91), Maenhaut *et al.*[1996] found that

typical anthropogenic metals (*e.g.*, Zn, As, and Sb) were predominantly associated with the coarse mode (>2 μm in diameter) in the Arctic aerosol. Based on trajectory analysis, they concluded that the high concentration of metals and crustal elements in the aerosol particles is the result of local mechanical windblown generation from river effluent materials. Elevated concentrations of non-seasalt sulfate were also found over the open water, and the main source was anthropogenic. Due to the limitations of analysis techniques, a long sampling time was required to have enough sample for extraction, only ground based measurements could be conducted, and it was impossible to measure the chemical composition variation of aerosol particles with altitude. As instrumental techniques developed in the last thirty years, such as neutron activation analysis, atomic absorption spectroscopy, proton-induced X-ray emission (PIXE), mass spectroscopy and electron microscopy micro-analysis, more complete analysis of the inorganic and organic chemical composition became possible.

The aerosol particles in the upper troposphere and lower stratosphere are important to the earth-atmosphere climate system because they scatter and absorb both incoming solar and outgoing terrestrial radiation. Additionally, they also change the formation and microphysical properties of high altitude clouds, such as cirrus and wave clouds, which impact the earth energy budget even more strongly than the aerosol particles alone. As a subset, IN specifically catalyze the formation of ice in supercooled clouds, and affect the evolution of these clouds [DeMott *et al.*, 1997]. To measure the components of single aerosol particles at high altitude, such as in the upper troposphere and lower stratosphere, particles must be collected by impactor, for either chemical reaction to generate a special pattern for morphological analysis, or individual particle micro-analysis to identify the chemical compositions. There are not many reports of single-particle chemical composition of IN and aerosols in the upper troposphere and lower stratosphere in the literature. With a collection substrate coated by $BaCl_2$, Bigg [1977] found that sub-micron sulfuric acid particles are dominant by number in the upper troposphere. This was later confirmed [Yamato and Ono, 1989; Ikegami *et al.*, 1993; Hagen *et al.*, 1994; Sheridan *et al.*, 1994; Heintzenberg *et al.*, 1996]. Sheridan *et al.*[1994] found that the number concentrations of sulfuric acid

particles were up to 90% of the total near the tropopause at midlatitudes. In the vicinity of cirrus clouds over Colorado and Wyoming, the observations by Hagen *et al.*[1994] reported higher fractions of non-sulfate particles. Besides sulfate aerosol particles, Ba, Al, C and Ti were frequently detected in their samples, and related to aircraft emission. Assuming that the soluble material was sulfuric acid or ammonium sulfate, Podzimek *et al.*[1995] estimated that 30% or 40% of the mass fractions of large aerosol particles inside cirrus clouds in the same field program were soluble. Silicon, chlorine, barium, sulfur, calcium, and carbon were the most frequently detected elements in these large particles. Among these non-sulfate particles, soot-containing particles are of interest because of their light absorption properties. Pueschel [1996] reviewed theoretical and observational knowledge of stratospheric aerosols, emphasizing their formation and climate effects on global changes. He found that soot aerosol from aircraft amounts to only a number fraction of 1% of the sulfuric acid aerosol, and predicted that the fuel consumption of a future supersonic fleet will increase the stratospheric soot aerosol burden by a factor of 2-3.

Some field measurements suggest that sulfuric acid droplets and insoluble components are the most abundant particulate substances in the upper troposphere [Brock *et al.*, 1995; Hagen *et al.*, 1994]. During the NASA SUCCESS field mission of 1996, several investigators [Chen *et al.*, 1998, Twohy *et al.*, 1998, Talbot *et al.*, 1998] found a strong sulfur component of the aerosol and detected ammonia in both bulk and individual aerosol samples. High mass fractions of insoluble material from surface sources were also found, consistent with the measurements of Hagen *et al.*[1994]. Murphy *et al.*[1999] recently also noted the ubiquitous presence of organic components in upper tropospheric aerosols.

1.2 Ice nucleating particles and ice formation processes

From thermodynamic theory and observation, we know that large samples of bulk water will freeze to ice at 0°C. But this is not always true for small quantities of water, particularly in the case of cloud particle ice formation. In cirrus clouds, super-cooled water droplets can exist even at temperatures of - 40°C [Pruppacher and Klett, 1997]. The reason for this is the kinetic barrier of formation of a new phase from a meta-stable

original phase. The phase transition does not begin in a continuous manner, but needs a fluctuation spontaneously in time and space of temperature and density in the original phase, to overcome the barrier. There are two mechanisms to atmospheric ice formation in the natural world: one is to exceed the critical super-saturation of the vapor or critical super-cooling of water drops, and the other is to provide some special aerosol particles to initiate the ice formation process. These particles are called ice forming nuclei or ice nuclei. Ice formation with the help of IN is called the heterogeneous nucleation process, and formation without IN is the homogeneous ice formation process.

There are four modes of IN activity in heterogeneous ice formation: deposition, condensation freezing, immersion freezing, and contact freezing. If water vapor deposits directly onto particles as ice, it is called deposition nucleation. The deposition mode cannot happen below vapor saturation conditions relative to ice. Under super-saturation conditions, water vapor condenses onto particles to form droplets first, which then freeze. That is the process called condensation freezing. In the immersion mode, an ice nucleating particle enters a droplet above 0°C and as the temperature cools down low enough, an ice crystal is formed. Finally, IN can initiate a freezing process by contacting a super-cooled droplet. IN can act via one or more modes.

The role of ice nucleating aerosols in cloud ice formation has been a topic of continuing scientific interest for a number of years. Scientific review articles have identified this topic as especially interesting because the microphysical and dynamic properties of a supercooled water cloud change drastically as it converts to an ice cloud [Hallett, 1983; Beard, 1987; Cooper, 1991; Szyrmer and Zawadzki, 1997]. Little is known, however, about IN aerosol origins, concentrations and histories for a number of reasons: (1) IN measurements are difficult to perform or verify; (2) IN can activate through several different thermodynamic mechanisms; and (3) there is no generally accepted method for measuring IN [Vali, 1996]. Thus measuring the concentration of IN at different temperatures and supersaturations, determining the size and chemical composition of natural IN aerosols, and inferring their origins and production mechanisms have been primary challenges.

Several techniques are available that measure the concentration of IN active at a given temperature (or temperature and supersaturation). However, due to ice multiplication, the

concentration of ice crystals in "real" clouds is not always represented by the concentration of IN measured or expected in one to one relationships. Ice multiplication arises from the fragile structure of ice crystals: when they are broken apart via collision, each fragment can act as an IN individually. Furthermore, no single measurement technique can distinguish one particular mode from the other three ice formation modes. Expansion chamber techniques detect deposition and condensation freezing and assume that a one to one correspondence exists between the ice crystal concentration and IN concentration. A cold chamber can activate IN through deposition, condensation and contact modes. The drop-freezing plate measures immersion freezing and contact modes. The thermal-gradient diffusion chamber method with membrane filter processing includes the aerosol particles activated by deposition, condensation freezing and perhaps contact nucleation.

Based on observations in the 1950s and 60s, people inferred the properties favoring an aerosol particle serving as an ice forming nucleus. First of all, it should be highly water-insoluble since the presence of salt in solution lowers the freezing temperature. The second property is size. Aerosol particles in the submicron size range are less likely to be active as IN than larger ones because of the curvature effect. The other favorable properties include chemical bond orientation, crystallographic fit and active-site density (from the defects in the surface structure) to catalyze ice formation processes. The last three are not readily determined for natural aerosol particles. However, all these properties except size are directly related to the chemical properties of aerosol particles. Therefore chemical compositions of IN are a key to solve the mysteries of the heterogeneous ice formation process.

Due to the lack of specific techniques to detect different modes of IN, some researchers examined the central nucleus of natural ice crystals [Kikuchi *et al.*, 1982; Murakami and Kikuchi, 1982]. In all of the 62 particles they collected from three locations in Japan, Ca, K, S, Si, and Cl were the major elements, occuring in more than 50% of the particles. Al and Fe were the second most common group, in 30% to 50% of particles. The disadvantage of their approach is that the residue of ice crystals may not be the originating ice nuclei, therefore misrepresenting the IN compositions. In the worst case, these inclusions could

be captured during precipitation scavenging, but not from freezing nucleation. Gas phase absorption during precipitation adds more uncertainties. Nevertheless, these observations give us a clearer image of what could serve as IN. *In situ* measurements could help to reduce these artifacts [Ström *et al.*, 1994]. The approach used by Rosinski *et al.*[1986, 1987] was to collect simultaneous aerosol samples on Millipore and Nuclepore filters. The Millipore filters were processed in a thermal diffusion chamber to nucleate ice crystals and grow them to a visible size for counting. The Nuclepore filters were examined for particles using electron microscopy (EM) for size and energy dispersive spectrometer (EDS) for chemical composition. With this technique, they tried to separately measure IN under condensation freezing and deposition modes. Most of the IN were smaller than 0.5 μm in diameter in the deposition mode, and 6 to 8 μm in the condensation mode. These studies were unable to separate IN from the total population, but the elemental compositions showed that no obvious difference existed between submicron aerosol particles and those above 1 μm diameter. The connection between IN activity and particle size/chemistry was by association with the simultaneous samples, not by examining the IN particle. This is a tenuous deduction because it is well known that most of the atmospheric aerosols are not active IN, that is, they will not nucleate ice until the temperature falls substantially below -20°C. The same technique was used on cloud condensation nuclei [Rosinski and Morgan, 1991], but was vulnerable to some contacting mode or other artifacts brought into the experiments. The review by Szyrmer and Zawadzki [1997], after summarizing the present knowledge about biogenic and anthropogenic sources of atmospheric ice nuclei, concluded that we need a standardized technique and a more coordinated and systematic effort in this area to understand the fundamental questions.

The development of an instrument for measuring IN, a continuous flow ice-thermal diffusion chamber, has previously been reported [Rogers, 1988, 1994]. Here we report recent laboratory results that were performed at the Colorado State University Cloud Simulation and Aerosol Laboratory with three different versions of the CFD instrument.

1.3 Cirrus cloud and homogeneous freezing studies

Cirrus clouds occur at high altitudes. They are "detached clouds in the form of white, delicate filaments or white or mostly white patches or narrow bands. These clouds have a fibrous (hair-like) appearance, or a silky sheen, or both."[Houze, 1993] Cirrus clouds usually consist entirely of ice crystals, typically bullet rosettes, bullets, and columns. In mid-latitudes, the height of the cirrus cloud base is between 5-13 km. Temperatures in cirrus clouds are typically -35°C and colder. In a generating zone of cirrus clouds, ice particles are nucleated and grow to large sizes. They exit the generating zone, and enter into a sublimation zone, that is located below the generating level, in which the particles sublime as they fall. Weak updrafts in generating zones are on the order of a few cm s^{-1}. Lifetimes for cirrus clouds differ from type to type, ranging from 15-25 minutes for cirrus uncinus, to a much longer persistent and large coverage for cirrostratus [Young, 1993].

The climatic importance of cirrus clouds has been recognized for a long time. Cirrus clouds cover about 20% of the globe on average, and are believed to have profound impacts upon the planetary energy budget due to their radiative effects. Even though the radiative properties of cirrus in the infrared spectral region are of special interest, absorption of solar radiation by cirrus may also significantly influence the stratification of the upper troposphere. As noted by Liou [1986], high cirrus clouds are normally optically thin and nonblack. The influence of optically thin and nonblack cirrus on the radiation field of the earth-atmosphere system, and hence on weather and climate components, depends on both the solar and thermal IR radiative properties which, in turn, are modulated by the compositions and physical locations of the cirrus in the atmosphere. In order to assess the validity of cloud predictions from global general circulation models, and also, in general, to better understand the effects of cloud radiative forcing and feedback on climate, investigation of cirrus cloud properties is an urgent need [Sassen *et al.*, 1995]. The difficulty of the investigation is that cirrus clouds are difficult to detect and categorize due to their special compositions and locations in the atmosphere.

The radiative properties of a cloud are determined by the cloud microphysical characteristics, *e.g.*, ice crystal size, habit, phase, number concentration and distribution. At the

temperature and humidity of cirrus cloud formation, homogeneous freezing is one likely the way that ice crystals are nucleated. As CCN are lifted and deliquesced as solution droplets, the weak updraft provides them with more moisture as the ambient temperature lowers, resulting in more diluted solution droplets. The likelihood of homogeneous freezing is enhanced as the temperature lowers and humidity and dilution increase.

Our knowledge of the freezing behavior of aerosols that nucleate cirrus cloud particles is still uncertain. Several investigators propose that the formation of cirrus clouds involves ice formation in ammoniated sulfate aerosols, and suggest that homogenous freezing is one possible nucleation process [Sassen and Dodd, 1988; Heymsfield and Sabin, 1989; DeMott *et al.*, 1994; Jensen *et al.*, 1994; Tabazadeh and Toon, 1998]. Knowledge of the chemical state of sulfate and sulfuric acid aerosol particles is required to understand the physical process at cirrus cloud formation.

In relatively large "bulk" samples of aqueous ammonium sulfate solution, supercooled metastable states do not occur, and a phase diagram of the $(NH_4)_2SO_4$ -H_2O binary system can be constructed from the thermodynamic model of Clegg *et al.*[1998], as shown in Figure 1.1. In this plot, the deliquescence curve (a) and the ice curve (b) represent the temperatures required for crystalline dissolution and solution freezing, respectively. A liquid solution exists between (a) and (b), and their intersection at the eutectic (E) denotes the point of equilibrium between the three phases (crystalline, solution, ice). Within the solution regime, a decrease in temperature at a constant relative humidity will equilibrate with the ice phase at the ice line, if there are nuclei available for ice formation. An increase in relative humidity at a constant temperature within the solid crystal regime will lead to deliquescence of solute at the deliquescence line. Below the eutectic point, the liquid phase does not exist at equilibrium. For microscopic size samples, metastable liquid can occur, and the phase diagram is more complicated.

Metastable liquid can exist well below curve (b) because solution droplets supercool. It is a well-known fact that pure water droplets will not freeze at 273 K without help from ice nuclei, and remain as liquid as cold as 235 K [Pruppacher, 1995]. The energy barrier for ice embryo formation prevents water from freezing. The same things happen in solution

droplets. Where the metastable ice line resides on Figure 1.1 depends on solution effects and surface tension, as discussed further in Appendix A.2. Soluble substances decrease the freezing/melting point of a binary system as in curve (b). For sub-micron size particles, curvature elevates the vapor pressure over solution droplets through a reduction in the surface tension and thus affects the equilibrium composition and freezing temperature of small solution droplets. The net effect of all three factors is that small aerosol droplets require lower temperatures to freeze than are predicted for bulk solution at equilibrium.

To model cirrus clouds, Sassen and Dodd [1988] noted that in many laboratory studies of solution droplets, the depression of the homogeneous freezing point (ΔT_{hf}) scaled in proportion with the melting point depression (ΔT_m), or,

$$\Delta T_{hf} = \lambda \times \Delta T_m \tag{1.1}$$

In this expression, ΔT_m is positive and increases with the solute concentration in solution droplets, and λ is a coefficient that relates this bulk melting point depression with observed freezing point depressions in droplets. Equation (1.1) is purely empirical, based upon laboratory observations, and was found to apply independent of the size of droplet or the type of solute used. The value of λ for a particular solute was derived from the temperature at which the median of a population of drops froze. It is not evident why the droplet freezing point depression should be directly related to the bulk melting point depression, as assumed in equation (1.1), particularly since freezing is described by a kinetic theory whereas the melting point is a well-defined thermodynamic quantity. Nevertheless, the observations support this relationship, and Sassen and Dodd [1988] took this a step further and proposed that the proportionality constant λ was also valid for kinetic calculations of nucleation rate at temperatures other than the temperature at which a drop freezes instantaneously (nucleation rate, $J = \infty$). That is, it is assumed that the nucleation rate in a solution drop at any temperature T can be computed from classical nucleation theory for a droplet of pure water, except that all temperature-dependent properties must be evaluated at an "effective" freezing temperature, T^*, defined by

$$T^* = T + \lambda \Delta T_m \tag{1.2}$$

Since λ and ΔT_m are always positive, Equation (1.2) indicates that the effective temperature is always warmer than its actual temperature. Thus when T^* is used, as proposed by Sassen and Dodd [1988], in the expression for the homogeneous freezing rate of a pure water drop of volume V_d at temperature T, it will yield an estimate of the freezing rate of a solution drop of volume V_d held at temperature T. The solution drop will require a colder temperature to achieve the same nucleation rate as that in the pure water drop, or conversely, will have a smaller nucleation rate than the same-sized water droplet held at the same actual temperature.

The classical nucleation rate expression has terms dependent upon droplet size, density and surface tension, as shown in equation A.10, each of which is in turn dependent upon the droplet composition in equilibrium with the ambient relative humidity, which defines the water content of the solution drop. As described in Appendix A, the addition of solute to pure water is expected to have a net effect of lowering the homogeneous nucleation rate from that expected for pure water. The approach used here, as defined by Sassen and Dodd [1988], is to capture the composition dependence of the nucleation rate entirely through the use of T^* in place of T in equation A.10; the rest of the parameters to be input to the equation are those for pure water. One advantage of this concept is that one may use homogeneous freezing rates for pure water that have been empirically- or semi-empirically determined, and are generally accepted as more relevant than those predicted from classical theory, to compute the equivalent freezing rates for solution drops, without having to determine how the presence of solute should alter the details of the empirical freezing rate. This is what we will do in this work, preferring to use the homogeneous freezing rate for pure water, $J_{hf}(T)$, as parameterized by DeMott et al. [1994] over the classical theory. The fraction of solution droplets of volume V_d freezing in some increment of time Δt is then given by

$$F = 1 - exp[J_{hf}(T^*)V_d\Delta t] \tag{1.3}$$

λ is always positive, and further is typically found to be larger than one. A value of $\lambda = 1$ implies that the solution drop can freeze at a degree of supercooling, below its

homogeneous freezing temperature, equal to its bulk melting point, which from equation (1.1) and Pruppacher [1995] (for ΔT_{hf} of pure water) would be equivalent to a 1 μm pure water drop freezing at T = –40 °C. The concept (with $\lambda = 1$) is equivalent to the suggestion by Hallett and Lewis [1967] for quantifying the freezing conditions of sulfuric acid drops. Another way of looking at this is that the value of T^* for $\lambda = 1$, when put into the homogeneous freezing rate expression for pure water, depresses the temperature at which a certain freezing rate is achieved for the solution drop only as much as the bulk melting point depression. Classical theory does not readily explain why $\lambda = 1$ is not the typically-found value, but values of λ observed in laboratory studies of supermicron droplets with fixed composition range from 1.4 to 2.3 for various solutes [DeMott, 2000].

Our laboratory studies determined the freezing conditions for solution droplets of solutes of importance to cirrus cloud formation, in a size range of haze particles appropriate to the atmosphere. Freezing occurred while particles were freely suspended in air, and interacting with the surrounding vapor field. In this work, we will derive the appropriate values of λ that fit our own results, as well as the experimental results of various other investigators, to put the experimentally-determined freezing data on the same basis, regardless of whether different sizes of droplets were used in the studies. This is possible if the fraction of droplets frozen is reported, along with their size and composition, because these can be input to equation (1.3) in an iterative manner until the effective temperature, T^*, which fits the data is obtained. λ is then directly derived from T^* and knowledge of the melting point depression for the composition at which freezing occurred. In Figure 1.1, we show the freezing temperatures expected for a freezing fraction F=0.99 of ammonium sulfate particles with dry particle diameters of 0.2 μm that have adjusted in size and water content the relative humidity shown on the x-axis (*i.e.*, their size is computed via the Köhler equation). The droplet composition also determined ΔT_m, which may be calculated based on tabulated data or, as done here, using mole-fraction-based thermodynamic models [*e.g.*, Clegg *et al.*, 1998]. In Figure 1.1, two different λ values, each yielding the unique curve shown, have been assumed, to show the effect of a change in λ on the actual freezing temperature.

In metastable systems, crystallization of solute from solution (efflorescence) does not happen at the same humidity as deliquescence. Depending on the chemical properties, super-saturation is required to form a solid embryo without the presence of nuclei. Therefore the efflorescence effect broadens the region of meta-stable states for solution droplets [see, *e.g.*, Imre *et al.*, 1997].

Several investigators have recently reported results from experiments examining the low temperature phase transition of ammonium sulfate and sulfuric acid by different techniques. Bertram *et al.*[1996] measured the freezing curve of liquid sulfuric droplets versus temperature using Fourier Transform infrared (FTIR) extinction spectroscopy. They froze poly-dispersed sulfuric acid droplets with average diameter of 0.4 μmin a flow tube. The aerosol particles were super-cooled by about 35 K below the temperature at which the corresponding bulk material freezes, and the overall freezing mechanism is similar to that of the bulk solution ($\lambda \approx 1$). Cziczo and Abbatt [1998] used a similar apparatus to measure the temperature-dependent deliquescence, efflorescence and super-cooling behaviors of ammonium sulfate aerosol particles. The aerosol size distribution they used was lognormal, with a number mean diameter of 0.35 μm. The pure water supercools up to 39K before homogeneous freezing, while ammonium sulfate exhibited less than 39 K of supercooling ($\lambda < 1$).

Imre *et al.*[1997] used an electrodynamic balance to measure the freezing behavior of single sulfuric acid particles ranging from 5 to 10 μm in diameter. The freezing line generated is close to the icing point but $\sim$1 K lower. Koop *et al.*[1999] observed sulfuric acid particles freezing under an optical microscope. The sizes of particles they used were from 5 to 20 μm. The freezing temperatures obtained over one thousand droplets of H_2SO_4 were used to define the homogenous freezing line under supercooled conditions ($\lambda \approx 1.9$). Martin *et al.*[1998] presented results from experiments using a traditional method to measure the phase transformation in NH_4HSO_4 bulk solution. These data agree well with the prediction from Clegg's model [1998]. Further comparison among these data will be discussed later.

Most FTIR experiments cited above define the phase transition temperature as where the first presence of the ice characteristic absorbance is detectable in the spectra, which

corresponds to formation of ice embryos. "Onset conditions" measured this way may not be the conditions for ice crystal formation in real cirrus clouds, since as the embryo is formed inside droplets, most of the particle still exists as solution. The homogeneous formation of ice embryos inside super-cooled droplets is not the same as the complete conversion of water to an ice crystal. Different experimental configurations, aerosol sizes and concentrations, as well as the different instrument sensitivities may affect the selection of onset conditions. This may explain some of the discrepancies among the previous studies. Hence it is very important to define what the onset condition means, whether only a small number of particles or almost all of them transfer to ice phase. All measurements discussed above, except the one from Imre's group and those for bulk solution, worked with poly-disperse aerosol particles. Since nucleation and freezing are strongly dependent on particle volume, changing the curvature term in Köhler theory, size effects play an important role in ice formation. Therefore mono-disperse aerosol particles should be used to obtain unequivocal information of atmospheric relevance before simulating the aerosol population in atmosphere. To avoid the possibility of a heterogeneous nucleation contribution, it is necessary to isolate aerosol particles from contact with any support surface. These are the other two criteria proposed for measurements most relevant to the upper tropospheric conditions.

A complication in understanding the role of soluble aerosol particles in forming ice in cirrus clouds is the already mentioned fact that they may exist as liquid or dry aerosol particles, depending on the environmental conditions and their life history. Besides efflorescence, the possibility exists that chemically different crystallites may form in solution droplets as they dry or cool. These changes in phase state can impact the conditions of re-deliquescence and freezing of particles. Also, there is the possibility that crystallized particles may form ice directly by deposition nucleation. These various scenarios have been described by Tabazadeh and Toon [1998] and Martin [1998].

To focus on conditions most relevant to actual nucleation by soluble aerosol particles in cirrus clouds, we exposed monodisperse particles to ice supersaturation in a thermal gradient diffusion chamber. The particles remain suspended in the sample flow. Conditions

in the chamber are selected to be relevant to temperatures and humidities in the upper troposphere. The apparatus detects the fraction of particles forming ice crystals as a function of these conditions.

1.4 Aircraft exhausts and contrails - Soot particles in the atmosphere

In the previous section, we discussed homogeneous ice formation by ammoniated sulfate and sulfuric acid aerosol particles in the upper troposphere and lower stratosphere. Here we will look into ice formation initiated by another group of particles – soot particles, also called black carbon, elemental carbon or amorphous carbon.

Aircraft exhaust can form persistent contrails when the ambient conditions are favorable. In the upper troposphere and lower stratosphere, the radiative properties of persistent contrails are similar to those of cirrus clouds, with the same ambient humidity and temperature. The ice formation behaviors for contrails are different from those of cirrus clouds, because of the presence of soot particles from exhausts and the high water vapor supersaturations likely at initial formation. Even without formation of contrails, soot particles can still impact the global radiation budget; therefore, they are of interest for global climate modeling. During the SUCCESS campaign, carbonaceous particles were found in the upper troposphere and lower stratosphere, in both ambient aerosols and IN collected by TEM grids [Chen *et al.*, 1998; Twohy and Gandrud, 1998]. However, in-situ measurements of IN concentrations in aircraft exhausts and contrails do not show dramatic enhancements during the flights [Rogers *et al.*, 1998]. That raises the question, what kind of role do the soot particles play in the formation of contrails, and even in cirrus clouds?

The formation of atmospheric soot particles is from incomplete combustion, either natural or anthropogenic. The origin of soot particles in the upper troposphere can be the earth's surface, but is mainly from aircraft emissions at that altitude [Pueschel, 1995]. Based on the emission index of 0.07 g soot per kg of fuel burned by commercial air traffic, the soot aerosol concentration is in the order of a few tenths of a nanogram per cubic meter [Pueschel *et al.*, 1995]. That is consistent with the observations in the northern stratosphere of 0.6 nanograms per standard cubic meter [Pueschel *et al.*, 1992]. Pueschel

[1996] collected both soot and sulfuric acid aerosols by wire impactors mounted on ER-2 and DC-8 aircraft. The size distribution of aggregate soot particles observed with a field emission scanning electron microscope had a geometric mean radius of 0.04 μm, with a standard deviation of 1.4.

Pure soot particles are believed to be hydrophobic and insoluble; therefore, they are not good cloud condensation nuclei in the atmosphere. After mixing with or coating by soluble sulfate or sulfuric acid, water uptake becomed much easier than for bare soot particles. The presence of insoluble material makes heterogeneous freezing possible, changing not only the mechanism of ice formation, but also the ice crystal population. While evidence exists for the action of both homogeneous and heterogeneous ice formation by background aerosol particles in the upper troposphere [Jensen *et al.*, 1998; DeMott *et al.*, 1998], there remains much uncertainty regarding the fundamental hydration and freezing behavior of mixed soluble/insoluble aerosol particles.

Few studies on ice formation by soot particles exist at temperatures above - 40°C. DeMott [1990] froze monodisperse soot particles generated by burning of acetylene after activating them as cloud condensation nuclei. A size dependence of ice formation by freezing nucleation was found, and only a few percent of particles acted as IN heterogeneously. The particle size was around 0.1 μm in diameter. Recently Diehl and Mitra [1998] found freezing nucleation for nearly 100% of the large droplets ($\sim$200 to 400 μm) containing kerosene-generated soot particles suspended inside in a wind tunnel around -28°C. To eliminate size effects, both results were normalized by the total particle surface area of soot particles inside droplets, and those two results are more consistent with each other. One difference between these two experiments is the origin of the soot particles.

The content of sulfur varies in jet fuels, typically ranging from 100 to 1000 ppm in mass fraction [Busen and Schumann, 1995]. The maximum specification limit is 3,000 ppm by the American Society for Testing and Materials (ASTM) [1994]. Measurements conducted by Schumann [1996] show that part of the fuel sulfur is converted to sulfuric acid which nucleates with water vapor heterogeneously on soot or nucleates acid droplets homogeneously which then coagulate partly with soot. Therefore the amount of sulfuric

acid on soot particles from aircraft exhaust can be different from fuel to fuel and may result in different ice formation behaviors under low temperatures below -40°C. We conducted experiments to determine ice formation by amorphous carbon particles, coated with varying amounts of sulfuric acid, and soot particles created by burning of jet fuel in our laboratory. The results will be discussed in Chapter 6.

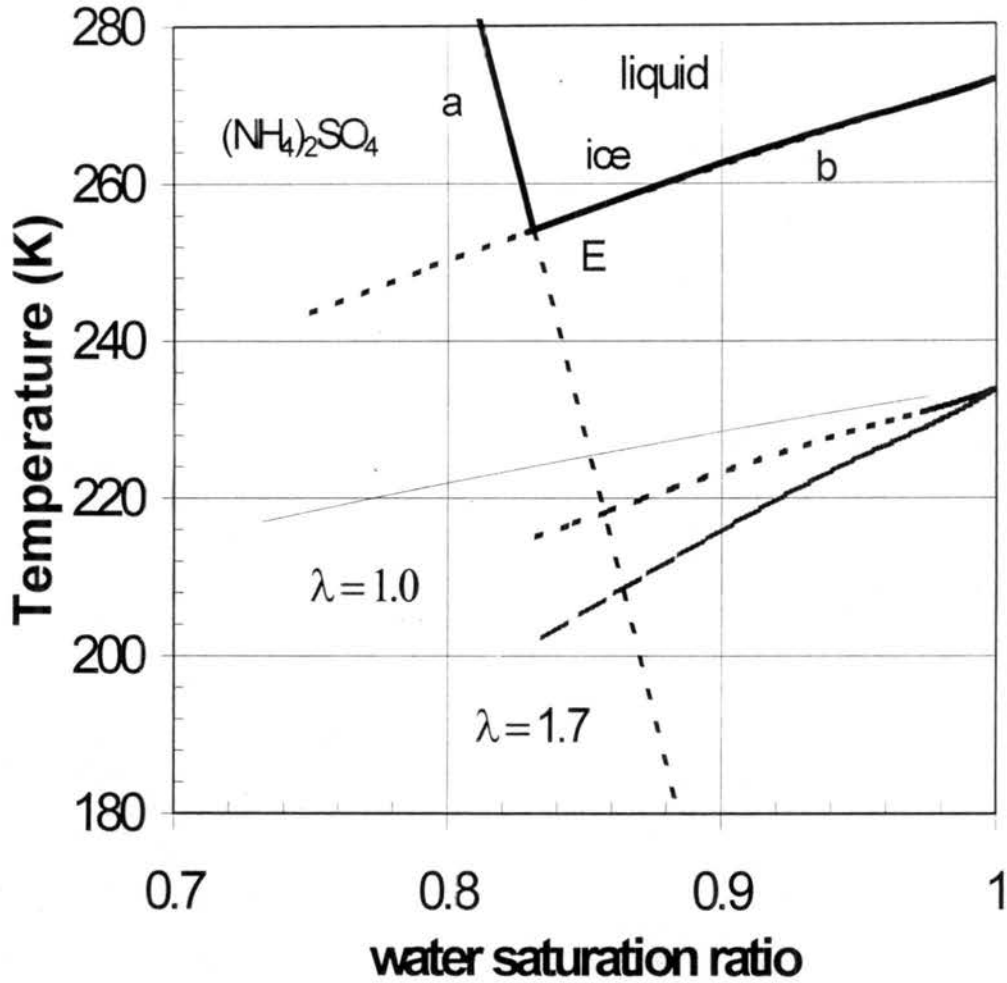

Figure 1.1: The thermodynamic phase diagram of $(NH_4)_2SO_4$-H_2O system. Curves a and b represent the deliquescence and ice lines. E is the eutectic point. Below the eutectic point, both curves a and b are extrapolated as dotted lines. The light line is the formation conditions of continental cirrus clouds from Heymsfield and Miloshevich [1995]. The dotted line and the dash line represent λ=1.0 and 1.7 in equation (1.1), respectively.

Chapter 2

INSTRUMENTATION AND TECHNIQUES APPLIED IN THESE STUDIES

2.1 Introduction to the CFD

We will briefly discuss the operating principles of the continuous flow thermal gradient diffusion chamber for ice nucleation measurements in this section. Dr. Rogers developed all of the three different versions of the CFD used in this dissertation. The detailed description of the chamber can be found in Rogers [1988]. The principle used in the CFD to create supersaturation relative to water is somewhat similar to that used in the thermal gradient diffusion chamber for detection of cloud condensation nuclei. The major advantage over earlier IN detectors is that it samples continuously. It consists of two concentric copper cylinders with their axis aligned and airflow vertically downward in the annulus between them. Sample flow is kept within 10% of the total volumetric flow, and is sandwiched by two equal, particle-free sheath flows. The two cylinders are coated by ice frozen from de-ionized water. Depending on the capacity of the cooling system the chamber works with, the wall temperatures can be cooled down to -60°C. The humidity generated inside the sample lamina ranges from ice saturation to 10 to 20% SSw, as long as the chamber is provided with enough flow to keep the sample lamina stable. Typically near -60°C, the relative humidity with respect to water is between 58% to 110% RH_w. Sample residence time depends on the length of the chamber, as well as on the total flow rate. In the experiments using the laboratory version of the CFD (CFD III), it is above 10 s.

The schematic of the CFD is shown in Figure 2.1, and sample profiles of airflow velocity, temperature, water vapor pressure, relative humidity, and ice saturation are shown in Figure 2.2.

In the original version of the CFD (CFD I), there is a window in the middle of the outside wall. Using a laser beam to illuminate the flow, we can locate the position of the sample lamina. The chamber is short, only 60 cm. The last 1/3 of the warm wall is insulated and dry, with no ice coating. The purpose of this section is to expose the aerosol sample to ice saturation and water subsaturation at the cold wall temperature, which evaporates the haze droplets, whereas ice crystals merely cease further growth. The cooling systems to control the temperatures of the walls are a Forma (Forma Scientific Co.) bath circulator and a Neslab circulator. Coolants are pumped into copper coils wound around the two cylinders. The lowest sample temperature that can be achieved with this system is around -25°C. The data system consists of one PC to record the conditions in the system, and another computer to log the spectra of ice crystals detected at the outlet of the CFD. At the outlet of CFD I, a white-light optical particle counter(Climet A6064A) is used to size and count ice crystals.

The airborne version CFD (CFD II) is a second-generation instrument and is refined in many features. It is 90 cm long, providing a longer residence time for nucleation and growth. An insulation section of length 30 cm is on the warm wall, similar to CFD I. The cooling system uses the direct expansion of refrigerant from one compressor, and adjusts the flow rates of coolant through walls with digital valves to control temperatures. The particle size spectra are measured by a laser optical counter(Climet 7350A, $\lambda = 780$ nm) at the outlet of CFD II. All sampling conditions, such as the temperatures, supersaturation, residence time, IN concentration and IN collected number, are recorded and displayed in real time by one computer. The multi-window display interface provides the real-time conditions inside the chamber. The schematic diagram of the signal processing in the airborne CFD is shown in Figure 2.3. More details are given elsewhere [Rogers *et al.*, 1998].

The new CFD III varies from both earlier versions. In addition to all the features of CFD II, it is much longer, since the limitation of clearance inside the aircraft cabins is not present. The length of the chamber is 150 cm, giving the sample a residence time of $\sim$12 seconds at room pressure. Numerical calculations showed that it is sufficient to achieve

equilibrium between the particles and the ambient water vapor concentration and to freeze the nuclei and grow them as ice crystals. Furthermore, with sufficient time for ice crystal growth, calculations show that the size differences between haze particles and ice crystals are big enough to separate them optically. Therefore, the thermally insulating vapor barrier (known as the evaporation section) on the bottom of the warm wall is removed. In this CFD III, two Neslab circulators are used to cool the walls of the chamber. Instead of the alcohol used in CFD I, a more efficient heat conductive fluid, Syltherm XLT heat transfer fluid (The Dow Chem. Co., Midland, MI), is used to achieve temperatures as low as -65°C. Also, better insulation reduces the heat conductive loss, thereby helping to reach lower temperatures. The data system is similar to that in CFD II: it monitors and records pressures inside/outside the system, as well as the particle size spectra measured by the same optical counter(Climet 7350A) as the CFD II over preset time intervals.

The details of the principles of the CFD and a description of the new features of the CFDs can be found in Rogers [1988, 1994, 1998, 1999]. The precision of relative humidity and temperature measurements will be discussed in Chapter 7.

2.2 Aerosol particle generation system

Several types of aerosol particle generation systems were used in this work, including a commercially available atomizer, a sulfuric acid generation system, a system for dispersion of commercially available soot and a jet fuel burning system. The latter three were developed in the Cloud and Aerosol Simulation Laboratory, Department of Atmospheric Science, Colorado State University. The principles of these systems will be briefly discussed in the following subsections.

2.2.1 Constant output aerosol atomization system

A TSI Model 3760 Constant Output Atomizer (TSI Inc., Minneapolis, Minnesota) was used to generate ammoniated sulfate particles for the cirrus cloud study. The schematic is shown in Figure 2.4. To make specified concentrations of ammoniated solutions, a known volume of de-ionized water was added to the appropriate amount of salt. All salts were analytical grade chemicals. All containers and glassware were rinsed with de-ionized water

three times before and after use. Volumetric bottles were used to make the solutions. The mass of salt was weighted with a Mettler Analytical Balance (Model AG204) to within ± 1 mg. Solutions prepared in this way have concentrations within $\pm 0.1\%$ relative standard deviation (RSD). In our experimental procedure, the concentration of the solution was not important, because we used a differential mobility analyzer (DMA) to select the size of monodisperse output aerosols. However, the solution concentration changes the mode size of the poly-dispersed output of the atomizer and it is desirable if the mode size of the aerosol is close to the selected monodisperse size, since this maximizes the monodisperse number concentration. Based on the technical specifications, 40% (w/v, weight over volume) sulfate solution is needed to obtain 0.2 μm diameter dry sulfate particles. The atomizer was not designed for such a high solution concentration, from which it is easy to crystallize salts and block the flows. Therefore, we used a 1.0% w/v solution with a peak size at 0.06 μm in diameter, as shown in Figure 2.5. The number ratios of particles at 0.2, 0.32, and 0.43 μm in this distribution is 1:0.31:0.17.

The operating principle of the atomizer is to pull the solution through a small orifice, breaking the stream into small droplets. These small droplets are carried out by a particle-free airflow, which is perpendicular to a metal block, which serves as an impaction surface. Large droplets in the airflow have high inertial momentum, making it difficult for them to move with the airflow as it is forced around the impaction surface, thereby removing them from the air stream. Only those particles small enough will be left. These droplets partially evaporate when mixed with dry, particle-free air, leaving a crystalline particle behind. However, depending on the properties of the solute, it is not guaranteed that aerosol particles from the atomizer are dry and completely crystallized, even after mixing with dry air. Therefore further evaporation may be needed, as we will see in the ammoniated sulfate experiments. The pressure of the atomizer cannot exceed 35 psig. We used 30 psig for sulfate generation. The output of the atomizer is above 10^6 cm^{-3} at about 1 liter per minute (LPM), which is too high for most experiments. Different methods can be used to dilute the atomizer output. The one we used for the sulfate experiments was to add 30 LPM dry, particle-free laboratory compressed air into the sample aerosol. After heating

up to 60°C, the air stream was dried by passing through a diffusion dryer. The dew point of the output after this ranged from -20°C to -35°C, or 7% RH to below 2% RH (beyond the limit of the humidity sensor).

Only a small fraction of the particle-laden air stream was taken by the aerosol classification system, between 0.5 to 1 LPM, depending on the concentration required. The excess air was sent to exhaust. Because of the high dilution ratio, small pressure changes in the laboratory compressed air could vary the aerosol concentration significantly. Real time concentration was monitored by a condensation particle counter (CPC).

2.2.2 Sulfuric acid droplet generation system

The sulfuric acid generation system (shown in Figure 2.6) followed Middlebrook *et al.*[1997], and is similar to the one Hanson [1995] used. The sulfuric acid is supplied as a drop held in a heated block, which is used to raise the drop temperature to 75–110°C. Carrier gas (high purity nitrogen, General Air, Co., grade 4.8) flowing over the drop carries sulfuric acid vapor out of the heated region, where it experiences relatively lower ambient temperature. Under these supersaturation conditions, nucleation starts homogeneously (or heterogeneously when the system is used to coat soot) to form sulfuric acid droplets.

Sulfuric acid droplets generated in this way have a lognormal distribution. There are two factors that decide the distribution: the heating temperature and the quenching rate. The Clausius-Clapeyron equation [*e.g.*, Pruppacher and Klett, 1997] indicates that the equilibrium sulfuric acid vapor pressure increases nonlinearly with the temperature of sulfuric acid liquid. High vapor pressure creates higher supersaturation after quenching, enhancing the nucleation process, and producing larger, and more numerous particles. In our system at 2.5 LPM, the peak size of the sulfuric acid droplets relates to the heating temperature as

$$D_{sulfuricacid}(T) = 0.0131T^2 - 1.6526T + 61.936 \qquad (2.1)$$

In the above equation, the carrier flow is set at 0.5 LPM. T is in °C, $D_{sulfuricacid}(T)$ is diameter in nanometer (nm).

The other factor related to the distribution is the quenching time, which is a combination of the carrier gas flow rate and the temperature difference between the heated

and ambient sections. In this work we fixed the carrier gas flow rate at 0.5±0.005 LPM, therefore we can ignore the influence from changes in flow rate. The effects of the daily variation of the air temperature in the laboratory were eliminated by fine adjustment of heating temperature.

In our sulfuric acid experiments, we worked primarily with a monodisperse diameter of 0.05 μm, although other sizes (0.016 μm polydisperse) were also used occasionally. The monodisperse aerosol was created by passing the sample through a differential mobility analyzer, described below.

2.2.3 Commercial soot generation system

The commercially available soot particles we used are manufactured for pigments, copier machines and printing applications. Although there are several sizes of monomer available, from 23 nm to 95 nm, all of the samples arrive as large aggregations of individual soot monomers. They cannot be used in our study without having been broken up and suspended.

A simple generation system for this purpose was developed in our laboratory and is shown in Figure 2.7. The main component of the generator is an audio speaker, originally designed for a telephone. Commercial soot particles were put directly on the vibrating surface of the speaker. As the surface vibrated, the aggregated soot particles were broken apart. A small cylinder, 1 in. high, was put on the speaker to contain the particles. Suspended particles were carried out of the generator by nitrogen (industrial level, General Air Co.).

The speaker was driven by an amplified square wave signal from a function generator (HP Model 3300A, Palo Alto, CA). Tests showed that the optimized frequency is around 650 Hz. At that frequency, the sound wave is audible and a nuisance, so the generator was put into a box with insulated walls. The concentration of soot particles also varies with the amplitude of the speaker. We used 0.8 V amplitude in all our experiments. With the carrier flow at 2 LPM, the concentration of soot particles ranged from 700 to 2000 cm^{-3}, and varied with time. Real time concentration is needed for the CFD experiments, so the output concentration was monitored with a TSI Model 3010 (or 3020) condensation particle counter.

2.2.4 Jet fuel combustion system

The system consists of two parts, a camp stove and a grain bin. A camp stove (Model 311600, Mountain Safety Research, Seattle, WA) was used to burn jet fuel completely at high temperature ($> 1500°C$), and the grain bin provides a large space as a stable source for long time sampling. The diameter and height of the bin are 12 and 20 feet, respectively. The combustion air was cleaned by a filter from Clean Room Products Inc. (Model 203910L-11, CRP, Ronkonkoma, NY), with an efficiency of 99.9995%. After recirculating air through the filter for 30 minutes, the condensation nuclei (CN) concentration was as low as 40 cm^{-3}. Compared with the concentration of soot particles, which was always above 10^5 cm^{-3}, the ambient background can be neglected without dilution.

2.3 Aerosol size classification system (Differential Mobility Analyzer)

A TSI Differential Mobility Analyzer (DMA, Model 3071) was used to select monodisperse aerosol particles from a poly-disperse source, and to measure the size distribution of aerosol particles. Detailed information can be found in TSI manuals. Here we only discuss the principle of operation of this instrument briefly.

The design of the DMA is based on the fact that aerosol particles can be charged on the surface. When particles are exposed to a gaseous medium containing bipolar ions, the particles and ions will undergo frequent collisions due to the random thermal motion of the ions. The amount of charge at Boltzmann equilibrium is not a function of the aerosol chemical composition, but is only decided by the size. The core of the DMA consists of two concentric stainless steel cylinders that are electrically isolated from each other (Figure 2.8). An electric field with controlled voltage is maintained between the cylinders. The surfaces of the cylinders are polished precisely, to create a uniform electric field. To keep laminar flow between the cylinders, there are four controlled flows within the DMA: an aerosol sample inlet flow (poly-disperse), a sheath air inlet flow, a monodisperse aerosol outlet flow and an excess air outlet flow. As the sample flow enters the DMA, it passes through a beta radiation source, the Krypton-85 neutralizer, which provides ions to force a distribution of charge on the aerosol particles. When entering the annular space between

the center rod and the outer rod, the electric field established by the voltage difference forces the charged particles to move along individual trajectories. The trajectory of a particle is determined by its electrical mobility, which is a function of the particle diameter, the air viscosity, and the mean free path. The particle mobility is related to the particle diameter as follows:

$$Z_p = neC_c/3\chi\pi\nu_{air}D_p, \tag{2.2}$$

where Z_p (cm^2/volts/s) is the electrical mobility, n is the number of charges carried on the particle, e is the elementary electric charge (1.6×10^{-19} coulombs), C_c is the Cunningham slip correction, χ is a shape factor (= 1 for spherical particles), ν_{air} (poise) is the viscosity of air, and D_p (cm) is the particle diameter. In the above equation, we calculate C_c [TSI, 1994] as

$$C_c = 1 + 2.492\lambda/D_p + 0.84\lambda/D_p e^{-0.43D_p/\lambda} \tag{2.3}$$

where λ (cm) is the mean free path of gas molecules.

In equation 2.2, the smaller the size of a particle the greater its electrical mobility. When the charged aerosol sample enters the electric field, positively charged particles are deflected towards the inner cylinder, and only those paticles with a certain electrical mobility reach the monodisperse sampling slits and remain in the monodisperse outlet air stream. Those particles with different mobilities will either be collected on the inner rod or stay within the sheath flow, which becomes the excess flow at the bottom of the chamber. The relationship between the DMA voltage and the electrical mobility can be derived as [TSI, 1991]:

$$V = [q_{sh} + 0.5q_{sample}]\ln(r_0/r_i)/(2\pi LZ_p) \tag{2.4}$$

where q_{sh} and q_{sample} ($cm^3\ s^{-1}$) are the sheath air and sample flow rates, respectively, r_0 (1.958 cm) is the inner radius of the outside cylinder, r_i (0.937 cm) is the outer radius of the center rod, and L is the length of the DMA column (44.44 cm). Setting the voltage on the DMA column will select a certain mobility of particles. By scanning voltages, the mobility distribution can be measured.

Unfortunately, not all of the particles are charged when passed through the neutralizer; only a relatively small fraction of the particles are charged. The charging efficiency

is a function of size, and ranges between 5% and 40% for typical particle sizes. Furthermore, of those charged particles, only ~50% of them are positively charged. Therefore careful calculations are needed to compute the actual input size distribution of the polydisperse aerosol. We used a program called DMPS.BAS written by M. Wendisch and A. Wiedensohler in 1994.

In using the DMA to generate "monodisperse" aerosol particles, of course there is not only exactly one size of particles coming out of the outlet. There are several other factors that can broaden the width of the geometric standard deviation of the distribution of particles exiting the DMA. The first one is called the "multiple charging" problem. At Boltzmann equilibrium, some particles carry more than one charge, although the possibility is finite. In an equilibrium state, the ratio of particles carrying 1, 2, 3 ... n_p elementary charge units to uncharged particles is given in Figure 2.9. The study by Wiedensohler [1988] showed that for particle sizes below 0.07 μm, multiple charge correction is required only for up to two charges per particle; for particle sizes greater than 70 nm, the full multiple charge correction inversion (up to 6 charges per particle) should be applied. At a voltage set to obtain 0.2 μm singly charged particles in our laboratory, double and triple charged particles at 0.32 μm and 0.43 μm having the same electrical mobility will also be in the output stream. Considering the charging efficiency in Figure 2.9, we have 20%, 8.9%, and 4.0% of the input 0.2, 0.32, and 0.43 μm particles in the sample. Since the aerosol generation system produces aerosol particles in these sizes in the ratio of 1:0.37:0.17 (see §2.2.1), the monodisperse output of the DMA should contain $1 * 0.2 : 0.089 * 0.37 : 0.04 * 0.17 = 0.2 : 0.033 : 0.0068$, that is 83.4% 0.2 μm, 13.7% 0.32 μm, and 2.9% 0.43 μm particles.

For the homogeneous ice formation study, the droplets with larger volume have a higher probability of forming an ice germ than smaller ones, since the nucleation rates (number per cm^{-3} per second) are the same. At 90% RH, the volume ratio of solution drops can be calculated as $(0.2 \times 1.53)^3$:$(0.32 \times 1.59)^3$:$(0.43 \times 1.62)^3 = 1 : 4.6 : 11.8$. The numbers to multiply are the size growth factors of 0.2, 0.32, and 0.43 μm dry particles at 90% RH. When the "monodisperse" aerosols start to freeze, the number ratio of ice crystals formed

homogeneously in these three sizes is in $1 * 0.834 : 4.6 * 0.137 : 11.8 * 0.029 = 1 : 0.75 : 0.41$. In other words, when ice crystals are formed homogeneously, 46% of them are from 0.2 μm particles, 35% from 0.32 μm, and 19% from 0.43 μm. In the worst case, we assume that 100% of the ice crystals have their initial size as 0.43 μm. When we processed the spectra, the lowest threshold we chose to separate ice crystals from haze droplets was 1.6 μm, about 4 times larger than the 0.43 μm particles. Under the conditions (-60°C, <90% RH) of ice formation, the relative humidity inside the CFD can grow haze particles at most 2.5 times larger than their dry size (based on calculations with Köhler equation). Therefore we have confidence that it is impossible to miscount the haze droplets of the triply charged particles as ice crystals, and the size broadening does not change our interpretation of experiments. The growth of large particles into ice crystals consists of only 19it is possible that threshold ice formation, taken as 0.1 to 1% of the input particles, is due only to larger particles. In this case, the solution composition assumed for initiation of ice (*i.e.*, that for 0.2 μm solution drops) will be slightly different than the actual composition. We estimate this effect to be at most 54%. We neglect any further effects of multiple charge broadening in the following discussions.

The second factor that can lead to non-monodisperse output from a DMA is diffusion broadening. Diffusion is particularly strong for those particles smaller than 20 nm. Diffusion loss and broadening within the DMA need to be considered for particles below 0.02 μm. For 0.2 μm aerosol particles, diffusion processes are insignificant, and can be neglected [TSI, 1994]. Therefore we did not consider the diffusion broadening in the study.

Another error of size broadening comes from the finite geometry of the system. The size of aerosol inlet slots, although very small, varies the trajectories of aerosol particles. From the specification provided by the manufacturer [TSI, 1994] and the flow setup used in our system, the selected mobility is obtained within 10%. Referring to the electric mobility equation 2.2, the range of particle size will be $(1.01 \pm 0.1) D_{pg}$. Therefore the actual size ranges of the "monodisperse" 0.2 μm, 0.32 μm and 0.43 μm particles are 0.18 to 0.22 μm, 0.29 to 0.35 μm, and 0.39 to 0.47 μm, respectively.

To summarize the discussion above, even though the monodisperse output of the DMA is not strictly only one particle size, the multiple-size effects do not impact our experimental results significantly. The uncertainty introduced can be quantified.

2.4 Condensation particle counter

In this section, we will discuss the principle of operation of the condensation particle counter (CPC, TSI Model 3010). The lower size limit of this counter (50% counting efficiency) is around 12 nm diameter, and it has 100% counting efficiency for particles larger than 28 nm. There is also an earlier version of the CPC (TSI 3020) which is alternatively used. Their operating principles are similar. The main difference is that the TSI 3020 has an internal pump, while the TSI 3010 uses an external pump to pull the sample flow.

The schematic of the CPC is shown in Figure 2.10. A vacuum pump is put at the end of the flow stream. The sample flow is pulled through the inlet and enters a space saturated by butanol vapor. The vapor saturation is maintained by a butanol reservoir warmed to 35±0.3°C. After mixing with vapor, the sample passes through a condensor unit, which is kept at 10±0.3°C. Butanol vapor will rapidly condense onto aerosol particles in the flow stream, growing particles to several microns in diameter. They then pass through the optical detection unit and are counted. When a droplet enters the laser beam in the optical cavity, the scattering and absorption of light creates a signal pulse that is detected by a photodetector. The number of pulses is accumulated for a preset time, and is displayed as a number concentration.

In the CPC, aerosol particles are counted continuously; therefore the flow rate is critical for the concentration calculation. In the TSI 3010, a critical orifice is put before the external vacuum pump, to regulate the flow. In the TSI 3020, an internal vacuum pump regulates the flow rate. The accuracy of the TSI 3010 measurements is within ±10% up to 5×10^5 cm^{-3} [TSI, 1994].

2.5 Optical particle counter

The optical particle counter (OPC) is an instrument for counting particles. Some OPCs can also measure particle size. Several OPCs have been used in our experiments. The one used in most of the sulfate and sulfuric acid experiments is the optical sensor from Climet (Model 7350A, Redlands, California).

The Climet uses a laser diode as the source. When a particle passes through, a signal pulse will be detected by the photodector. At a certain velocity, the height of the pulse is proportional to the optical cross-section of the particle, which can be related to the physical size for a known composition. The pulse sizes are transferred to and processed by a circuit board. After being amplified at different gains, the sensor outputs the spectrum through three ports built on the board: high, low and digital. A multi-channel analyzer (Nucleus 1024D) reads these signals, sorts them into preset voltage bins, and accumulates the counts per channel. This distribution is then displayed on the CRT and transferred to the data-collecting computer.

In retrieving the size distribution, it is important to know the velocity of the aerosol particles, which can be calculated from the volumetric flow rate and the geometry of the optical cavity. The flow rate can be measured to within ± 0.05 LPM with the digital mass flow meter (Microbridge AWM 5140VN, see Appendix B.2).

2.6 Design of five-jet inertial impactor

To collect ice nuclei for later electron microscope (EM) analysis, we developed a new five-jet inertial impactor to collect ice crystals after the chamber. After ice crystals are intercepted by the impaction surface, they are melted and evaporated, leaving the residue as IN. Other large particles can also be scavenged. Therefore, a pre-impactor is needed in the sample inlet to remove large particles to collect IN. Haze particles and non-CCN aerosol particles are much smaller than the impactor cutoff size; thereby, they are not collected. The pre-impactor on the CFD II was used to remove particles with aerodynamic diameter larger than 2 μm. The five-jet impactor was designed to have a 50% cutoff diameter of 3 μm.

The design guidelines for an inertial impactor suggest keeping the Reynolds number (R_e) and Stokes number (Stk_{50}) within certain ranges. The Reynolds number is the ratio of the inertial forces of the gas to the friction forces of the gas moving over the surface [Willeke and Baron, 1993]. A R_e between 500 to 3,000 shows a smooth flow pattern. Poorer cutoff characteristics are observed at lower R_e. In pratical design, well-designed impactors can be assumed to be ideal and ideal collection efficiency curves can be applied. The impactor will collect all particles with Stk larger than Stk_{50}, which is equal to 0.24 for our round jet impactor. Depending on the ambient conditions, collection efficiency curve may vary.

The diameter of the jets in our design is 2.0 mm. Assuming the total flow rate through the CFD is 20 lpm, the volumetric flow through an individual jet is 4 lpm. The R_e number is calculated as

$$R_e = 4\rho_g \times W \times Q/\eta\pi W^2 = 4\rho_g Q/\eta\pi W \tag{2.5}$$

where W is the diameter of the nozzle (cm), ρ_g is the air density (g cm^{-3}), Q is the volumetric flow rate (cm^3 s^{-1}), η is the gas viscosity (1.81×10^{-4} poise).

Substituting the flow rate, the density of air (1.2×10^{-3} g cm^{-3}), and the 0.2 cm diameter of nozzle into the equation, the design R_e is found to be 2815.

Next we calculate the Stokes number for 50% collection efficiency:

$$Stk_{50} = 4\rho_p \times C_c \times d_p^2 \times Q/9\eta\pi W^3 \tag{2.6}$$

$$d_p = (Stk_{50} \times 9\eta\pi W^3/4\rho_p \times C_c \times Q)^{1/2} \tag{2.7}$$

where C_c is Cunningham slip correction, d_p is the cutpoint particle diameter in cm, and ρ_g is the particle density in g cm^{-3} (0.7 g cm^{-3} for ice crystals). Setting Stk_{50} equal to 0.24, we find the 50% cutoff diameter is 2.2×10^{-4} cm, or 2.2 μm. This is the cutoff size of this impactor under sea-level pressure. From the equation for Stokes number, both C_c and η are related to the pressure under which the impactor is operating. Calculation shows that the cutoff size changes to 1.9 μm at cold temperatures (up to -40°C) and low pressures (300 mb). This shift can be compensated for by slowing down the flow rate or by using more jets to decrease the individual flow. For example, for the measurements in the SUCCESS

mission, two jets were plugged under normal sampling conditions to increase the flow rate for interception of large particles. Using more jets under the same total flow rate will increase the cutoff size of impactor. A stub holding a TEM grid is placed underneath the central jet to collect aerosol particles for later analysis.

2.7 Electron microscope technique and individual particle analysis

The electron microscope (EM) uses an electron beam, instead of visible light as in an optical microscope, as the source to illuminate the microstructure of objects. Due to the short wavelength of the electron beam, the resolution of the EM is much higher than that of optical microscopes. Similar to an optical microscope, the EM consists of a radiation source (electron gun), projector lens, condenser lens, and objective lens.

When a well-focused electron beam bombards a specimen, it excites various signals, which can provide information about composition, structure, and topographical image in small areas of the specimen. The X-ray photons emitted by the specimen can be detected by wavelength- or energy-dispersive spectrometer (WDX or EDS, respectively). From the characteristic X-ray spectrum, the elemental composition of the specimen segment can be obtained. Due to X-ray absorption loss in air and the window crystals used to separate the microscope column and X-ray detector, unless an ultrathin window is used, the detector of the X-ray spectrometer is only sensitive to elements with atomic number above 11 (Na).

There are two electron microscopes available for research purposes at Colorado State University: a scanning electron microscope (SEM), and a transmission electron microscope (TEM). Both are equipped with an EDS system. Compared with the SEM, TEM has a better detection limit, which provides us the ability to analyze particles with EDS down to 0.1 μm in diameter.

Particles collected on the EM grids were examined using a Japan Electron Optics Laboratory, Model JEOL 2000 transmission electron microscope and energy dispersive X-ray spectrometer (EDS), sensitive to atomic number ≥ 11, at the CSU Electron Microscopy Center. Grids were first examined at low magnification (600 $\times$) to locate the approximate center of the particle deposit. Next, they were examined at medium magnification (10,000

×) to count the number of particles deposited in each square for several squares near the deposit center in a cross pattern. These counts were averaged and are reported here as the particle number per grid square. The sizes of particles were estimated as the average of the longest dimension and the orthogonal dimension. A lower limit of 0.1 μm particle size is estimated for X-ray analysis; for counting purposes, the lower limit size is 0.05 μm. In all the measurements, only elements with signal peaks three times higher than background level are counted. Small particles yield weak signal intensities. Therefore these EM results can only be treated as qualitative representations.

2.8 Pre-conditioner

Concerns about the consistency of the initial phase state of aerosol particles as generated, and changes in phase that might occur as the particles entered the CFD at warm temperatures, motivated the use of a special pre-conditioning apparatus. The pre-conditioner consists of two parts, a saturator and a pre-cooler. The purpose of the saturator is to elevate the moisture level inside the air stream, to deliquesce dry soluble particles, if these are present. To construct the saturator, de-ionized water was put into a Dewar bottle. A stainless steel tube introduces aerosol flow close to the water surface, and another stainless steel tube serves as an outlet. With this configuration, the humidity of the air stream can be increased to above 90% relative humidity with respect to water at room temperature.

The principle of the pre-cooler is fairly straightforward. A straight copper tube was soldered to a 1/4" stainless steel tube and they were insulated with a thick foam layer. A Formar bath circulator pumped cold ethanol through the copper tube, cooling the sample as it passed through the stainless steel tube. A thermocouple was put in the flow stream at the outlet of this pre-cooler, and showed the temperature of the air stream was as low as -30°C.

2.9 Procedure for ice formation studies

After the discussions of all of the commercial and laboratory instruments and devices, we now describe the overall experimental configuration (Figure 2.11).

In the sulfate experiments, we used 0.2 μm salt particles from the atomizer/DMA system. The pre-conditioner was used in some experiments to initialize the phase state prior to introduction to the CFD. As discussed before, the purpose of the pre-conditioner is to control the humidity of the sample stream, hence the phase state of aerosol particles as crystalline or solution.

The procedure used for experiments was as follows. The two bath circulators were turned on first, to cool down to -27°C without circulating the coolant to the chamber. In order to avoid frost formation inside the CFD chamber, we filled and over-pressurized the chamber with clean, dry air before sending coolant to cool down the chamber. When both walls were cooled to -25°C, de-ionized water was pumped into the chamber from the bottom outlet of chamber. As the chamber was filled, pumping was stopped and water was allowed to flow freely back to the water tank at the bottom. After the procedure, the walls of the chamber were coated with a thin layer of ice. Therefore this procedure is called "icing the chamber".

After the chamber was iced, the circulators were reset to the experimental temperature (*e.g.*, -50°C). With clean and dry air (or nitrogen) flowing through it, the chamber was further cooled down to experimental temperatures. The continuous airflow can prevent frost formation, especially in the inlet manifold. As the chamber reached the preset temperature, it was ready to go. At this point, both walls were equal in temperature. The whole chamber was isothermal, with humidity in the flow equal to ice saturation, because of the water vapor equilibrium between the ice layer and the gas phase. The sheath flows were recirculated for 20 to 30 minutes before introducing sample flow, in order to establish steady state between the two walls, and to remove background and possible memory effects (some frost particles precipitate into the optical cavity of the OPC) in the OPC. This is the initial point from which all experiments were started. The size distribution of particles at the outlet was recorded, both on the high gain and the low gain channels. Because ice saturation corresponds to relatively low water subsaturation (around 56.5% RH at -60°C), we treated these spectra as the input aerosol distribution spectra.

There are two types of binary data files generated in each experiment. The first six digits of these file names represent year, month, and day of the experiment. The

information about the CFD conditions, such as temperatures, flow rates, and relative humidities, are stored together with all digits as names. The spectra measured by the OPC are saved as files with their names ended as XXXXXXmc.XXX. These files cannot be read before being converted into ASCII format. In ASCII format, these spectra are recorded in 256 rows, corresponding to the 256 channels sorted by the multi-channel analyzer. Each column contains the number distribution integrated over 12 sec. Each spectra file can store at most 30 spectra. These spectra thereafter are plotted with Excel (on PC) or IDL (on UNIX).

Data recording began with a particle-free air sample. This sample was obtained by either using a high efficiency filter bypass or zeroing the DMA voltage when the preconditioner inline. After the counts on the low gain channel of the OPC were cleared out, and the counts on the high gain channel were stable, the sample aerosols were directed to the CFD chamber. The OPC measured the size distribution of particles at the bottom outlet of the CFD chamber. The size distribution spectra were later compared with each other and the input distribution spectra. The 200 nm ammoniated sulfate aerosols were barely seen as a shoulder at the small size channels on the OPC; 50 nm sulfuric acid droplets were hardly detected. If ice crystals were formed inside the chamber, calculations show that they will grow to several micrometers in size, while the droplets can increase their diameters by factors of 2–4 (depending on the initial size). Since the ice nucleation rate is a function of temperature (see Appendix), different size thresholds for the separation of ice from unactivated haze particles were selected. For example, we assumed 1.6 μm (1600 nm) as the threshold at -60°C. All particles above 1.6 μm were assumed to be ice crystals; smaller particles were not included as possible crystals. With this method, it is possible to underestimate the number of ice crystals, since some may have nucleated in the lower part of the chamber and not have time to grow past the threshold. Due to daily variations in aerosol concentration input to the CFD, we report the fraction of the number concentration that froze (the activated fraction), to make the measurements comparable. Results showed that when we lowered the threshold 0.4 μm to 1.2 μm, the activated point for ice formation would be deduced to be 2% RH lower. In that case, the background noise from

the optical counter was stronger, changing the detection limit of the OPC, and a higher activated fraction was needed to define ice crystal activation. This will push the meaningful ice crystal onset condition higher. In other words, the lowered threshold corresponds to a higher "activated fraction", so the observed onset condition would change less than 2% RH.

During the course of an experiment, by varying the temperatures of both walls, the relative humidity was raised in steps of 2% to 3% RH, up to conditions of supersaturation relative to water. As the humidity was changed, sample temperatures were kept constant within $\pm 0.3°C$. In this way, the dependence of ice formation on both relative humidity and temperature was measured. Three experimental series were performed, for particles composed of $(NH_4)_2SO_4$, NH_4HSO_4 , and H_2SO_4. A particle-free sample was measured between measurements to monitor potential leaking and background ice crystals that can occur if frost develops somewhere within the CFD.

In the first stage of experiments, aerosol samples were sent to the CFD directly, without any pre-conditioning. Inconsistent results were obtained for ammonium sulfate and ammonium bisulfate. The results can be grouped into two categories, related to the variations in the dew point of the sample flows. The pre-conditioning system was built to determine the impact of the phase state of particles on the freezing process. Experiments using that system constitute the second stage of tests. In the pre-conditioned tests, we compared the results under the same humidity and temperature with and without the pre-conditioner. The results will be discussed later. Uncertainty and error analysis will be discussed in Chapter 7.

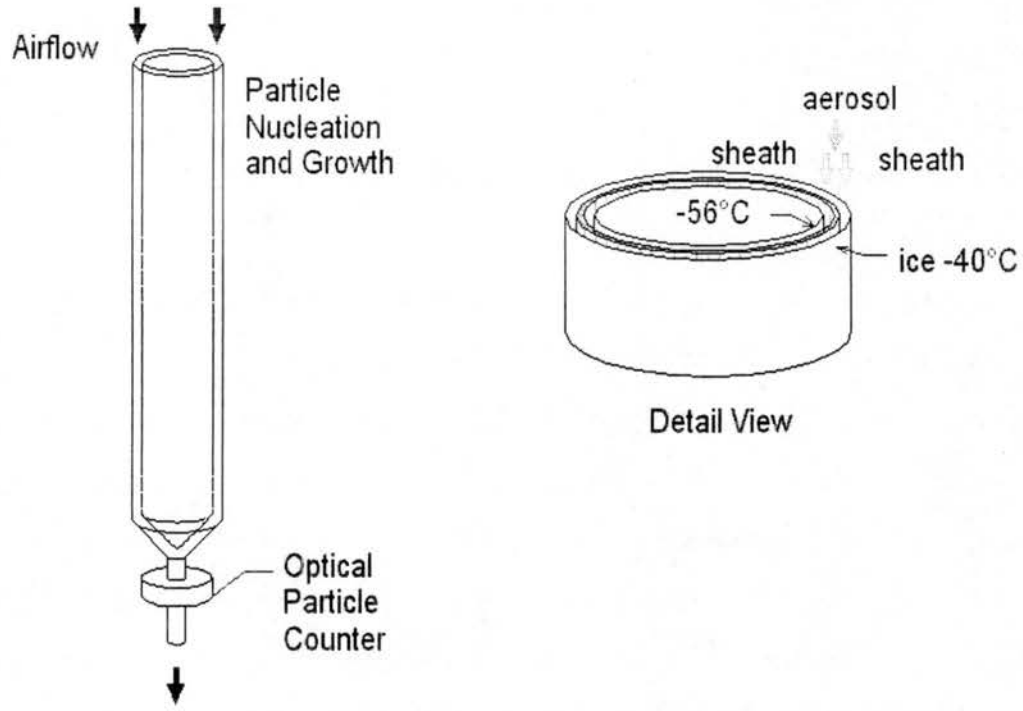

Figure 2.1: Simplified illustration of CFD operating principles. In this CFD, the evaporation section is not shown.

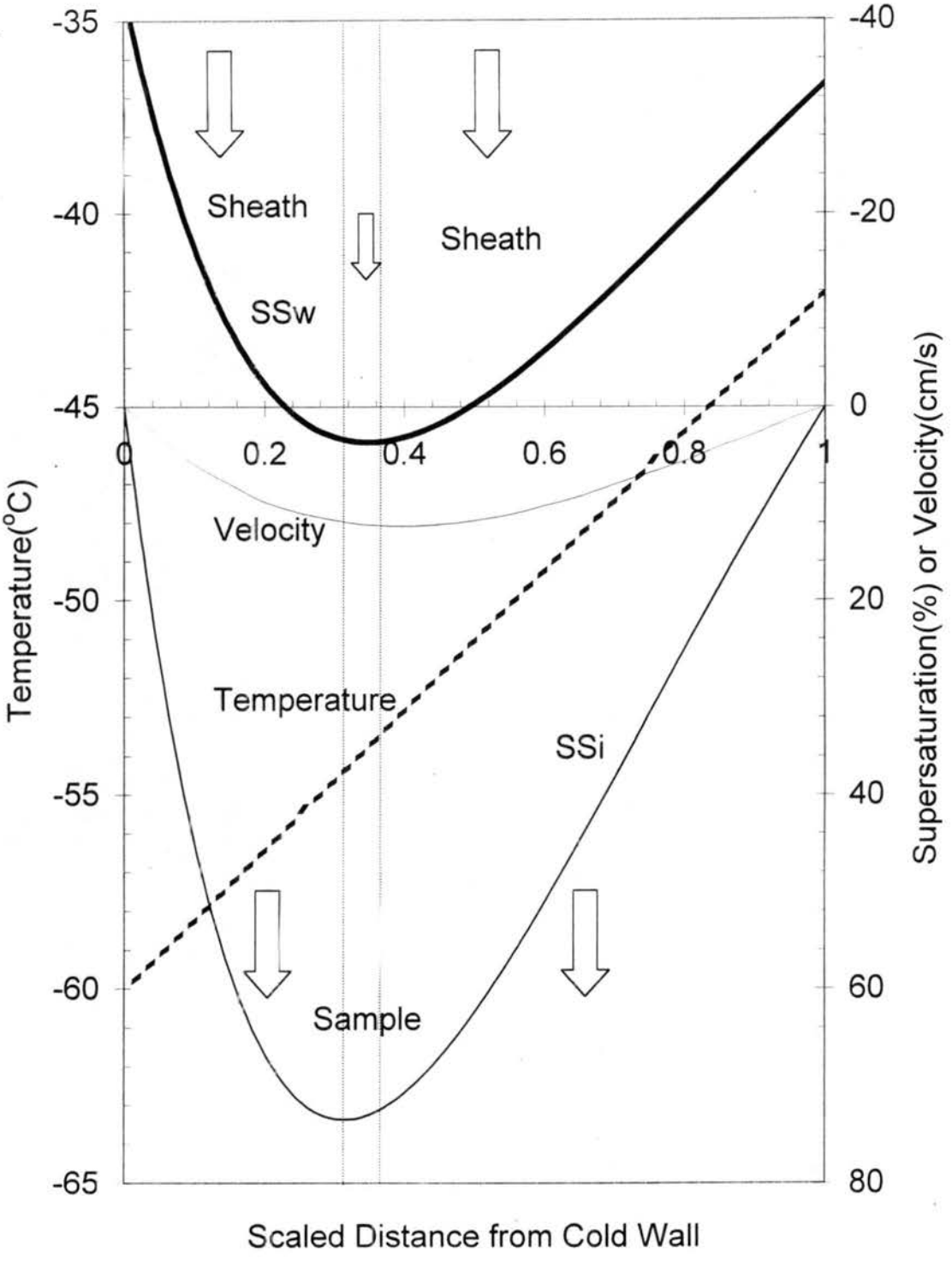

Figure 2.2: The schematic profiles of the temperature, supersaturation with respect to water, supersaturation with respect to ice, and velocity between the two walls of the CFD chamber. The flow direction is downward. The dash-dotted line is the central line between the two walls.

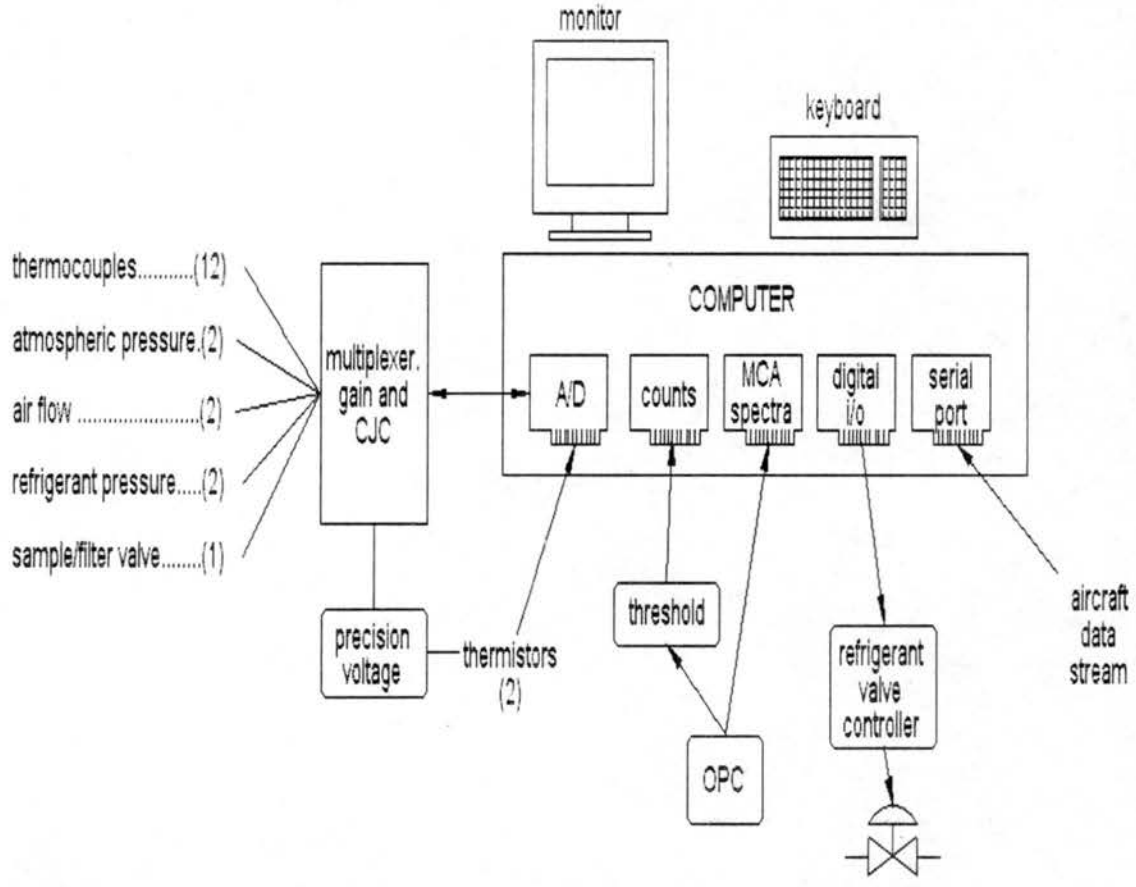

Figure 2.3: Block diagram of signal processing in CFD data system. A/D = analog to digital converter; CJC = cold junction compensation for thermocouples; MCA = multi-channel analyzer; OPC = optical particle counter.

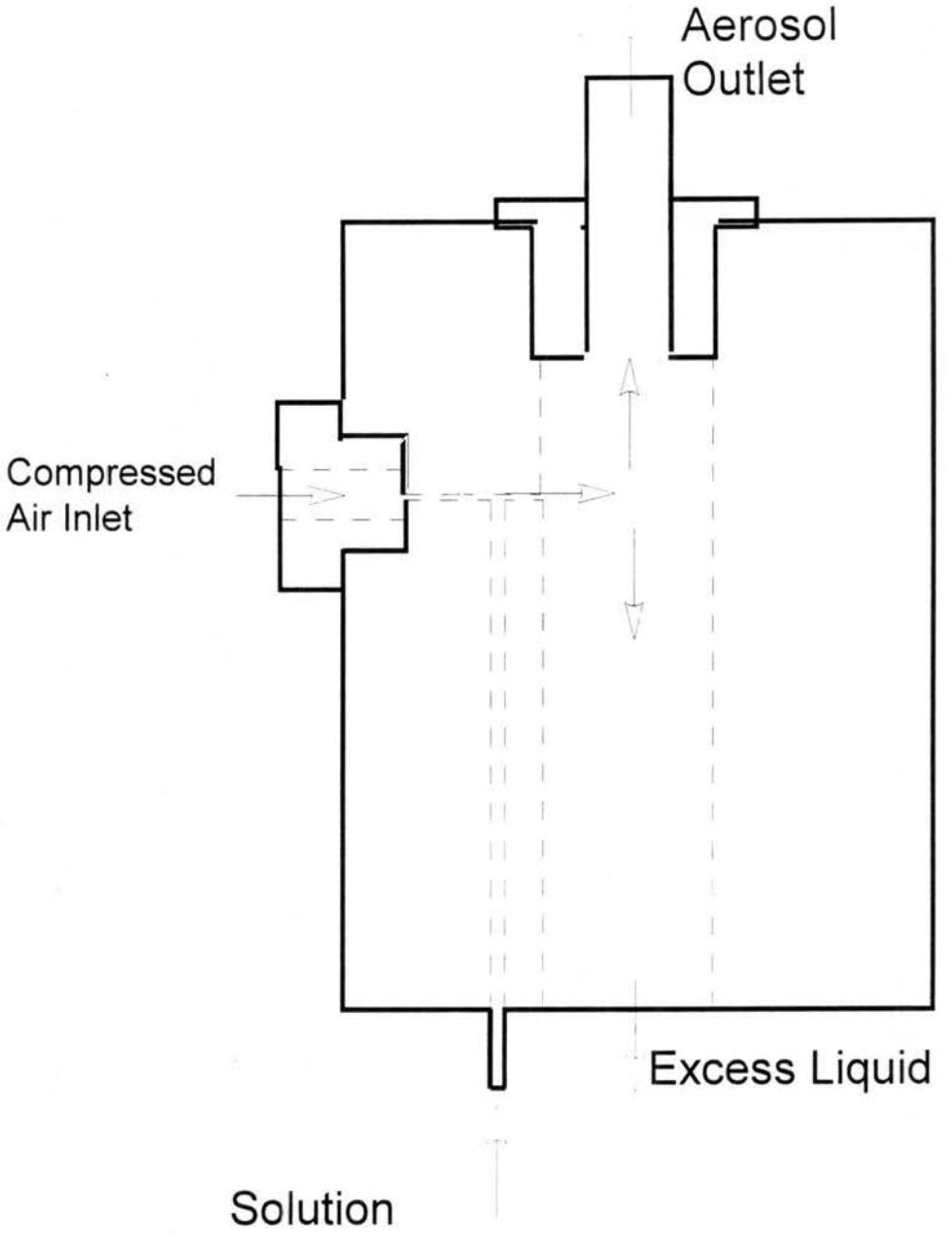

Figure 2.4: Schematic of the constant output atomizer. The solution is atomized into small droplets. Large droplets will be impacted and returned.

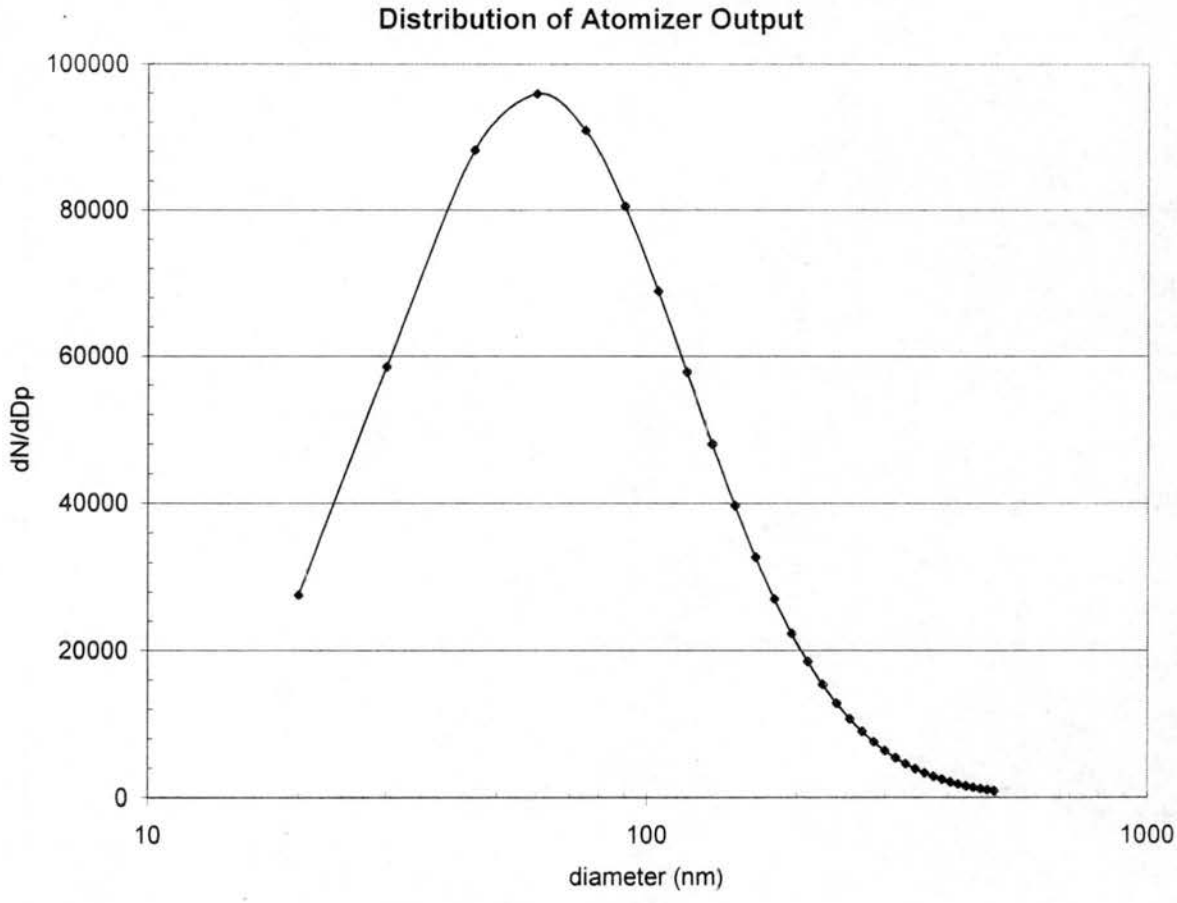

Figure 2.5: The size distribution of the atomizer output in this study.

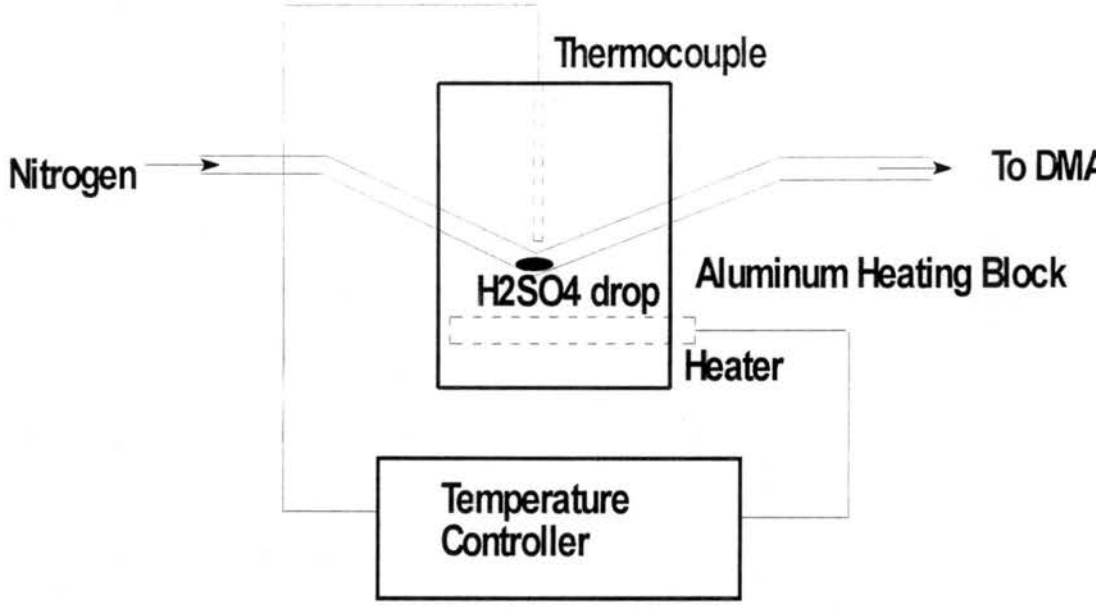

Figure 2.6: The sulfuric acid generation system. The temperature controller monitors the temperature inside the aluminum heating block.

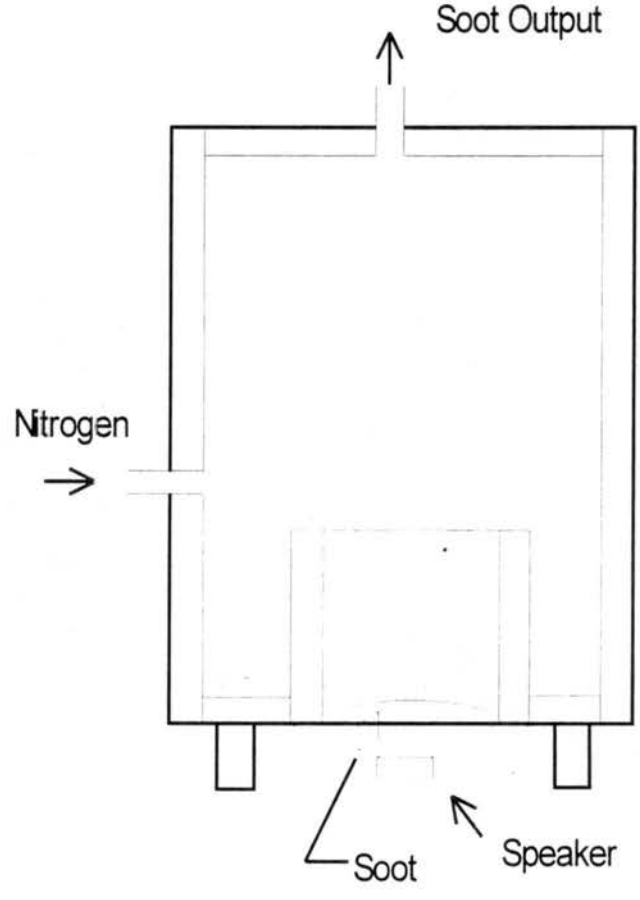

Figure 2.7: The commercial soot generation system. An audio speaker is used to break the aggregates of soot particles apart, and nitrogen brings these particles out of the generator. The speaker is driven by a square wave signal from a function generator.

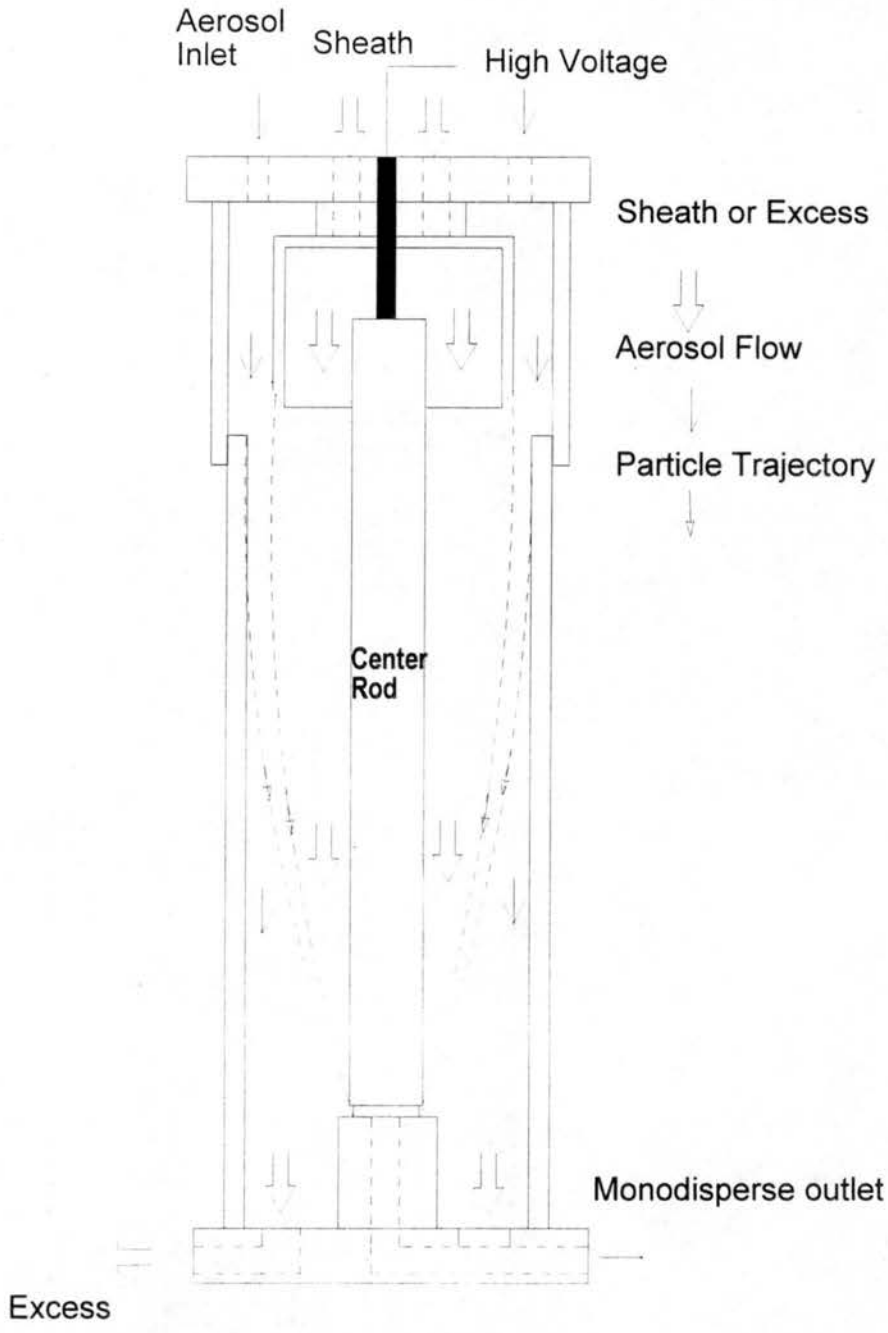

Figure 2.8: Schematic diagram of the Differential Mobility Analyzer (DMA). Arrows designate air sample flow pathways.

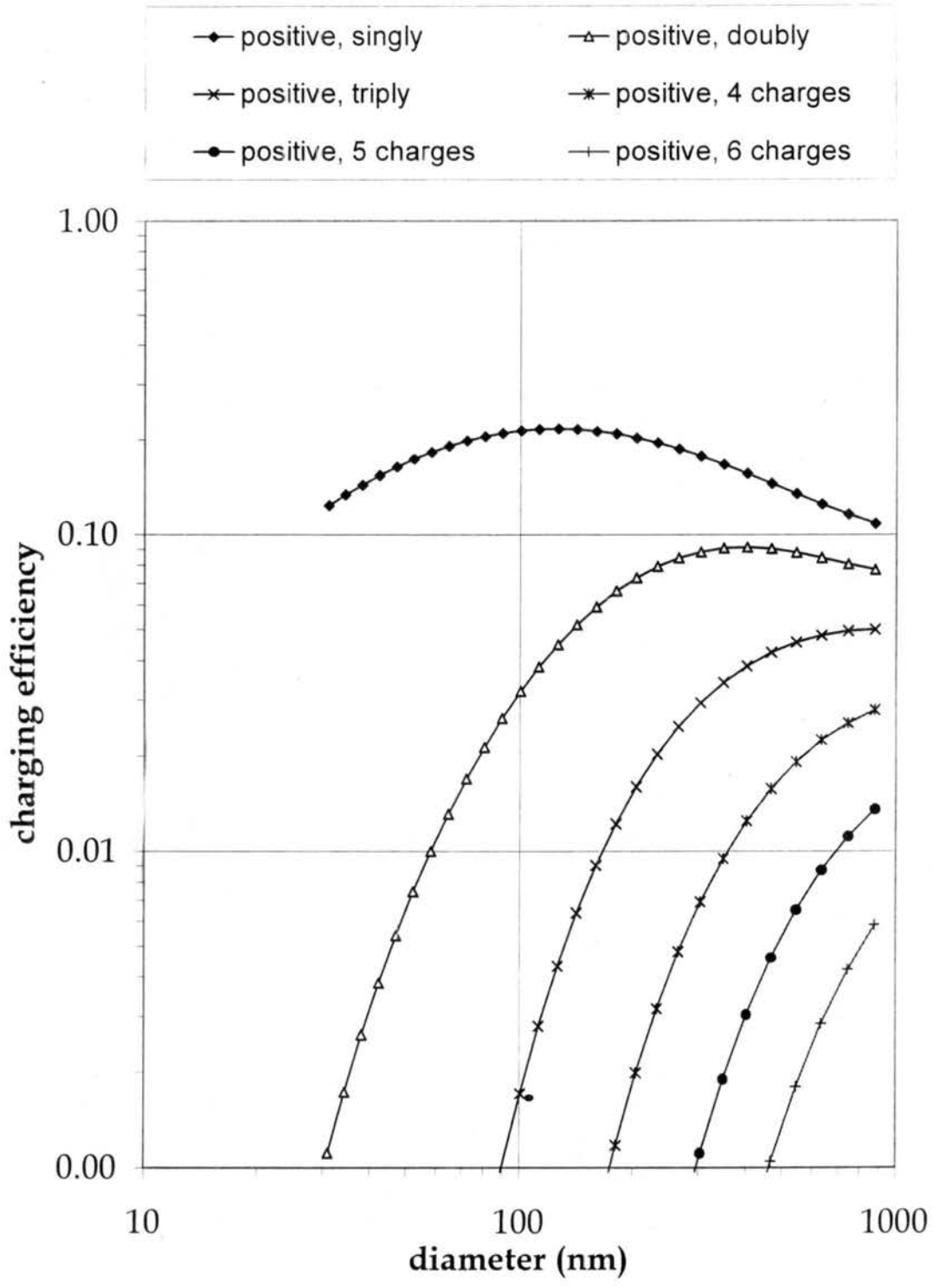

Figure 2.9: The charging efficiency for multiple charges on aerosol particles as a function of size. Here only positive charges are showed.

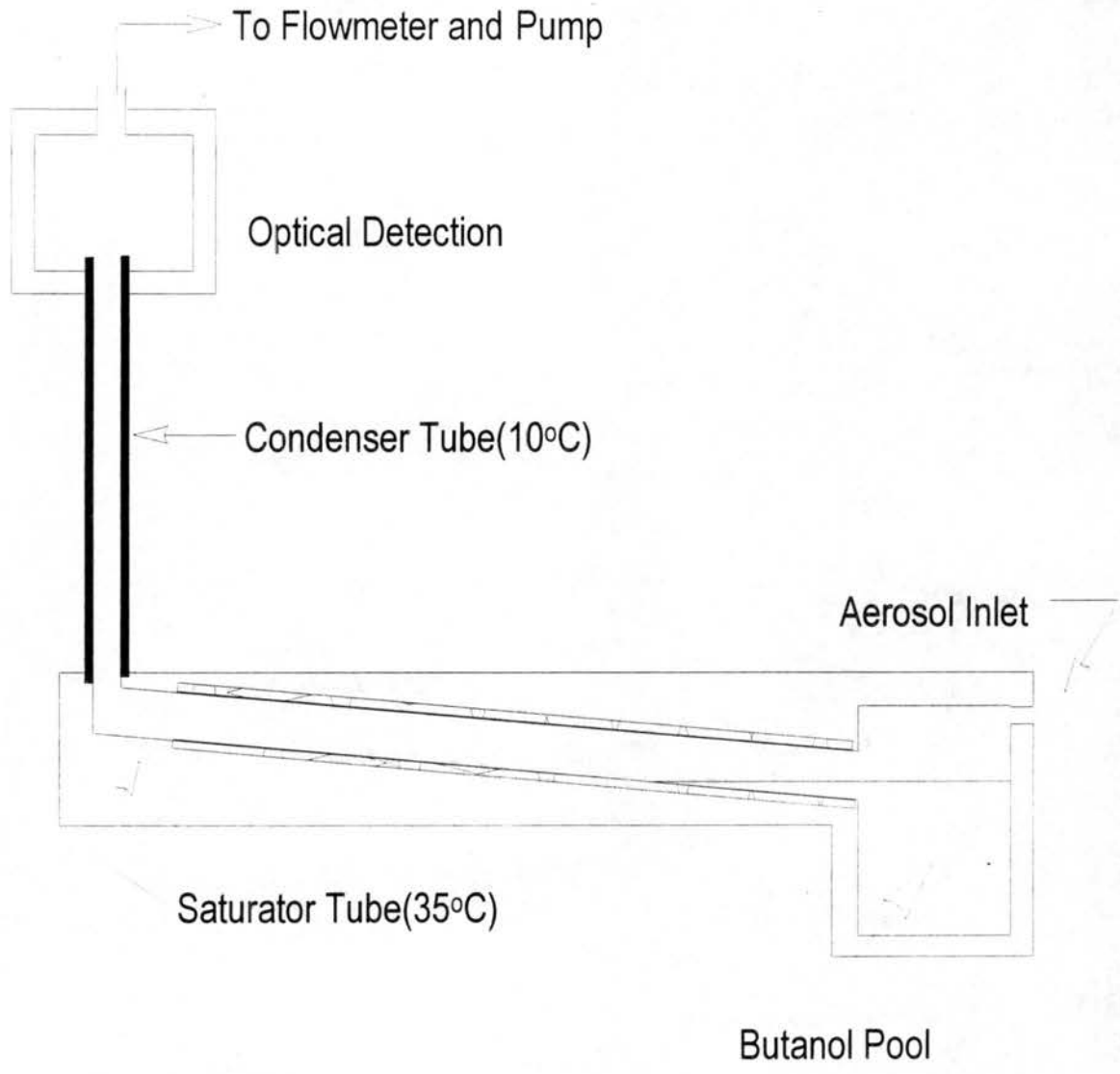

Figure 2.10: Schematic diagram of the condensation particle counter (CNC).

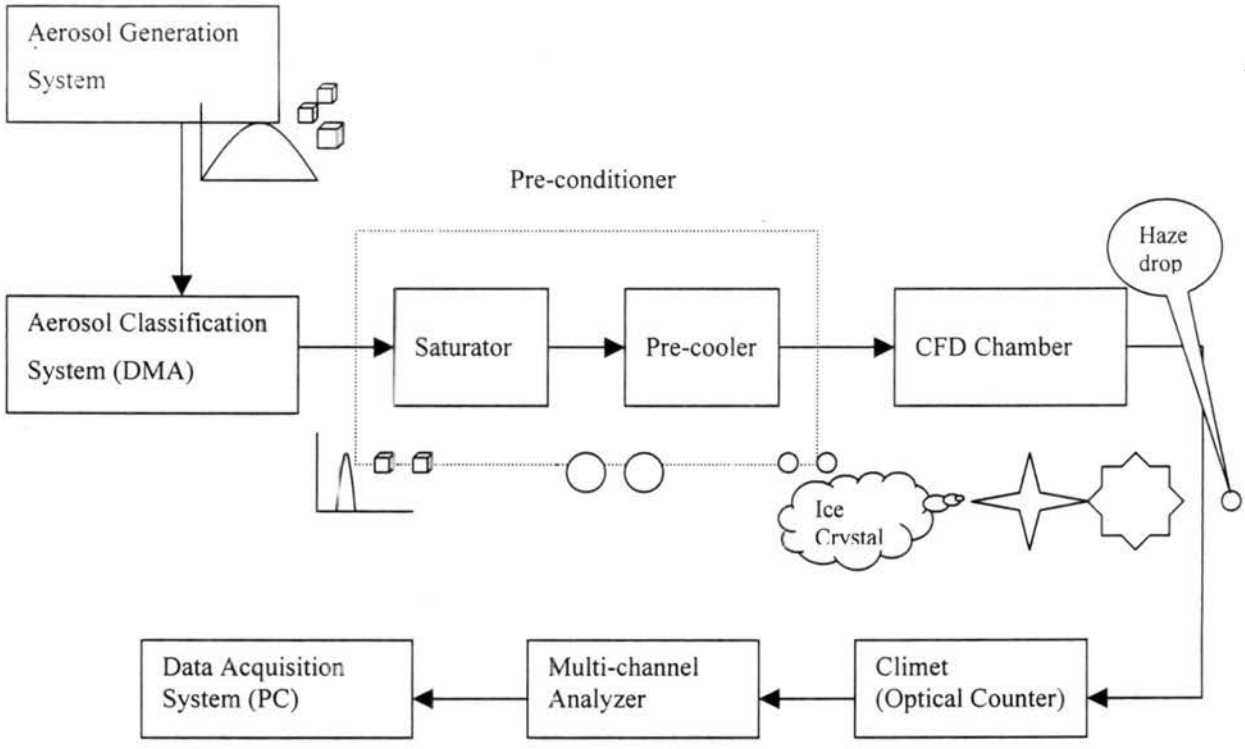

Figure 2.11: The experimental configuration used in this study. Between different stages, the size distribution and phase state of aerosol particles are indicated, as dry crystals, drops, or ice crystals.

Chapter 3

PROOF-OF-CONCEPT TEST – ISOLATING AND IDENTIFYING ATMOSPHERIC ICE-NUCLEATING AEROSOLS BY CFD

The objective of the first set of experiments reported here was to further test the ability of the CFD to discriminate IN from non-IN by showing that crystal residues contain only IN, and therefore, that crystal counts are not contaminated by the presence of non-activated particles. Laboratory-generated aerosols of known composition and concentration were used for these tests. In the second set of experiments, the same procedures were applied to collect and examine natural IN. Results of these experiments were reported in Kreidenweis *et al.*[1998].

3.1 Experiment description

3.1.1 Continuous flow diffusion chamber

The CFD I used in this study is described in Rogers [1988, 1994]. The instrument and principles of operation are reviewed only briefly in Chapter 2, with differences noted here. Ice crystals from the CFD are detected by an optical particle counter (OPC, Climet 6064A) at the CFD outlet, and the electrical signals are sized and counted with a multi-channel analyzer (Nucleus 1024D). When the aerosols are exposed to water supersaturation in the chamber, a subset of particles activate as cloud condensation nuclei (CCN), and nucleate and grow as solution droplets to their stable sizes. These sizes are defined by the Köhler equation (see Appendix), and are usually several times larger than dry CCN. The sizes of ice crystals are much larger than the drops, because the water supersaturations (2%) are typically much smaller than the ice supersaturations (~23%). Furthermore, the evaporation section at the last 1/3 of the chamber's warm wall exaggerates the size difference. In the evaporation section, a thin layer of dry foam insulation covers the warm

wall. After reaching a steady state, the temperature profile across the space between the two walls is unchanged, but the humidity becomes constant because there is no vapor source at the warm wall. The consequence is that the relative humidity in the sample flow decreases to a low level (ice saturation), and the drops shrink by evaporation; the saturation with respect to ice is still at 100%, keeping the ice crystals unchanged. In this way, the ice crystals can be distinguished from the drops in the aerosol size spectra.

In a previous study, Rogers [1994] tested the response of the CFD by sampling IN and non-IN alternately. In that experiment, silver iodide was used as the IN agent, and ammonium sulfate as the non- IN. As a hygroscopic material, ammonium sulfate particles deliquesce into drops at relative humidity about 80%. When exposed to water supersaturation, they readily serve as CCN, but not as IN at temperatures above -30°C. At the outlet of the CFD I, high ice crystal number concentrations were counted for the AgI sample flow and no large ice crystals were found when sampling ammonium sulfate.

3.1.2 Aerosol generation

A Skyfire-type generator (Montana State University) was used to burn an acetone-water solution for the generation of AgI particles [DeMott *et al.*, 1995]. The solution consisted of 2% AgI by weight, and the molar ratio of ammonium iodide to AgI was 1:2. The presence of ammonium iodide helped to increase the solubility of AgI as $Ag(NH_3)_2I$ in water. The solution was atomized, mixed with propane, and then burned. All samples were taken in a vertical wind tunnel 8 m downstream of the generator with a 4.25-l syringe. To dilute the high concentration, 90% of the syringe sample air was expelled and replaced with particle-free, dry air. Further dilution was made to transfer the sample into a 10-l electrically conductive bag, and mixed with more particle-free air to fill the bag. After briefly aging, the total concentration in the bag was measured with a CN counter (TSI 3010). The concentration of AgI varied between 500 to 106 cm^{-3}. According to DeMott *et al.*[1995], the aerosol particles generated with this method are poly-dispersed with a median size 0.05 μm.

A Constant Output Atomizer (TSI Model 3076) was used to generate non-IN CCN particles. The principle of this generator can be found in Chapter 2. The solutions used

were 1.6% by weight for both sodium chloride and ammonium sulfate. The aerosol particles were mixed with particle-free, dry air and stored in a 60-l electrically conductive bag. The size distribution of these aerosol particles can be fitted by a lognormal distribution, with a median size of 0.06 μm, based on the measurements by a DMA (TSI 3071A).

3.1.3 Experiment procedures

Experiments were conducted with three kinds of aerosol samples: AgI and NaCl, AgI and $(NH_4)_2SO_4$, and natural ambient air. The experimental configuration for the two AgI experiments was as shown in Figure 3.1. The IN and non-IN were mixed before entering the CFD. The flow of AgI aerosol was measured and regulated by a flow meter, and the flow of non-IN was the difference between the CFD sample flow and the AgI flow. With these two flows and their concentrations, we calculated the mixing ratio of AgI to non-IN. Before entering the CFD, the mixed aerosol particles were dried in a diffusion dryer, and large particles were removed from the sample stream by two series connected impactors (2 μm cutpoint diameter). These two impactors improve the efficiency for removing large particles. The operating conditions of these experiments are as shown in Table 3.1.

Table 3.1: Operating conditions for the CFD.

Experiment	Sample Temp. (°C)	SSw (%)	SSi (%)	Total flowrate (l min^{-1})	AgI flowrate (l min^{-1})	CCN flowrate (l min^{-1})	Total particle concentration cm^{-3}
NaCl/AgI	-19.8	0.7	23.6	7.3	0.3	0.3	3600
$(NH_4)_2SO_4$/AgI	-19.3	2.3	23.7	12.0	0.3	1.6	24100
Ambient	-18.4	1.9	22.5	10.7	1.72	1.72	-

At the outlet of the CFD, either the Climet optical counter (OPC) or a cascade impactor (PIXE Corp.) was connected to measure the distributions or to collect the aerosol particles. The flow through the impactor was regulated at 1 liter per minute. The sampling times for AgI/salt and ambient aerosols are 1 min and 1.5 h, respectively. Different bypass flows were needed to keep the CFD flow conditions the same between the OPC and PIXE samplings. The principle of the cascade impactor is similar to the five-jet impactor described in Chapter 2, but it has only one jet and multiple stages are

connected together in series. A total of seven stages was used to collect aerosol samples in this experiment, with 50% aerodynamic cutpoint diameters of 4, 2, 1, 0.5, 0.25, 0.12, and 0.06 μm. On each stage of the impactor, a copper transmission electron microscope grid was placed to collect aerosol samples. Calculations showed that active IN were expected to grow to at least 2 μm inside the CFD as ice crystals. Those ice crystals larger than several microns in size should be collected on the top two stages of the impactor (> 2 μm). Those IN that were activated later inside the CFD grew to smaller sizes, and non-activated particles would be captured on the lower stages. In these experiments, sodium chloride and ammonium sulfate particles are non-IN, and a fraction of AgI are relatively active IN, therefore it is reasonable to expect that only AgI particles, but not the salt particles, would nucleate ice and be captured on the first two stages.

As dry particles, AgI and NaCl have different crystal habits: smaller and spherical for AgI, and cubic for NaCl. These were easily identified with TEM by morphology and confirmed by Energy Dispersе Spectrometer (EDS). The compositions of the ambient aerosol sample were more complex, and cannot be identified only by morphology. In this circumstance, EDS was the only approach to measure the elemental compositions of individual particles. Figure 3.2 shows some examples of EM images and X-ray spectra from the test aerosols. In these samples, we could not detect Cu in any particles because of the strong signal from the copper grids. The spectra of AgI, NaCl, and $(NH_4)_2SO_4$ particles are shown in Figure 3.2a, b, and c.

3.2 Results and discussion

3.2.1 Mixed AgI/salt aerosols

Figure 3.3 shows the results of the AgI/NaCl experiments, which are presented as the number of particles detected per grid square for the grid squares examined, as a function of particle type and of impactor stage. The size ranges of particles that were impacted on different stages of the PIXE are summarized in Table 3.2.

The most significant feature in Figure 3.3 is the singular presence of AgI particles as residues of ice crystals on the two top stages of the PIXE, 2 and 4 μm. These two

Table 3.2: The size ranges of particles collected on the stages of the PIXE impactor after processing in the CFD, as determined by electronic microscopy.

Stage cutpoint (μm)	0.06	0.12	0.25	0.5	1	2	4
AgI size (μm)	~0.05	~0.1	~0.1	0.05-0.5	0.05-0.6	0.05-0.2	0.05-1.0
NaCl size (μm)	~0.05	0.05-0.2	0.1-0.5	0.05-0.8	0.1-1.0		
$(NH_4)_2SO_4$ size (μm)	~0.05	0.05-0.3	0.1-0.6	0.1-1.0	0.4-1.2		

stages are also the ones for which ice crystal collection was expected. As shown in Table 3.2, the sizes of these AgI particles were between 0.05 to 0.1 μm (as aggregate particles), far smaller than the 50% cutpoint of these two stages. These AgI particles could not be captured except as an inclusion in a much larger particle, *i.e.*, as an ice crystal. The size distributions of aerosol particles at the outlet of the CFD showed that the optical cross section sizes of particles were above 2 μm, both before and after aerosol sampling by the PIXE. These results confirm the ability of the CFD to selectively activate IN, and to grow them to a size large enough for optical detection or collection with an impactor. The IN particles collected after the CFD are expected to have different compositions than those input to the instrument: some species favorable for ice nucleation are enriched, some are removed. This capability supports the use of the CFD to study the effects of particle chemical composition on ice-nucleating activity.

The experimental temperatures used in this study are too warm to initiate homogeneous ice formation within water or solution drops. As CCN particles, no NaCl was expected to be collected on the 2 and 4 μm stages, although some of them were found on the 1 μm stage with sizes from 0.1 to 1.0 μm. Some were collected as crystals with a cubic shape, while most of them were impacted as drops with round impaction patterns on the substrate. Both types of particles (patterns) were also found on the 1, 0.5 and 0.25 μm stages. When NaCl particles entered the CFD, they may have deliquesced to drops after adjusting to the much colder temperature and being exposed to water super-saturations. In the super-saturation region of the CFD, the drops kept growing before entering the insulated evaporation region. Humidity measurements were conducted at the outlet of the

CFD with a chilled mirror hygrometer (General Eastern 1211 optical dewpoint sensor), indicating 80% RH. This humidity ensured that all NaCl exited as drops instead of dry crystals since the deliquescence point is at 76% RH. The deliquescence, droplet growth, and subsequent evaporation of NaCl particles is the most likely explanation for the predominant number concentration of impacted NaCl on the 0.25 μm stage. To illustrate the small features on the other stages, the ordinate in Figure 3.3 was truncated at 30.

In contrast to the selective presence of NaCl particles, AgI particles were detected on all impactor stages. This is what was expected, since not all of the AgI particles nucleate and grow into ice crystals under these CFD operating conditions. Only a few percent at most act as IN, and the others may pass through the CFD unchanged or condense some water vapor at the supersaturation conditions. Using a similar generation system, DeMott *et al.*[1995] found only 0.3% of $AgI_{0.8}Cl_{0.2}$-0.125NaCl aerosols were active IN in the CFD at -15°C and 2% supersaturation. Therefore those AgI unactivated would be collected on stages corresponding to their initial dry or wet sizes. Further, there is a humidity profile across the sample flow, which means some aerosol particles might experience higher humidity than the others. AgI used in the tests can form ice by all of the known nucleation modes, and is known to be a particularly effective contact freezing nucleus. Those IN at lower humidity or in different nucleation modes will nucleate at later times, and don't have much growth time available. This was also confirmed by the broadened size distribution of ice crystals on the OPC. The presence of AgI on the 0.5 and 1 μm stages may be due to crystals that had shorter growth times in the CFD, or to crystals that partially evaporated during impaction. IN number may be underestimated by counting only stages with 2 and 4 μm collection cutoff diameters. The sizes to which crystals grow vary with their residence times inside the CFD, which can be changed by the total flow rate or the length of the chamber [Rogers, 1994].

Similar features were found from the results for the AgI/$(NH_4)_2SO_4$ experiment, as shown in Figure 3.4 and Table 3.2. The two notable aspects are: (1) only AgI, not $(NH_4)_2SO_4$, was found on 2 and 4 μm stages, and (2) a substantial number of the hygroscopic $(NH_4)_2SO_4$ particles were collected on stages larger than the aerosol dry size, suggesting that they were haze particles in the exit stream. The difference from the AgI/NaCl

results is the haze size distribution. $(NH_4)_2SO_4$ showed a secondary mode around 0.5 μm, and the main peak below 0.12 μm. From Table 3.1, the water supersaturation of this experiment was 2.3%, higher than the 0.7% of the NaCl experiment; the higher total particle concentration may involve more vapor competition between haze particles. These are likely reasons for the difference. Since the relative humidity of deliquescence of $(NH_4)_2SO_4$ is near 80%, haze drops were also expected.

3.2.2 Measurement of ice nuclei in ambient aerosols

The concentration of IN in the ambient environment is typically low; therefore only one stage (2 μm) was used to collect IN in this experiment. The other five stages with cutpoints from 0.06 to 1 μm were used to capture smaller particles. The number of particles per grid box on different stages is shown in Figure 3.5. The size distribution of 46 particles found in 21 grid boxes from the sample on the 2 μm stage (corresponding to IN) is shown in Figure 3.6.

The number concentration shows similar features to the results of the NaCl/AgI experiment: a large number of aerosol particles were found on the 0.25 μm stage, and the majority of particles collected on the 2 μm stage were much smaller than the impaction size. Even though we did not measure the size distribution of the dry ambient aerosol, it is unlikely that the number distribution in Figure 3.5 represents the natural dry aerosol sample. The likely origin of this number distribution is that most particles were activated as CCN in the CFD (1.9% SSw) and left the chamber as incompletely evaporated haze droplets above 0.25 μm. There were so many particles on the 0.25 μm stage that they piled up in the central deposit region, making it impossible to obtain an accurate count. Also, as described in Chapter 2, particles smaller than 0.1 μm are difficult to both compositionally identify and size with EM/EDS techniques, resulting in a bias toward larger sizes. The limitation is inherent to the individual particle analysis technique.

The loading on the 2 μm stage, identified as IN, was the smallest of all stages, as shown in Figure 3.5. The majority of the particles on this stage were discrete solids, and no droplet residue patterns were found, suggesting water insoluble properties. Figure 3.6 shows the normalized size distribution of the 46 particles on the 2 μm stage. The

distribution is monomodal in the range between 0.05 to 2.0 μm, with the peak at the 0.05 to 0.1 μm interval. A few large particles were in the 1.2-1.8 μm range. Pruppacher and Klett [1997] suggested that IN activity increases with size and decreases with its diameter below $\sim$ 0.2 μm.. Larger particles are more favored to initiate ice formation than smaller ones. At -20°C and water saturation (100% RH), the critical diameters are approximately 0.018 and 0.005 μm in vapor and inside a water drop, respectively. In our experiments, nearly all of the IN were larger than the critical sizes, expected at the experimental temperature and humidity. Smaller IN above the critical size, but below the detection limit of EM, may also have been activated and optically counted, but not counted on the impaction grid. The critical size is also dependent on composition and mode of ice formation, so that it is difficult to define the critical sizes with certainty.

The chemical compositions of IN particles on the 2 μm stage were represented by 17 arbitrarily selected particles. In this study, we categorized particles into four groups: silicate (crustal), metallic, sulfate, and mixture of silicate-sulfate. The distribution of composition for these 17 particles is shown in Figure 3.7. The dominant group is silicate, about 59% of the IN. Silicate particles often contain other elements (Ca, Fe, Al), associated with crustal material. Metallic particles comprise the second largest group, including metals or oxides. Titanium and iron were the two most frequently detected elements. All particles in the mixture subdivision are mixtures of silicate and sulfate, with silicate as the dominant component. There were no pure sulfate particles detected as IN. Both the non-drop residue pattern and the composition of the IN fraction suggest they contain insoluble components. These chemical composition results are consistent with previous reports from other investigations, as well as with theoretical predictions. For example, clay mineral particles were found to be predominant in the residue of ice crystals in Antarctic samples by Kumai [1976]. High proportions of Si rich in S were detected in ice crystal residues collected at a mountain site [Murakami and Kikuchi, 1982]. In the samples captured in Missouri [Rucklidge, 1965], the majority of the identifiable particles were silicates. Pruppacher and Klett [1997] suggested that many metal oxides, including iron oxides, are good ice nucleating agents.

Two sample spectra from particles collected on the 2 and 0.25 μm stages, representing IN and non-IN fractions, respectively, are shown in Figure 3.8. The large copper and small chromium peaks in both spectra are from the EM substrate, its holder and the objective aperture, not from the particles. The IN particle was about 0.3×0.2 μm, much smaller than the 2 μm cutpoint diameter, and thus, most likely is the leftover of an ice crystal. This particle contained primarily Si, Ca, and Al, was classified as silicate. These elements also appear in the non-IN particle from the 0.25 μm stage in similar ratio. However, small amounts of other elements, including S, Fe and K, were detected in that particle, which was approximately the same size as the IN particle. The presence of sulfur and potassium may suggest that this non-IN particle was partially soluble, grew and evaporated in the CFD, but did not nucleate ice. The absence of drop residues around the 2 μm stage IN particle is consistent with the concept that totally soluble particles cannot serve as IN at temperatures warmer than -20°C.

There are some experimental uncertainties in this study. The size of particle measured under the EM is the physical cross section of the particle, while the impactor collects particles according to their aerodynamic sizes. Irregular shape and density of particle are needed to determine the aerodynamic size of the natural aerosol particle, as [Hinds, 1999]

$$d_a = d_e\sqrt{\rho_p/\rho_0\chi} \tag{3.1}$$

where d_a and d_e are the aerodynamic and physical diameters of particles, ρ_p and ρ_0 are the densities of particle and water, and χ is the dynamic shape factor. For natural sands, χ is below 1.5, and the density of most silicates is around 2.1 g cm^{-3}. Therefore for the extreme case, the correction factor for size will be 1.2, that is, d_a is 1.2 times greater than de. In this study, the aerodynamic size is approximated by the physical size. With a mixed aerosol particle, such as silicates mixed with soluble sulfate, if the silicate components were large enough, the soluble sulfate should have deliquesced and continuously grown though the CFD. At the outlet of the CFD, the size of the particle could be large enough to be miscounted as IN by the OPC, or to be collected in the impactor. The mixed particles would have to have large dry sizes for this to occur. For a mixed particle with 1.5

μm diameter, assuming it consists of 90% insoluble carbon and 10% ammonium sulfate, the equilibrium size would be 1.6 μm after the evaporation section of the CFD at -20°C. Of the 46 natural IN collected, only 6 (13%) of the IN were larger than 1 μm, and none of them were found to have solution residue pattern, therefore possible misclassification of these particles is unlikely to have a large impact on the results. Another possible error is from contact freezing. The CFD does not distinguish contact freezing from the other mechanisms, which might cause misleading classifications of which particle types served as IN. At the low number concentration conditions characteristic of the ambient samples and the small residence time in the CFD in this study, collisions of particles and droplets are very unlikely. At most 1 to 2% of the ice crystals were formed by contact freezing, based on the studies of Song and Lamb [1994] and Young [1974]. Therefore we can say all these uncertainties will not change the general results for natural IN.

Based on the OPC measurements, the average natural IN concentration in the ambient experiment was 82 l^{-1} at 1.9% SSw, -18.4°C. Comparison can be made between this concentration and the particles collected by the impactor, given the flow rate, the collection efficiency of the impactor, the percentage of particles captured by the grid, the exposure time, and the count and distribution of particles on the TEM grid. From the 46 IN particles counted in 20 grid squares on the 2 μm stage, the upper limit of ambient IN concentration is approximately 140 l^{-1}. Although this estimate is subject to uncertainties in collection efficiencies, deposition distribution, and the exposure time, these two numbers are in the same ballpark, and imply the high efficiencies of collection with the cascade impactor.

3.3 Conclusions

The results of two laboratory aerosol samples indicate that the continuous flow diffusion chamber has the capability to distinguish IN from non-IN by their different nucleation and growth behaviors. Additionally, based on the size difference between nucleated crystals and unactivated particles, IN can be separated from non-IN. Impactors can be used to collect ice crystals after the CFD, and their residues can provide us with information about size and elemental composition of individual particles. Application of this approach

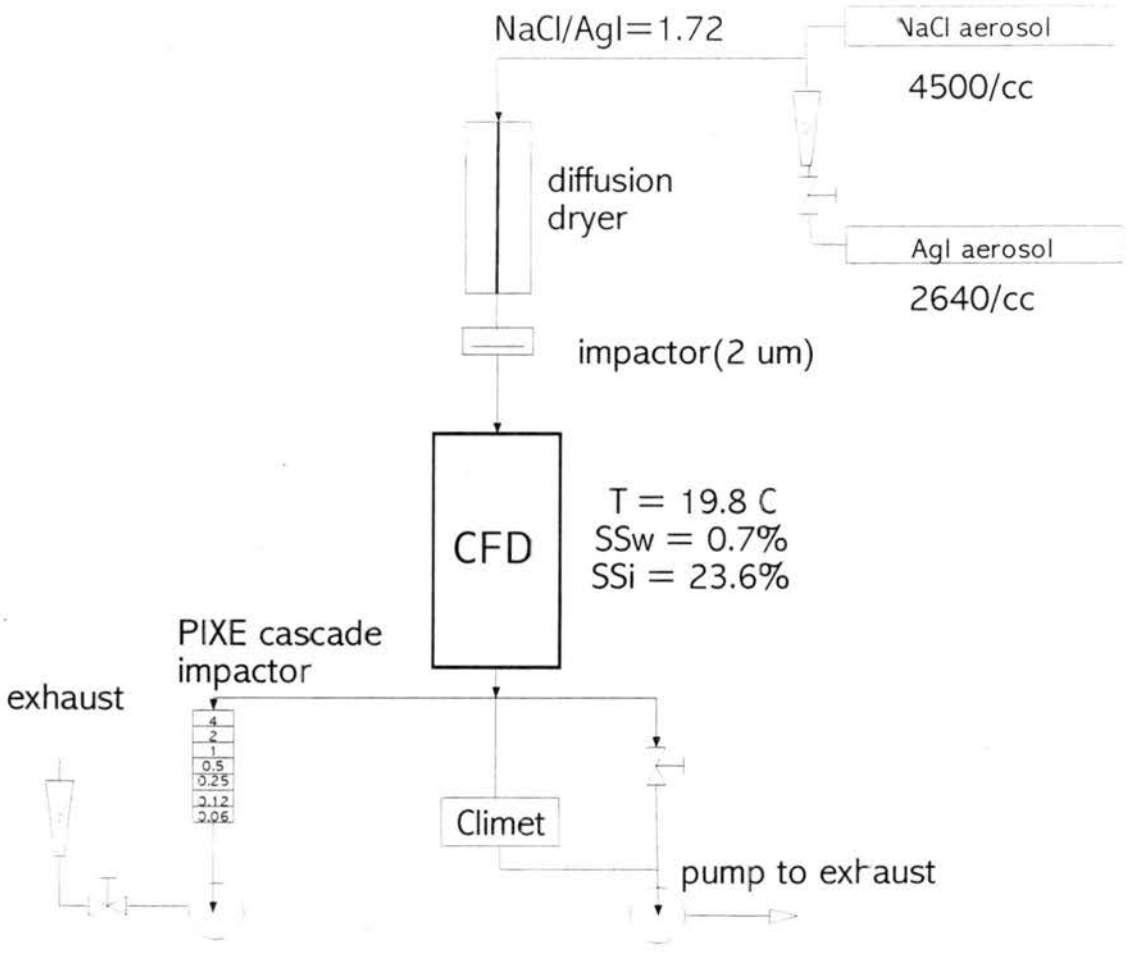

Figure 3.1: Schematic airflow in the proof-of-concept experiment. The Climet OPC and impactor were switched alternately.

a

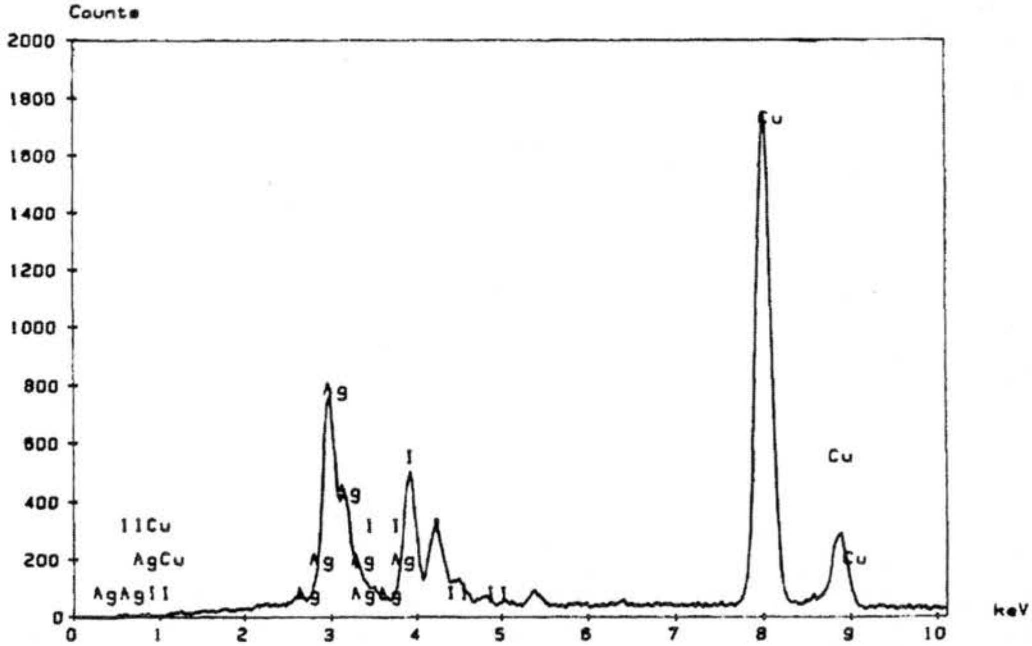
Counts
2000
1800
1600
1400
1200
1000
800
600
400
200
0
Ag
Ag
I
Cu
Cu
Cu
IICu
AgCu
AgAgII
Ag
Ag
Ag
Ag
Ag
I I
I I
I I
0 1 2 3 4 5 6 7 8 9 10
keV

b

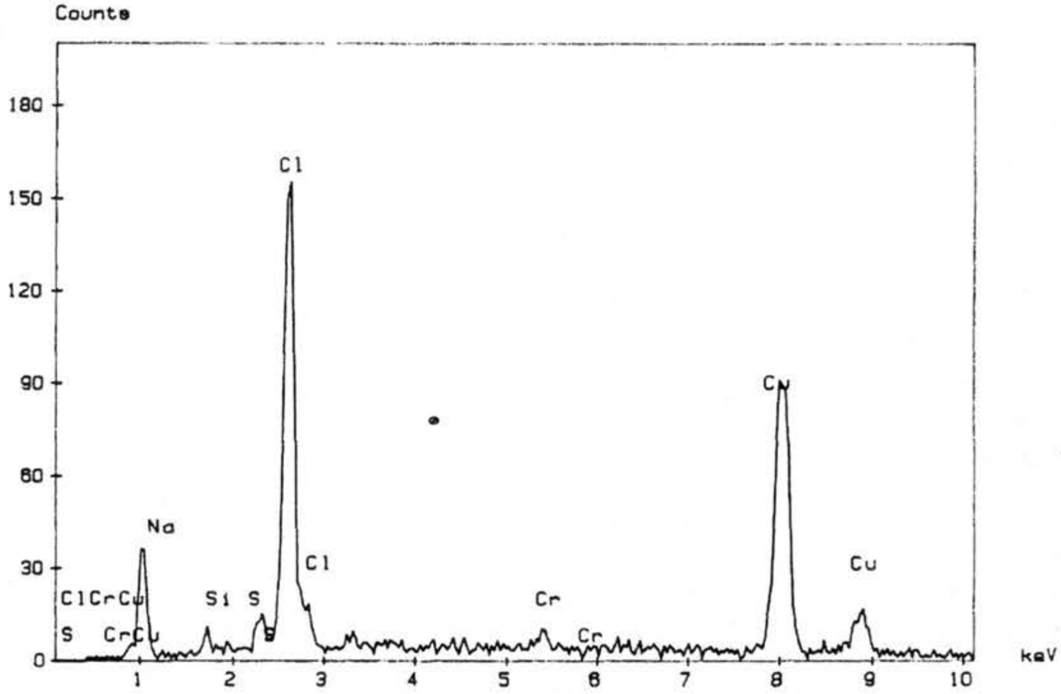
Counts
180
150
120
90
60
30
0
Cl
Na
Cl
Cu
Cu
Cr
Cr
ClCrCu
S CrCu
Si S
S
1 2 3 4 5 6 7 8 9 10
keV

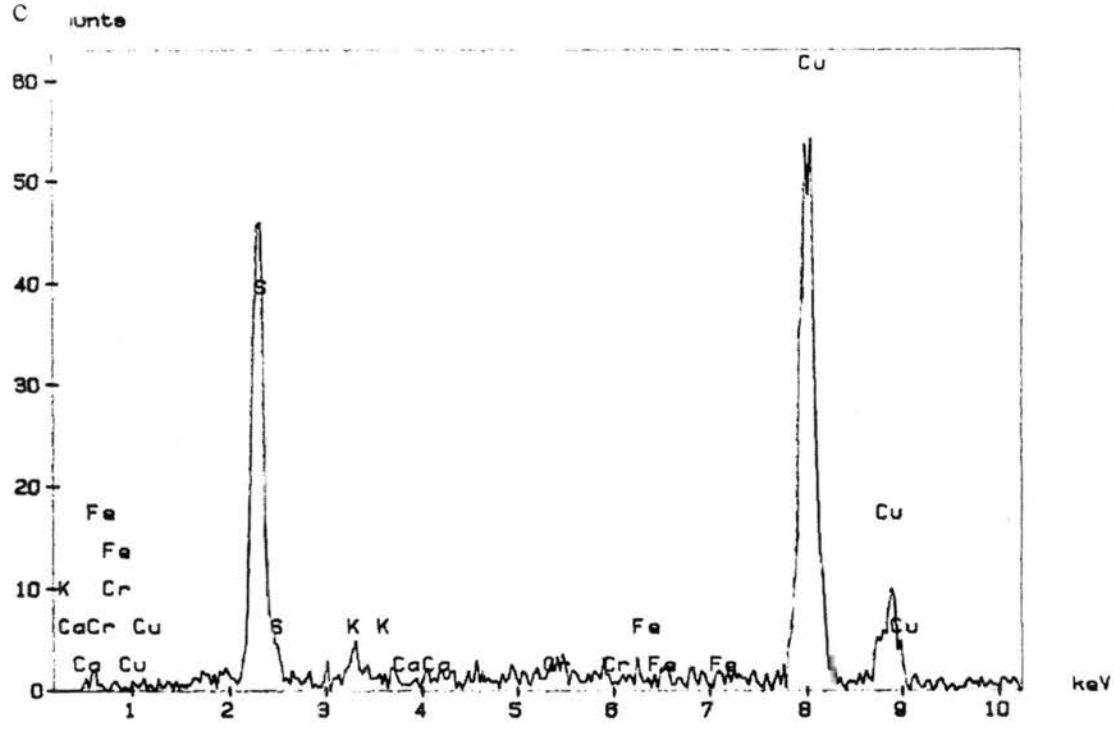

Figure 3.2: Silver iodide, sodium chloride and ammonium sulfate particles (or residue) and their energy dispersive X-ray spectra. (a) AgI; (b) NaCl; (c) $(NH_4)_2SO_4$

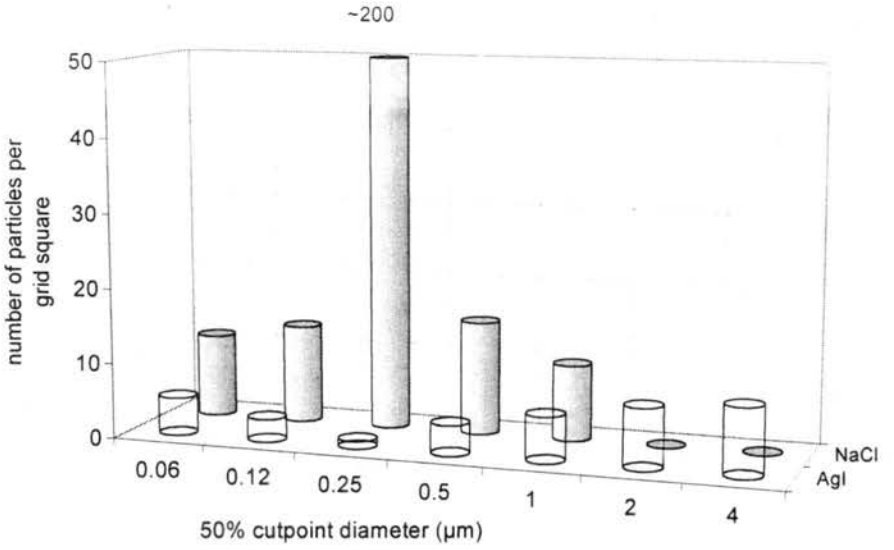

Figure 3.3: The number concentration of AgI and NaCl on different stages of the PIXE impactor as determined with transmission electron microscope. Vertical scale is truncated for clarity of other features.

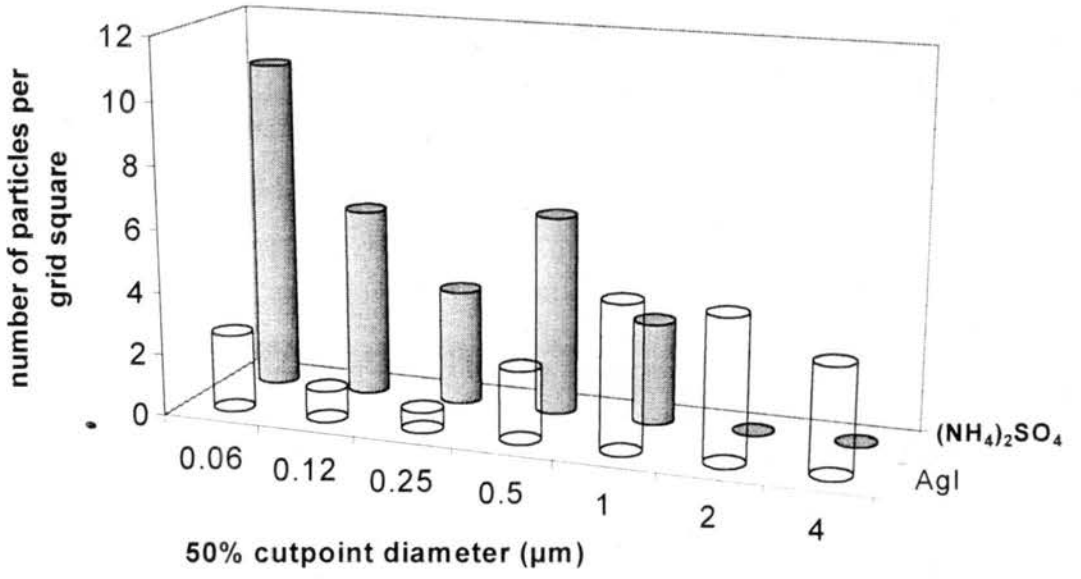

Figure 3.4: The number concentration of AgI and $(NH_4)_2SO_4$ on different stages of the PIXE as determined with transmission electron microscope.

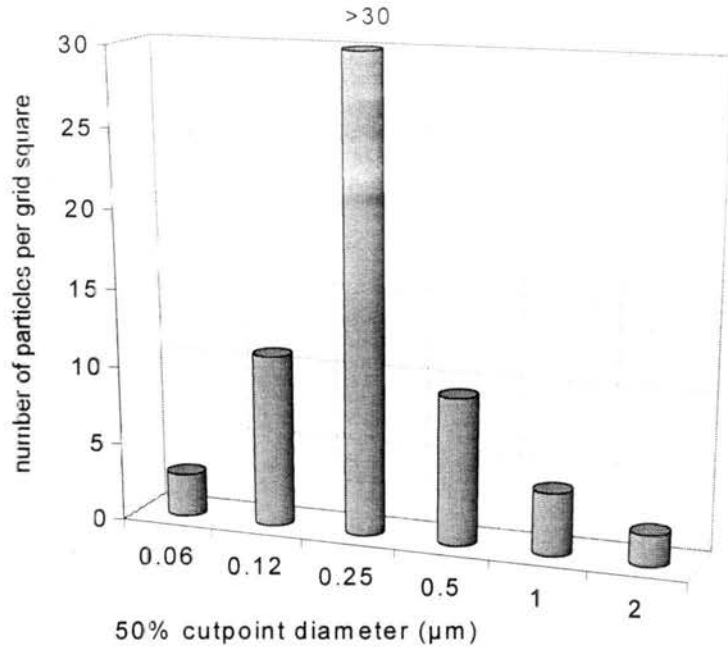

Figure 3.5: Number concentration of ambient aerosols on different stage of the PIXE after processing through the CFD. Vertical scale is truncated for clarity of smaller features.

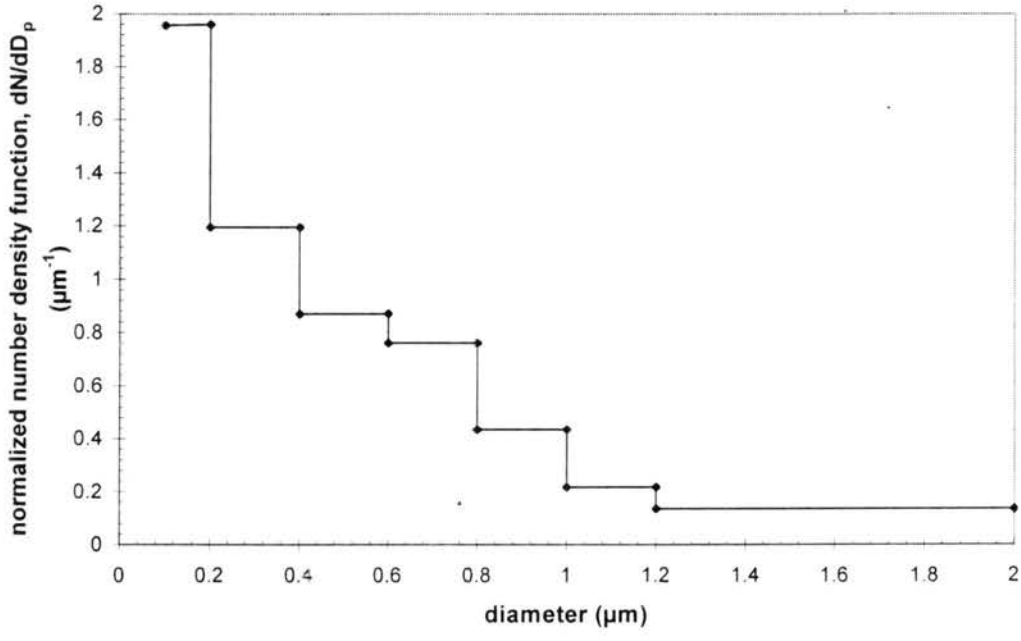

Figure 3.6: Size distribution of aerosol particles obtained from 46 particles on 2-µm cutpoint stage during the ambient aerosol experiment. The size is measured with the electron microscope.

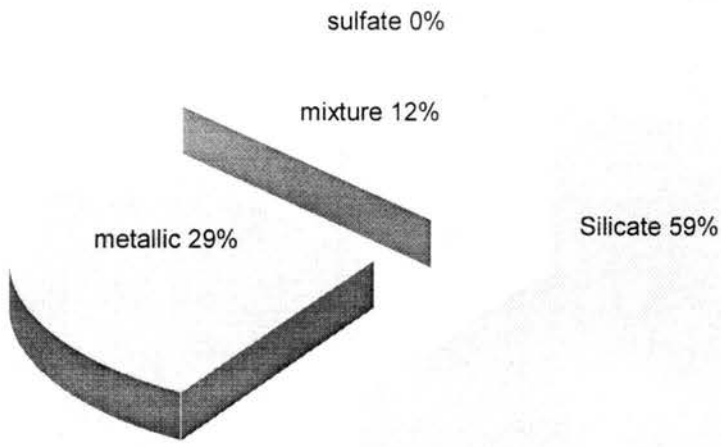

Figure 3.7: Chemical composition of IN in ambient aerosol collected on 2-μm stage by the CFD during the ambient experiment. The chemical information was based on 17 particles selected randomly from the 46 particles in Figure 3.6.

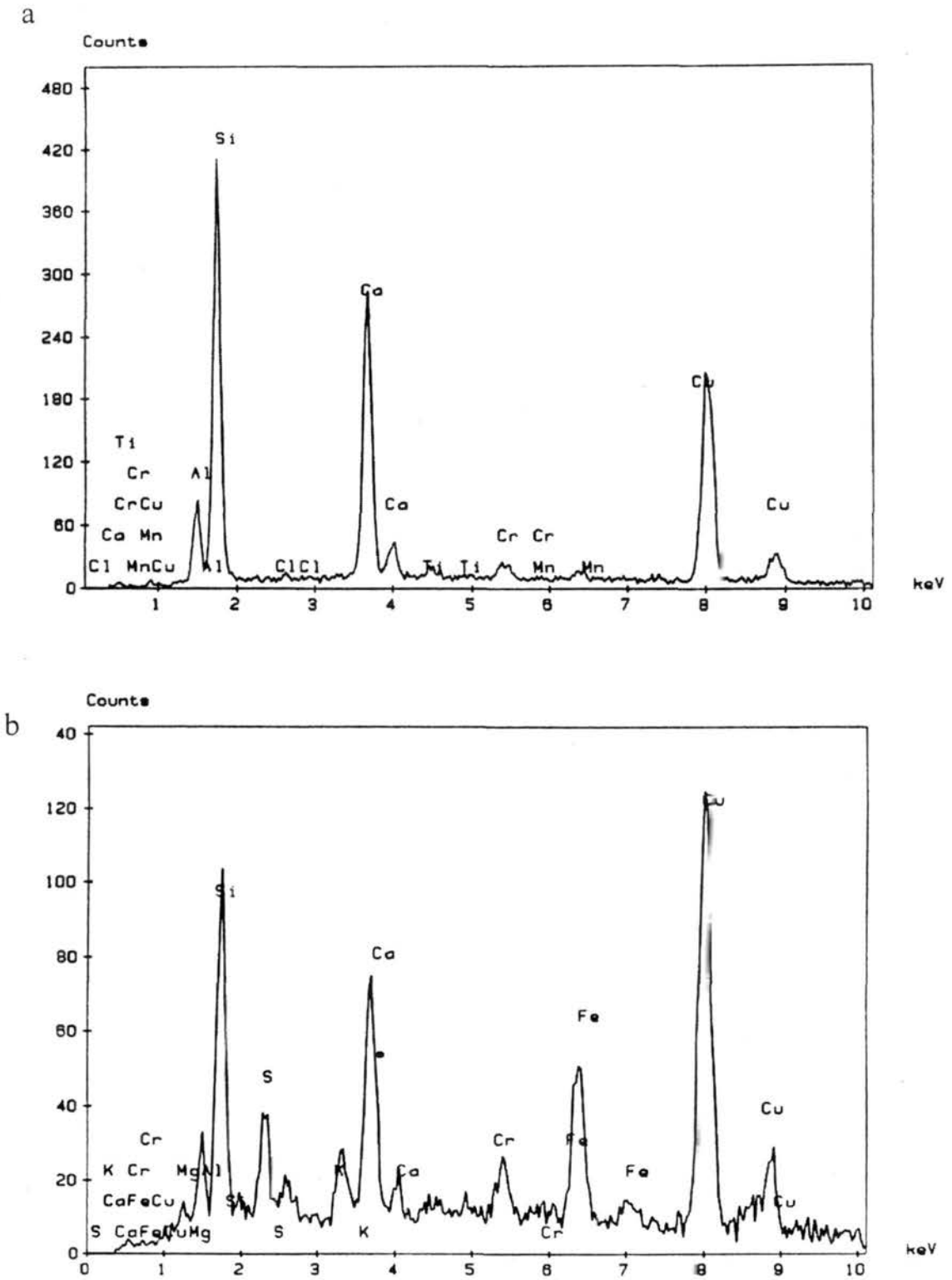

Figure 3.8: EDS spectra of an IN particle and non-IN particle in natural aerosol experiment. (a) silicate (from IN fraction); (b). mixture of silicate and sulfate (from non-IN).

Chapter 4

HETEROGENEOUS FREEZING STUDY – CHEMICAL COMPOSITIONS OF AEROSOL PARTICLES AND ICE NUCLEATING PARTICLES IN THE UPPER TROPOSPHERE AND LOWER STRATOSPHERE IN THE SUCCESS PROGRAM

In this chapter, we discuss observations of the chemical composition, size, and morphology of ambient particles and the IN subset in the upper troposphere and lower stratosphere. All of the aerosol samples were collected during the NASA Subsonic Aircraft: Contrail and Cloud Effects Special Study (SUCCESS, Spring 1996) project. One of the key objectives of SUCCESS was to investigate the impact of anthropogenic aerosol, particularly aircraft exhaust, on cold cloud and contrail formation. Some of the results summarized here were published by Chen *et al.* [1998].

The field campaign was conducted from April 10 to May 15, 1996. The first thirteen research flights were based out of Salina, Kansas, and the final three flights (including one ferry flight back to California) were based out of Ames Research Center, Moffett Field, California. For the first time ever, a CFD (the CFD II) was deployed on the NASA DC-8 airborne laboratory to detect and collect heterogeneous ice nucleating particles in the upper troposphere and lower stratosphere. A novel feature of this work was the use of this new instrument to detect and separate ice nucleating particles from an aerosol sample in real time [Rogers, 1993]. It is also the first time that both ambient aerosols and IN were collected and later analyzed by individual particle analysis techniques for the purpose of comparison of composition between these two particle types. Observations of ambient aerosol and IN number concentrations during SUCCESS and a description of the airborne ice nucleus detector are reported in DeMott *et al.* [1998] and Rogers *et al.* [1998].

4.1 Experimental approach

4.1.1 Sampling system

The CFD II was located at the rear left side of the cabin of the NASA DC-8. We shared an inlet probe with a research group from National Center for Atmospheric Research (NCAR). The probe faced forward, was located aft of the left wing of the aircraft, and was 38 cm from the skin which is long enough to sample above the air flow boundary layer created during the flight. The thickness of boundary layer is defined by the DC-8 flight manual. Air was sampled via the probe, drawn through a pre-impactor to remove particles larger than 2 μm in diameter, and then split into two flows. One stream was delivered to the CFD II to grow the IN rapidly by exposing the sample to ice supersaturations. With the configuration of the CFD II, we can nucleate IN and grow them to crystals ($D_p > 3$ μm) that were counted by an OPC (Climet 7350A) at the instrument outlet [Rogers *et al.*, 1998]. To eliminate detection of the homogeneous nucleation mechanism, we operated the CFD II above -40°C, mostly around -30°C. Supersaturations with respect to water were varied from positive (up to +10%) to negative (-20%). After the OPC, the IN fraction was collected with the five-jet inertial impactor with two jets blocked to have a 50% cut size of 2.2 μm at the high altitude pressure, such that only crystals were collected but not the non-IN [Kreidenweis *et al.*, 1998]. One CN counter (TSI 3010) measured the total ambient particle number concentration (in volume at the pressure outside the aircraft). With two PIXE cascade impactors (PIXE Corp.) available, we could at most collect two samples of the total aerosol in each flight. These samples are hereafter referred to as AP (ambient particles). With the flow rate at 1 l min^{-1} and 1 standard atmosphere, the 50% cut diameters of the six stages used are approximately 0.06, 0.12, 0.25, 0.5, 1.0, and 2.0 μm. On each stage of the PIXE impactor, as well as the collection stub of the five-jet impactor, a 200-mesh copper transmission electron microscopy grid, with a Formvar backing and evaporated carbon film for purpose of stabilization, was used as collection substrate. The sampling duration was about 15 to 30 minutes for AP, depending on the ambient concentration. For the IN samples, the duration was determined by accumulated optical counts, and was on the order of 1 hour due to the low number concentration of IN.

After landing of each flight, the samples were immediately transferred and stored in grid boxes. Right after the field campaign, selected samples were analyzed with individual particle analysis techniques at the Electron Microscopy Center, Colorado State University. The energy-disperse spectrometer (EDS) is sensitive to elements with their atomic weights above 11 (from Na) due to the absorption loss from the window between the EDS and the column of the EM for lighter elements. Replicate analyses of a subset of the samples were obtained by Dr. Lynn McInnes at the National Center for Electron Microscopy (NCEM, JEOL JEM 200CX) using an ultra-thin window energy dispersive X-ray detector (atomic number > 5) to detect lighter elements (*e.g.*, carbon and oxygen). The results of the replicates showed consistency between these two instruments. The procedure for the analyses is described in Chapter 2. Each particle was grouped into one of five categories based on its elemental spectrum, as defined in the following section. The lower size limit for sizing and counting was approximately 0.05 μm, and approximately 0.10 μm for the purposes of X-ray analysis.

4.1.2 Particle classifications

Based on the compositional categories used by Sheridan *et al.* [1994], we put all of the particles into five groups: crustal, sulfate, carbonaceous, metallic, and others. The crustal group includes silicate and silicon-dominated particles. Unusual smooth spheres were observed in some samples in this group, suggesting that some of them had experienced high temperature processes [Sheridan, 1989]. Both soot (black carbon) and non-soot carbon rich particles were grouped as carbonaceous particles. Under the bombardment of the electron beam within the electron microscope, these carbonaceous particles were distinguished by essentially no detectable elemental X-ray signals, or sometimes by trace amounts of Si, Fe, Cr or Ni overshadowed by a strong background; therefore the signals were weak in comparison to same sized mineral or metallic particles. The classification as carbonaceous was confirmed at NCEM using the more sensitive detector, for particles with an integrated carbon signal > 3 times the background signal of the substrate material in a particle free region. Some micron-sized carbonaceous particles contained $\sim$0.1 μm metallic particles, primarily Ti, as inclusions. These particles were classified as carbonaceous, instead of

metallic, due to the mass dominance of carbon over the metallic elements. Similar carbonaceous particles with inclusions were observed in the UT by Sheridan *et al.* [1994], and Hagen *et al.* [1994] show example spectra of UT coarse particles having fly ash (combustion) and carbonaceous compositions, similar to those we observed.

Particles classified as sulfates could be identified by their morphologies, depending on the extent of neutralization and the associated cations. The characteristic sulfuric acid drop deposition pattern is one or several big drops surrounded by much smaller satellites [Ferek *et al.*, 1983]. The fewer the number of satellites, the more the sulfuric acid is neutralized. There are no satellites present for totally neutralized sulfate drops. Droplet residue patterns without satellites, showing only a S signal in their X-ray spectra, were observed. These particles are most likely composed of totally or nearly totally neutralized ammonium sulfate, although the presence of nitrogen could not be confirmed with our detectors.

The composition and abundance of metallic particles varied dramatically from sample to sample. As will be discussed later, samples across exhausts of aircraft tend to contain more metallic particles than those outside exhaust-dominated regions. The metals most often observed included Al, Fe, Ti, Cr, Zn and Ca. They may be present as pure metals, oxides or carbonates; the window of our detector prevented us from distinguishing the X-ray signals of oxygen and carbon. Particles with predominantly a Cl signal, and those that were hard to group into previous categories (*e.g.*, P), were classified as "other". Most samples had no particles or only a small percentage of particles in this class.

4.2 Results and discussion

Here we discuss some samples collected during the research flights on May 4, 8, and 12, 1996. The measurements of bulk chemical compositions and NC_x measurements on May 4 and 8 can be found in Campos *et al.* [1998] and Talbot *et al.* [1998]. The main reason to choose these samples is that they had several cases of overlapping IN and AP collections, which allow comparison of compositional differences between the two populations, and represented samples from very different air mass types that are expected to have different chemical signatures.

4.2.1 May 4 flight

The DC-8 flight pattern on May 4 was to sample aircraft exhaust and short-lived contrails of a NASA Boeing 757 (B757) and a T-39 small aircraft. In order to coordinate with another ground based field mission (CART) in Oklahoma, all three airplanes flew in clear skies over a broken stratus deck. To get the exhaust samples, the DC-8 followed as close as 9 miles behind the B757. In the flight, the B757 alternately burned high and low sulfur fuels in its two engines. There were a total of four IN samples and one AP sample collected, with the AP sample taken during the last IN sample. The sampling times, along with information that describes the ambient conditions encountered, are shown in Table 4.1. During the first three IN samples, the DC-8 flew through exhaust and contrails most

Table 4.1: The sampling conditions of May 4.

Sample	Time(UTC)	CFD temp.(°C)	CFD SSi(%)	Flight description
IN-1	17:57:35-18:22:00	-31.4	47	Troposphere, 500 ft. below/in contrail
IN-2	18:31:20-19:25:00	-36.2	31	Near tropopause, in/out contrail
IN-3	19:27:30-20:35:00	-35.0	34	At tropopause, in/out contrail
IN-4	20:37:40-21:35:50	-36.2	38	In stratosphere, short time in exhaust
AP-1	20:49:00-21:09:00	-36.2	38	In stratosphere, short time in exhaust

of the time in the upper troposphere. The AP sample and last IN sample were collected primarily in the lower stratosphere without exhaust or contrails.

After normalizing by the number of particles analyzed, the chemical compositions of all five samples are shown in Figure 4.1. The fractions are the percentage of particles in each category. The total numbers of particles analyzed in each sample are shown inside parentheses. They represented on average 10% - 20% of the collected particles for IN, and 50% for AP. In the first three IN samples that were influenced by exhaust/contrail, metallic particles are the predominant group, while carbonaceous and crustal particles are the other two major ones. Combining the metallic and carbonaceous particles together, they comprised at least 65% of the IN in these samples, and up to 87% in one sample.

Another notable feature is that only small fractions of the IN were sulfate or mixed-sulfate particles. According to the discussions concerning heterogeneous ice formation in Chapter 1, aerosol particles need to be insoluble to serve as IN. X-ray analyses of these sulfate particles showed some of them were mixed with crustal components, suggesting the particle was at least partly insoluble. On the other hand, it may imply that the chemical requirement for heterogeneous IN is not necessarily that they be totally insoluble. Similar sulfate particles were also found in the IN samples on May 12.

Since the last IN sample was taken in the lower stratosphere not in the upper troposphere, it is difficult to simply compare it with the other three IN samples. Without being immediately influenced by aircraft exhaust, it had few metallic particles and was dominated by carbonaceous and crustal particles. A similar feature is observed in the two IN samples on May 12. The higher abundance of metallic and crustal particles in the UT IN samples, compared with the LS sample, is in qualitative agreement with reported relative UT/LS abundances for ambient aerosol [Sheridan *et al.*, 1994].

In Figure 4.1b, there are clear differences between the chemical compositions of IN and AP sampled in the lower stratosphere. Since the AP samples were obtained with a cascade impactor, composition results shown here are accumulated from all six stages, weighted for relative particle loading on each stage. The two dominant groups are the crustal and carbonaceous for the IN sample, and the sulfate and carbonaceous for the AP sample. The fractions of metallic particles are almost the same. While sulfate particles dominated the AP, they were less than 10% of the IN category. The sulfate particles left different patterns on the substrates: mostly round residues in the AP samples, and round residues with solid inclusions or discrete solid particles in the IN samples. These residues give us information about the phase states of the particles when they were impacted on to the substrate: the round residue is from liquid portions of the drop, and the inclusion and discrete solid particles suggest the liquid was mixed with an insoluble substance. With a pre-impactor inserted in the inlet flow, only those IN and AP below 2 μm were collected. One possible reason for the composition differences between IN and AP is from differences in the sizes of these populations. As we discussed in Chapter 1, both observations and

theoretical studies show that large particles are more likely to be IN than small ones. This is also confirmed by our soot ice formation experiments in Chapter 6. If the size were the only factor that decides the capability of nucleating ice, then the observed size distribution of IN would have shifted to larger size. As shown in Figure 4.2a, the peak size of the IN distribution is around 0.2 to 0.4 μm, and 0.8 to 1.0 μm for AP. The majority of AP consists of sulfate with large sizes, but sulfate particles are poor IN. Most crustal and carbonaceous particles were smaller, shifting the IN peak size to smaller diameters. In Figure 4.2b, the size distributions of silicates in IN and AP are plotted together. From these distributions, we conclude that large particles are favorable as IN, but this is not the case for sulfate particles although many of them were large (0.6 to 1.0 μm) relative to silicates. Hence chemical properties are more important than size in the ice nucleation process.

4.2.2 May 8 flight

The flight on May 8 was a coordinated mission of the DC-8, T -39, and ER-2 over Iowa and Wisconsin, west of Lake Michigan. The major event sampled during the flight was the cirrus anvil outflow from a mesoscale convective system. Six IN samples and two AP samples were collected, of which the third IN sample had a short time ($\sim$ 8 min.) in the lower stratosphere, and all the other samples were in the troposphere. The last IN sample collected during the descent until landing, is a collection from the middle troposphere to the ground. The sampling times and ambient conditions are shown in Table 4.2. Since the DC-8 spent most of its flight time in clouds, it is not surprising that clouds affected the first five IN samples and two AP samples. Thus these samples represent a composite of the IN characteristics of the total aerosol population and of the cloud interstitial particles.

Figure 4.3a shows the chemical compositions of all six IN samples. The crustal group becomes the second most abundant in relative number while the metallic group is the third, reversing their relative orders when compared with the in-contrail IN samples from May 4. The carbonaceous group is the largest category in all IN samples. Comparison of the two pairs of AP and IN samples (Figure 4.3b) reveals that more crustal and less sulfate particles were IN, and the relative fractions of metallic particles did not change dramatically, being in the same relative abundance characteristics as observed on May 4.

Table 4.2: The sampling conditions of May 8.

Sample	Time(UTC)	CFD temp.(°C)	CFD SSi(%)	Flight description
IN-5	17:21:14-17:58:00	-26.9	28	Cirrus, no contrail, tropopause
IN-6	17:59:50-19:08:08	-35.2	30	Turbulence, near tropopause
IN-7	19:10:54-20:13:00	-36.9	33	Thin cirrus, stratosphere
IN-8	20:16:00-20:40:52	-28.2	22	Tropopause, cirrus
IN-9	20:44:10-21:15:16	-31.3	30	Decent to 24K ft., clouds
IN-10	21:16:31-21:30:00	-29.2	35	Before landing
AP-2	18:55:00-19:08:40	-35.2	30	Out of clouds
AP-3	20:16:30-20:31:30	-28.2	22	Deep in clouds

Crustal and carbonaceous particles are the dominant IN classes, and account for 73% to 80% of the total, while the AP samples had larger number fractions of sulfate particles.

4.2.3 May 12 flight

On May 10, 1996, all the field measurement groups moved back to the NASA Ames Research Center in California. On May 12, the DC-8 flew over the Pacific Ocean, along the California and Oregon coasts, to sample its own long-lived loop contrail. The sky was covered by stratus clouds near the coast. The DC-8 flew in the troposphere most of the time. Two IN samples and one AP sample were collected: IN-11, IN-12, and AP-4. The IN-11 sample was collected within the old contrail in the upper troposphere, and the IN-12 sample in cirrus clouds. The AP-4 sample overlapped with the IN-11 sample. The sampling times and ambient conditions are shown in Table 4.3. Thus these samples represent a composite of the IN characteristics of the total aerosol population in the contrail

Table 4.3: The sampling conditions of May 12.

Sample	Time(UTC)	CFD temp.(°C)	CFD SSi(%)	Flight description
IN-11	20:51:00-21:45:00	-34.0	27	Thin cirrus clouds, tropopause
IN-12	21:53:00-22:23:00	-35.4	30	FL 31K ft., cirrus
AP-4	20:41:15-21:15:00	-34.0	27	Near tropopause

and of the cirrus cloud particles that were sampled by the inlet.

The comparison between the chemical compositions of IN samples on May 4 and 12 is presented in Figure 4.4a. The most significant feature is the relatively high abundance of sulfate-containing particles in the IN-11 sample on May 12. They account for up to 33% of the total number, while the fraction is below 16% in all May 4 IN samples. The likely reason is the combination of the old contrail and the strong influence of surface pollution in the West Coast. Among all the categories, the carbonaceous group is still the most important group, 40% and 63% in the two IN samples, respectively. Meanwhile, fewer crustal particles were found in the May 12 IN samples. It is most likely because of the marine origin of the sampled air and contrasts with the IN samples from May 4. In the cirrus clouds, fewer carbonaceous particles were collected than in the contrail. This suggests emission from jet engines as the source of carbonaceous particles. The metallic class is larger in the contrail sample than that in the cirrus cloud without influence of contrail, consistent with what we found in the May 4 samples. The compositions of the AP sample were dominated by 77% of all the 619 particles analyzed as sulfate, with other species present just as minor fractions, as shown in Figure 4.4b. The metallic fraction in the IN sample with overlapping sampling times was higher than the other IN samples, they agree with each other. Similar to what was deduced from the May 4 and 8 data, we conclude that pure soluble sulfate particles are less likely to form ice crystals under heterogeneous freezing conditions, while IN were enriched in carbonaceous and metallic particles. Another interesting issue is the absence of crustal particles in IN-11. There are two possible reasons for this observation. The first is that there were less crustal particles available in the AP sample, about 7.4% of the total population. Second, for the crustal category in the AP sample, many of those crustal particles were mixed with sulfate. As we discussed in the experiment section, they were put in the crustal group because the crustal species were the major component. It is possible that the sulfate coating disables the capability of these crustal particles to serve as IN; thereby, it lowers the number fraction of crustal particles.

A comparison of the metallic particle composition in the May 4 and 12 IN samples is shown in Figure 4.5. In all of these IN samples, Ti, Fe and Zn are the metals most frequently found, and can be related to jet engine materials, as well as to ground based

convection. Due to the resolution limits of EM, we cannot detect oxygen because of its low atomic number ($8 < 11$). It is possible that some of these metallic particles exist as oxides, not pure metal particles.

4.3 Summary and conclusions

The compositions obtained from our four AP samples are consistent in many common features with those reported by Hagen *et al.* [1994], Heintzenberg *et al.* [1996], and Sheridan *et al.* [1994]. One of the differences is from the relative abundance of sulfate: although sulfate particles dominated our AP samples, their fractions were not as large as those determined by Sheridan *et al.* [1994], in which only sulfuric acid particles were found on the TEM grids, but no other sulfate compounds. In contrast to the significant numbers of particles dominated by other species (e.g. crustal, carbonaceous) observed on our TEM grids, Sheridan *et al.* [1994] did not observe significant numbers of non-sulfate particles. The approach they used to analyze their TEM grids is different from ours. Since their TEM grids were heavily loaded, they sampled the deposit away from the central impaction spot. This introduces some uncertainty into their reported relative particle abundances, because the radial location of particles from the center of the impaction jet will vary with particle size and density [McInnes *et al.*, 1997]. The lighter particle loadings in our measurements mitigated this problem, but our AP abundances required a correction for the relative loading of particles on each of the impaction stages. After discussions with the authors of that paper, one possible explanation they provided is the impact of a volcanic eruption before the missions in which they sampled, producing an UT/LS aerosol heavily dominated by sulfur. This observation helps to resolve the discrepancy between our results.

In all our analyses, we applied a more detailed categorization than that shown here to group the particles. For the purpose of comparison with other researchers, we report here a composite into only five groups. Due to the relatively low number, soot particles were included in the carbonaceous category. When we looked at the number fraction of soot particles, their abundance in aircraft exhaust/contrail samples (May 4) was not as high as one might expect. Our analytical approach might be the reason for this discrepancy.

Limited by the EM, we cannot apply the EDS to particles smaller than 0.1 μm, whereas most of the soot number concentration was found in much smaller particles [Pueschel *et al.*, 1997]. Ström *et al.*[1997] reported a significant fraction of the cirrus residues that they sampled to be smaller than 0.1 μm; many of those particles would be missed by EM techniques. For all the IN samples, the peak sizes of IN were 0.2 to 0.4 μm. It is possible that this result is biased both by the 2 μm inlet pre-impactor and by the $\sim$0.1 μm threshold for EDS analysis. However, we conducted examination of several IN sample grids at higher magnifications ($\times$ 30,000) than used for the chemical characterization ($\times$ 10,000), and did not find many particles smaller than 0.1 μm.

There were clear differences in the composition of IN sampled in jet aircraft exhaust/contrails and in upper tropospheric air influenced by deep convection. A relatively larger number fraction of metallic and carbon-rich particles and smaller fraction of crustal particles were found in the exhaust/contrail samples. Based on the comparisons of the composition between the total aerosol and the IN fraction, we concluded that only a certain subset of particles serve as heterogeneous ice nucleating particles. Among the five categories, crustal and carbonaceous particles appear to be good IN, while sulfate particles are poor heterogeneous IN. Another interesting finding is the presence of partially soluble IN in our samples. It shows that the IN were not necessarily totally insoluble. In our samples, between a few and 25% of the IN exist as mixtures of sulfates and elements indicative of insoluble particles, with 10 - 70% of the particle volume estimated to be soluble. The presence of mixed soluble/insoluble IN can change the mechanisms of ice formation in cirrus clouds, and initiates phase transition to ice under totally different conditions [DeMott *et al.*, 1998]. Hence it is very important in studies of aerosol climate effects.

Continental and marine IN samples showed clear differences in their chemical compositions. While the continental IN sample contained 11 to 31% ($\pm$ 7%) crustal particles and less than 16% sulfate particles, the marine samples had less than 10% crustal particles, and 40% to 64% sulfate particles. As a metal widely used in building aircraft, Ti is a major constituent of the metallic particles.

a.

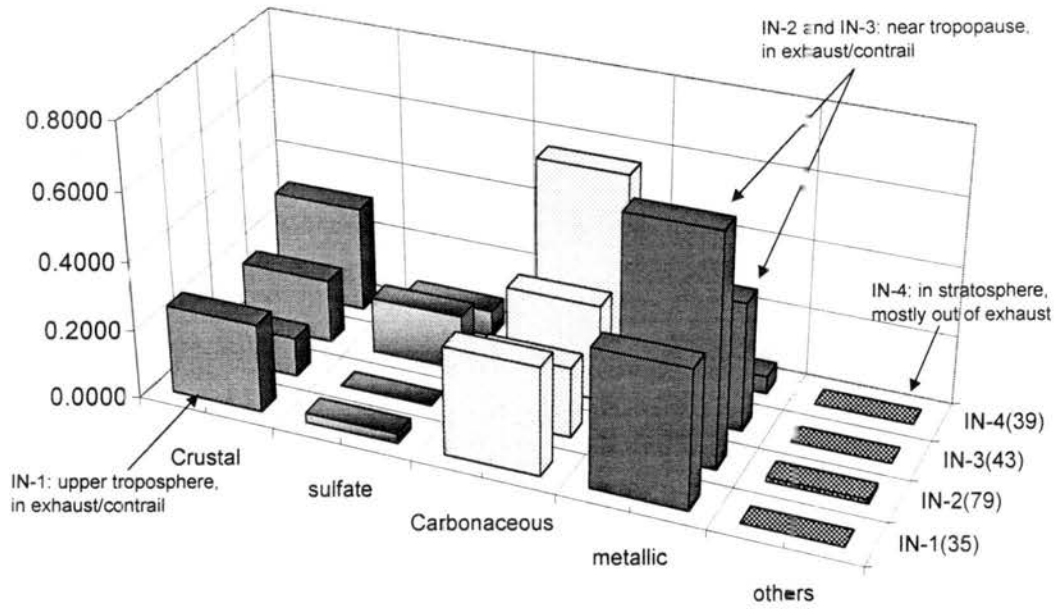

b

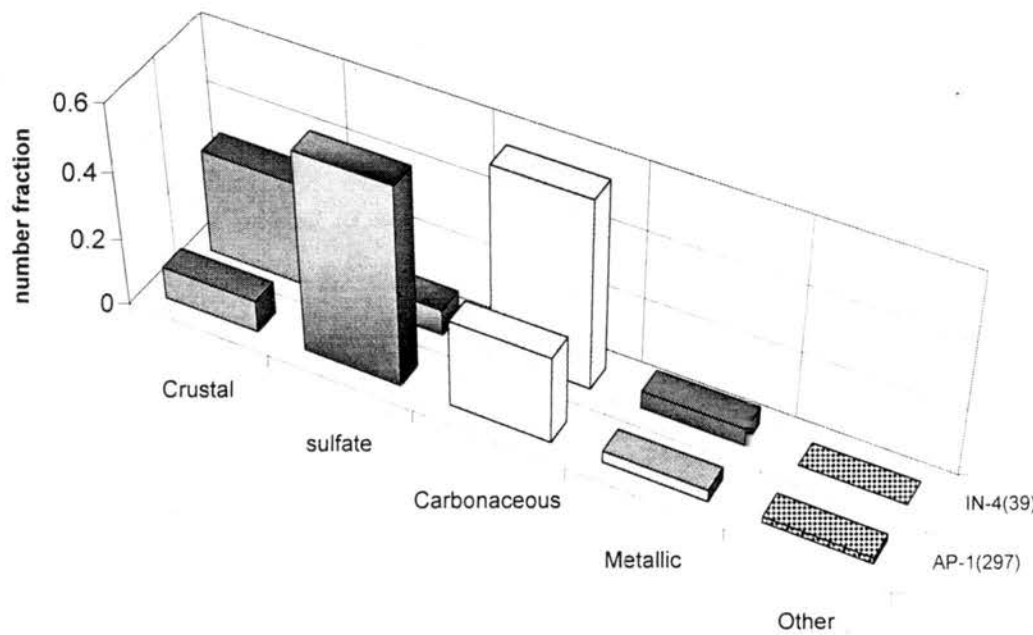

Figure 4.1: Chemical compositions of May 4 aerosol samples. (a) Ice-nucleating particles; (b) Comparison of overlapping IN and AP sample. Sample identifiers are as in Table 4.1; the number after each identifier indicates the number of particles examined in the sample. The ordinate is the number fraction of particles having the indicated composition.

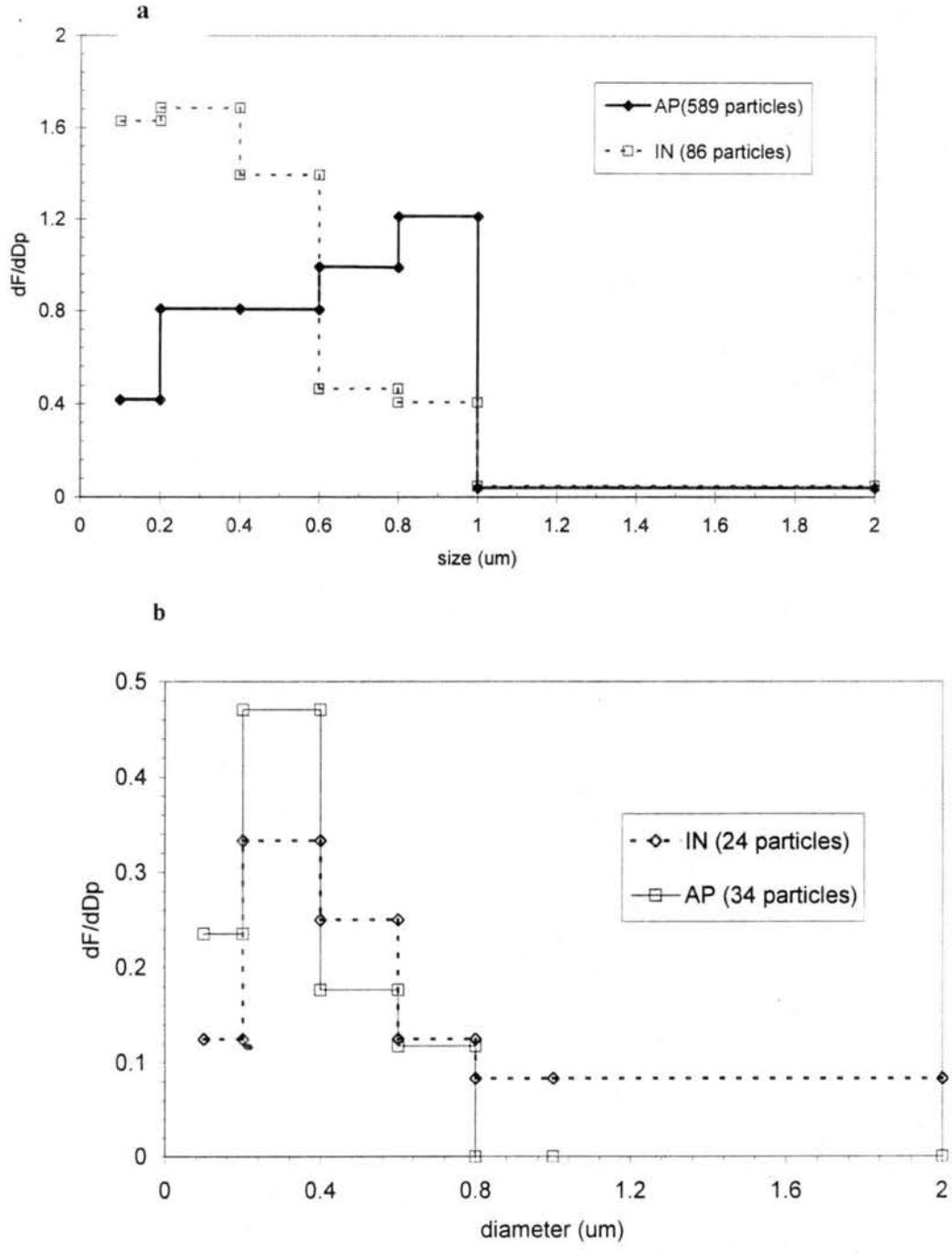

Figure 4.2: The fractional size distributions of May 4 aerosol samples. (a) IN-4 and AP-1; (b) dF/dDp represents the number fraction of aerosol particles in the size bin. Comparison of silicates in IN-4 and AP-1; Sample identifiers are as in Table 4.1; the number after each identifier indicate the number of particles examined in the sample.

a

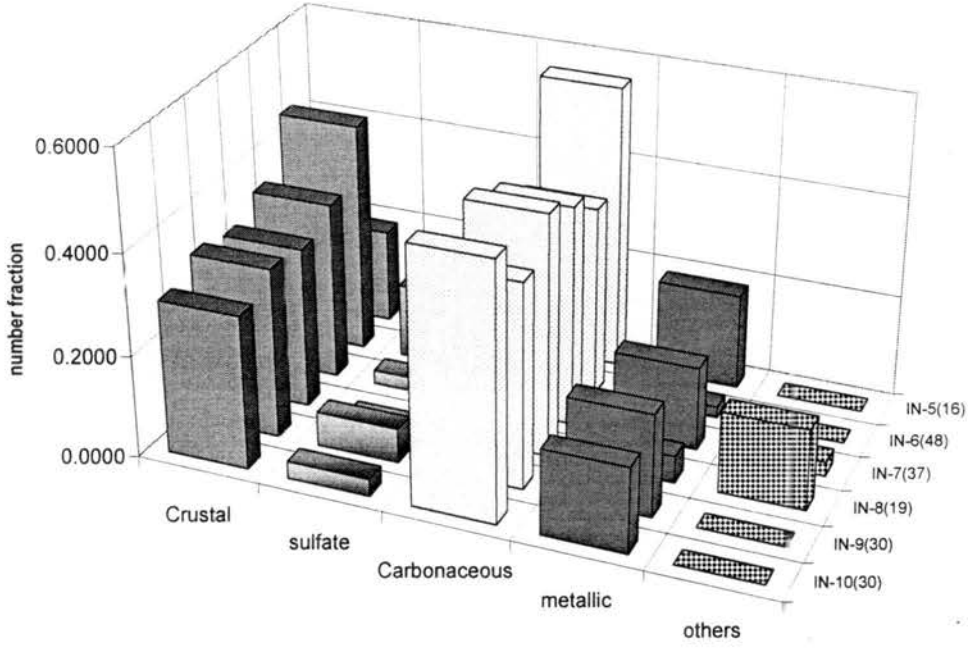

b

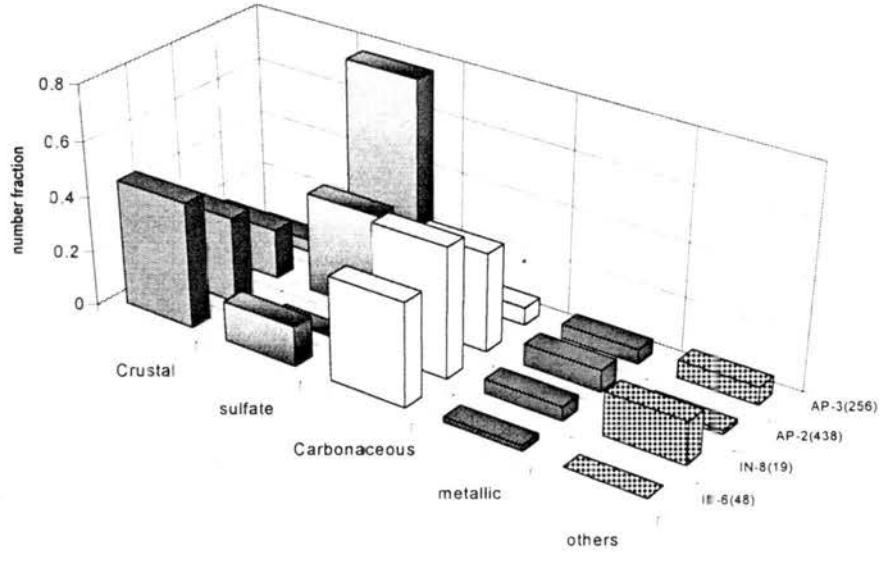

Figure 4.3: Chemical compositions of May 8 aerosol samples. (a) Ice nucleating particles; (b) Comparison of overlapping IN and AP sample. Sample identifiers are as in Table 4.2; the number after each identifier indicates the number of particles examined in the sample. The ordinate is the number fraction of particles having the indicated composition.

a

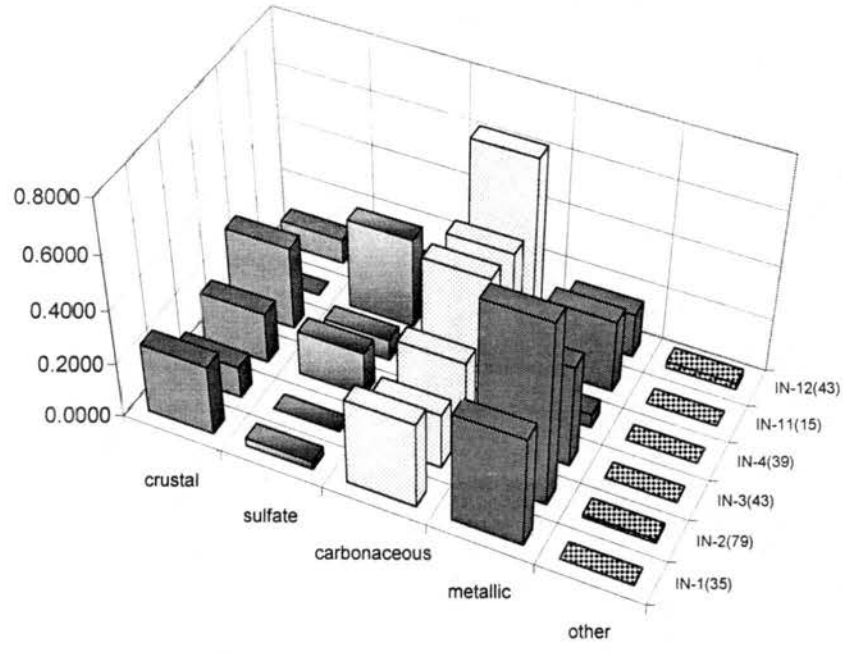

b

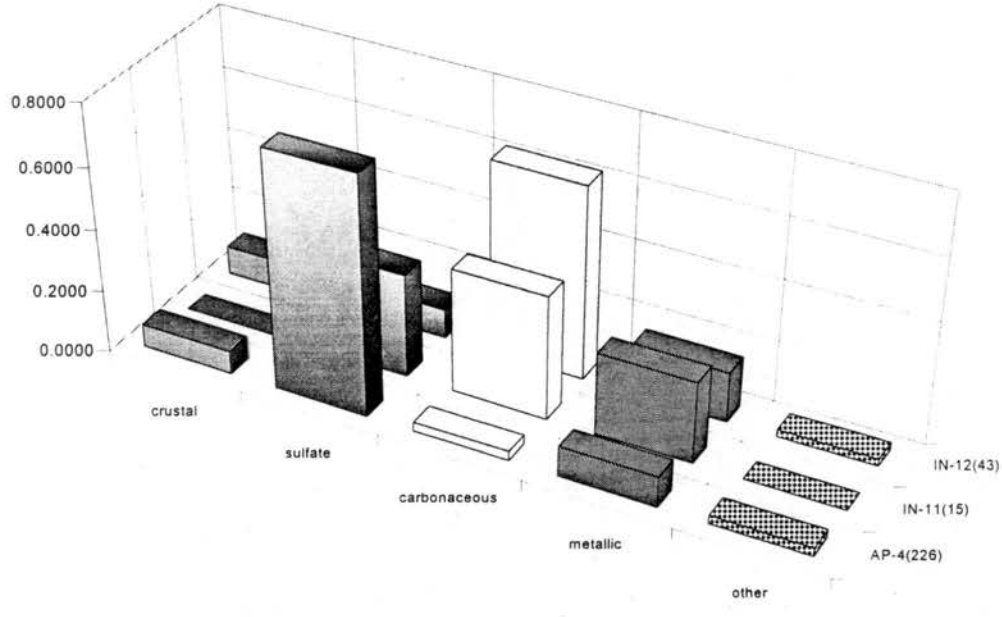

Figure 4.4: Chemical compositions of May 12 aerosol samples. (a) Comparisons between May 4 and 12 ice nucleating particles; (b) Comparison of overlapping IN and AP samples. Sample identifiers are as in Table 4.3; the numbers after each identifier indicate the number of particles examined in the sample.

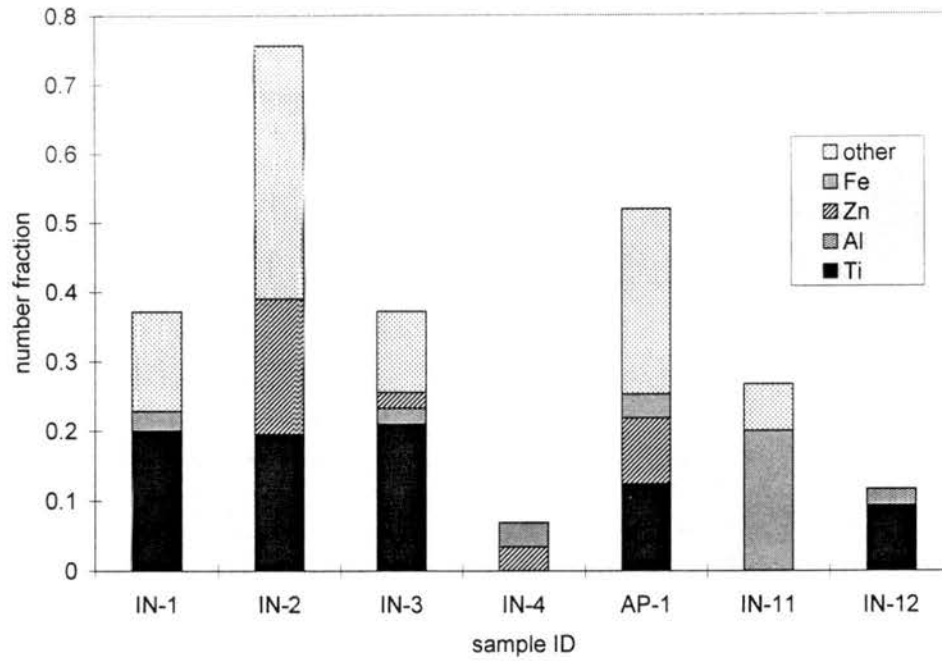

Figure 4.5: Chemical compositions of May 4 and 12 aerosol samples.

Chapter 5

HOMOGENEOUS FREEZING PROCESS – ICE FORMATION BY SULFATE AND SULFURIC ACID AEROSOL PARTICLES UNDER UPPER TROPOSPHERIC CONDITIONS

In the NASA SUCCESS field mission of 1996, aerosol particles in the upper troposphere were collected and analyzed by several investigators [Chen *et al.*, 1998, Twohy *et al.*, 1998, Talbot *et al.*, 1998]. The chemical and morphological analyses of collected particles show the presence of ammonia and sulfate in both bulk and individual aerosol compositions. The role which these ammoniated sulfate and sulfuric acid aerosols play in ice formation within cirrus clouds provided motivation for the studies described here.

To simulate the conditions in the upper troposphere, monodisperse particles were exposed to ice supersaturation in a thermal gradient diffusion chamber (CFD). Conditions in the chamber were selected to be relevant to temperatures and humidities in the upper troposphere. The apparatus detected the fraction of particles forming ice crystals as a function of these conditions.

5.1 Experiment description

5.1.1 Continuous flow diffusion chamber

In this paper, all ice formation experiments were conducted using the CFD III as described in Chapter 2. The 150 cm long chamber gives the sample a residence time above 12 s. Calculations show that this time is sufficient to achieve equilibrium between the particles and the ambient water vapor concentration and also potentially to freeze and grow as ice crystals. Starting from a few tenths of microns, ice crystals formed in the sample stream grow to a few microns inside the CFD, due to the tens of percent

super-saturation relative to ice in the sample stream. If the aerosols are exposed to sub-saturation with respect to water, they will deliquesce and equilibrate as haze droplets. Below their critical relative humidities for droplet activation, these few tenths of micron dry particles may equilibrate to haze droplet sizes a few times larger, but always well below one micron. Although earlier versions of CFD chambers had a low humidity section near the outlet to exaggerate the size difference between water droplets and ice crystals, no evaporation section was used in this CFD. Size distributions of all particles ($> 0.4\ \mu m$) were measured optically at the bottom of the CFD. The activated fraction was calculated from the number concentration of large ice crystals in the outlet stream. All conditions in the CFD, including sample location, temperatures, airflow rates, and other thermodynamic conditions were calculated in real-time and recorded by the data acquisition system. The data system also monitored and recorded pressures inside/outside the system, as well as the particle size spectra measured by an optical counter (Climet 7350A) over preset time intervals (12 seconds in this work).

5.1.2 Experiment configuration

Two generation systems were used to produce sulfate and sulfuric acid aerosol particles, respectively. The constant output atomizer and the sulfuric acid system were discussed in Chapter 2. Additional details of the configuration used to achieve aerosol particles of the desired size and number concentration are presented here. The setup of experiments is shown in Figures 5.1a and b. Clean dry air was passed through an atomizer (TSI 3076) to disperse an aqueous sulfate solution into small droplets. Solutions were made from reagent grade salts and deionized water at different concentrations, depending on the size of aerosol required. After the atomizer, the flow was temporarily heated to 60°C, and then moisture was removed from the air stream by a diffusion dryer (TSI 3062). To further reduce the humidity of the aerosol flow and to stabilize aerosol concentrations, the exiting flow from the diffusion dryer entered into a 5-liter glass jar, and was mixed with another dry airflow pre-cleaned by molecular sieves. The flow was then split, with one fraction discarded as excess and the other used as a poly-dispersed aerosol source for a Differential Mobility Analyzer (DMA, TSI 3071A). The same cleaned air source was used as the sheath flow in the

DMA. The size of the mono-dispersed output aerosol was selected by changing the voltage on the DMA inner column. The number concentration and dewpoint of the aerosol sample stream entering the CFD chamber were monitored, respectively, by a optical condensation particle counter (TSI model 3010) and a chilled mirror hygrometer (General Eastern 1211 optical dewpoint sensor). The dew point temperatures achieved in this system could be as low as -32°C, less than 2% RH_w at typical room temperature. Low humidity in the sample flow was important for preventing spurious relative humidity increases and for preserving the initial phase state of aerosol particles when they entered the cold inlet manifold of the CFD.

In selected experiments, the sample was passed through an optional pre-conditioning apparatus before entering the CFD. It consisted of two parts, a saturator and a pre-cooler. Two additional thermocouples were put into the outlet of the pre-cooler and the top of the CFD inlet region, respectively, to monitor the temperatures of the sample flow after the pre-cooler and immediately before it entered the CFD chamber. The saturator was operated at room temperature. It consisted of a Dewar bottle with deionized water in the bottom, stainless entry and exit tubes, and wicking material to distribute vapor inside the bottle. The purpose of the saturator was to elevate the humidity of the sample stream, deliquescing all sulfate particles into solution drops. This was a critical step in our experiments, since it was intended to investigate differences between ice formation by dry crystals and solution drops of ammoniated sulfates. Inside the saturator, the aerosol particles experienced a humidity around 90% RH_w, much higher than the deliquescence point of either sulfate aerosol. Such a high humidity ensured the existence of ammoniated sulfate (either ammonium sulfate or bisulfate) as solution drops.

In the absence of the pre-cooler, a humidified sample would cause spuriously high sample relative humidity and heavy frosting problems if introduced directly into the CFD. From vapor pressure equations given by Buck [1981], the water saturation vapor pressure at -30°C over super-cooled water is about 0.433 times that at 25°C. Thus with the same vapor pressure in the sample stream, the relative humidity would increase 2.31 times after cooling from 25°C down to -30°C. Assuming that the humidity after the saturator is 80%

RH_w, when the sample flow enters the CFD inlet region and adjusts itself to the colder conditions, the relative humidity inside the sample stream will increase rapidly to 185% RH_w. Although the aerosol particles only spend several tenths of a second in the inlet region, the high super-saturation leads to frost formation, which accumulates on the walls and in the small inlet slots.

The same situation could occur as the sample flow proceeds to the ice-coated region that is operated mostly below -45°C. In this region, the aerosol particles that dilute in response to the high RH_w could freeze under conditions that would not normally lead to freezing. Also, the water vapor from the highly super- saturated sample flow has to be depleted and deposits onto the cold wall. After hours of operation, frost particles will gradually enter the CFD flows, and overshadow the nucleation signals from aerosol particle ice formation. To remove the excess amount of water vapor from the sample stream, the pre-cooler was operated from -25 to -30°C before the CFD. The frost thus deposited on the walls of the pre-cooler instead of on the inside of the CFD. Ice that accumulated in the joint between the pre-cooler and the saturator had to be removed every ten to fifteen minutes when using the saturator/pre-cooler system.

Only experiments conducted after December 20, 1998 were operated using the saturator/pre-cooler system. The earlier experiments thus had some ambiguity as to whether the aerosol samples introduced to the CFD were crystalline salts or solution drops. The pre-conditioner was never used with sulfuric acid particles since these are known to be liquid down to very low relative humidity.

The sulfuric acid aerosol generator is described in Chapter 2. In this work, the sulfuric acid generator was operated at temperatures between 85°C to 105°C, to generate sufficient concentration of 16, 50, and 100 nm diameter sulfuric acid particles. Similar to the system used for ammoniated sulfate particles, a DMA was used to extract a monodisperse particle sample stream from the sulfuric acid generator. High purity nitrogen (4.8 grade, General Air Co.) was also used as the sheath flow for the DMA. The mono-sized sulfuric acid droplets from the DMA were sampled by the CFD.

5.1.3 Procedures

The detailed procedure used for experiments was discussed in Chapter 2. These procedures are summarized briefly here. The chamber was filled with clean, dry air, both walls of the chamber were cooled to -25°C, and the walls were coated with ice. Then the chamber walls were further cooled down to experimental temperatures. This is the initial point from which all experiments were started, and also corresponds to 100% saturation relative to ice, and sub-saturation relative to water. By varying the temperatures of both walls, the relative humidity was raised in steps of 2% to 3% RH_w, up to conditions of super-saturation relative to water. As the humidity was changed, sample temperatures were kept constant within ±0.3°C. In this way, the dependence of ice formation on both relative humidity and temperature was measured. A filter was inserted into the inlet flow or the DMA voltage was set to zero between measurements to monitor potential leaking and background ice crystals that can occur if frost develops somewhere within the CFD. Three experimental series were performed, for particles composed of $(NH_4)_2SO_4$, NH_4HSO_4, and H_2SO_4. Due to daily variation of aerosol concentrations input to the CFD, we report the fraction of the number concentration that froze, to make the measurements comparable.

In the first stage of experiments, aerosols were sampled by the CFD directly without any pre-conditioning. Some inconsistent results were obtained for ammonium sulfate and ammonium bisulfate. These results were related to variations in the dew point of the sample flows and could be grouped into two categories (see section 5.2.2). The pre-conditioning system was subsequently built to determine the impact of the initial phase state of particles on the freezing process. Experiments using the pre-conditioner constitute the second stage of tests. We compared experimental results under the same CFD humidity and temperature, with and without the pre-conditioner. These results from the different experiment stages will be discussed in the next section.

There are several advantages of using the CFD for the present investigations. Ice formation of liquid particles occurs at actual haze particle sizes, vapor supply is continuous to provide for ice crystal growth, and the device is a close relative to a field device for making similar measurements in the atmosphere. Therefore the homogeneous freezing mechanism

can be isolated, to identify the size effect on ice formation, and the comparison between laboratory experiments and in situ measurements made more meaningful. The ability to determine what fraction of the particle population nucleates under different conditions is another advantage.

One modest drawback of the technique used was the limited residence time. Sample aerosols had about 10 to 15 seconds to adjust themselves to ambient temperature, to nucleate, and to grow. Hence the combination of residence time and nucleation rates will impact the definition of the metastable ice transition regime, which is the focus of this work. The dependence of nucleation rate on temperature and humidity can be measured by varying the residence time of aerosol particles in the CFD chamber. Future experiments are planned to accurately measure nucleation rates, but they are not part of the research described here.

5.1.4 Evolution of solution drops, dry crystals and partially crystallized NH_4HSO_4 aerosols in the chamber

Before discussing the experimental results, it is helpful to describe the thermodynamic and compositional history of various aerosol particles in experiments and their potential effects on the results.

Solution drops

The processes happening inside the CFD are illustrated in Figure 5.2. Starting from the inlet, the first several tenths of seconds of residence time in the CFD are called the transition region, where the sample adjusts to temperature and flow. This transition region mainly consists of the inlet manifold and the top 1/10 of the cylinders. At the end of the transition region, the aerosol particles within the sample lamina are exposed to humidity in the CFD, and the particles grow toward their equilibrium sizes (at water sub- saturation) as regulated by the Köhler equation. This adjustment can take up to a few seconds, depending on particle size and the humidity condition. If the temperature is too warm to form ice homogeneously and if there are no foreign substances present to initiate heterogeneous freezing, these drops will remain unchanged at their equilibrium sizes through the CFD. That is what happened to completely soluble aerosol particles.

When the temperature in the CFD is below about -40°C, cold enough for homogeneous freezing nucleation of haze particles, the aerosol particles can undergo a different process. After the particles reach their equilibrium sizes, some ice embryos can be formed inside the drops. If this occurs, the meta-stable state of super-cooling inside the drops is broken. These ice embryos grow quickly into large ice crystals. As more liquid water freezes to ice, the concentration of the remnant solution will be limited by the drop temperature, which goes through a transient warming during freezing. The rate of crystallization is probably not related directly to the vapor diffusion although it will be affected by the concentration of salt ions. After completely freezing, the ice crystals grow rapidly because the environment is highly supersaturated with respect to ice (~40%). Ice crystals can grow as large as several micrometers at the bottom of the CFD, while the solution drops are still in the sub-micron range.

The above scenarios assume that the humidity and temperature profiles across the sample lamina are uniform. Since these profiles in fact vary with radial and axial position, some aerosol particles may experience stronger thermodynamic forcing and initiate the ice phase ahead of the others, and therefore have longer growth times. Those that form ice later will have less time to grow. The consequence of different growth times is a broadened size distribution of ice crystals, but not a well-defined size distribution. This has been observed in the OPC data. It is possible that some of the particles begin freezing near the end of the chamber and do not have enough time to grow, and are therefore incorrectly identified as drops when the OPC data are processed. To avoid underestimating the number of ice crystals, a longer residence time can be obtained by reducing flow rates or extending the length of the chamber. However, a critical flow rate is required at each temperature. Flow rates below the critical value lead to uncertainty in the calculated position of the lamina inside the CFD because of thermal buoyancy effects. Increasing the chamber length could exaggerate the temperature gradient along the walls, without special attention to coolant distribution. Operating the CFD at lower pressure lowers the critical flow rate, so this is a potential means for increasing residence times in future studies.

Dry crystals – $(NH_4)_2SO_4$

The mechanisms of ice formation by dry particles are very little understood from the measurements and observations currently available. Therefore the following discussions are mainly hypothetical. In this study, ammonium sulfate aerosol particles were the only ones that could be completely dried in the generation system. Therefore this discussion describes the evolution of the dry ammonium sulfate particles inside the CFD.

Dry ammonium sulfate particles were passed to the CFD whenever the preconditioner unit was not used or whenever the saturator was bypassed during use of the preconditioner. In either case, the sample flow had very low water vapor content ($<$ 1-5% RH_w at 20°C). Thus, the only difference in the two dry aerosol cases was that the pre-cooler lowered the temperature of the aerosol stream by up to 50°C in advance of the CFD transition region. This pre- cooling would extract any excess water vapor above ice saturation at -25 to - 30°C, and it would assure a temperature trajectory below the eutectic temperature (-19°C) in Figure 5.3(thin dotted line). In the absence of precooling, the temperature trajectory would also pass beneath the eutectic, except perhaps when the sample dewpoint temperature exceeded the eutectic temperature.

When the dry aerosols entered the low temperature and high humidity in the transition region, there are two possible pathways they could take: deliquescence followed by homogeneous freezing, or direct formation of ice by deposition nucleation. On the phase diagram discussed in Chapter 1 (Figure 5.3), the extrapolation of the deliquescence line below the eutectic point on the phase diagram is based on the assumption of meta-stable states that can exist in small aerosol particles. Since the trajectory of dry particles on the RH_w vs. temperature plot (thin dotted line in Figure 5.3) passes below the eutectic point, the temperature is too cold for deliquescence in the bulk phase. Nevertheless, the trajectory does cross the extended parts (dotted black lines) of both deliquescence and ice lines. If the dry particles do deliquesce and freeze to ice, their ice formation onset conditions would be expected to be similar to those of the solution drops or to follow the extrapolated deliquescence line at low temperatures. On the other hand, deposition nucleation is primarily driven by the supersaturation with respect to ice (SSi) [Huffmann,

1973]. Depending on the surface properties of dry particles, water vapor will deposit, and form ice crystals at relatively high humidities, otherwise the nucleation rate would be too low to produce enough ice embryos. In this situation, the SSi will play an important role in the ice formation.

Partial crystallization – a possibility in the bisulfate system

Dehydration of liquid ammonium bisulfate aerosol particles differs from drying ammonium sulfate in an important way. Based on recent thermodynamic models [Clegg *et al.*, 1998] and laboratory vapor pressure and bulk phase measurement [Chelf and Martin, 1999; Yao *et al.*, 1999], drying of ammonium bisulfate at temperature below 310 K produces particles that are partially crystallized in a mixture with solution. This mixture was determined to contain letovicite ($(NH_4)_3H(SO_4)_2$) and a remaining liquid that was acidified from the bisulfate composition. These results were not available when the initial series of tests were conducted. The tandem differential mobility analyzer (TDMA) studies in the CSU laboratory [Brechtel and Kreidenweis, 1999] conducted after the first series of ice formation tests (without the pre-cooler), indicated the presence of letovicite in the dried bisulfate aerosol from the generation system used in the present study. This determination was based on the observed deliquescence RH_w at room temperature. This means that the liquid phase line for the bisulfate system is that for letovicite. The eutectic temperature of the bisulfate system is -31°C [Chelf and Martin, 1999].

The multiphase nature of bisulfate aerosols generated in this experiment complicates the results, especially for those experiments conducted without the preconditioning system. It is more likely that the generated bisulfate aerosols had a thermodynamic trajectory upon entering the CFD that crossed the deliquescence line at a temperature warmer than the eutectic, leading to the dissolution of letovicite in most cases, but with some partially crystallized cases. Pre-conditioning by the saturator and precooler should have led to the same situation of pure solution drops as discussed in the previous section. When precooling was used without the saturator, it was likely that the aerosol particles crossed the deliquescence condition below the eutectic temperature. Here the question of deliquescence of aerosol particles under cold temperatures is the same as those in the previous section.

5.2 Results and discussion

Three series of experiments were conducted with monodisperse aerosol particles: 0.2 μm ammonium sulfate, 0.2 μm ammonium bisulfate, and 0.05 μm sulfuric acid particles. As discussed in Chapter 2, with our experimental configuration, the 0.2 μm "monodisperse" aerosol particles contained 51% of 0.2 μm, 33% 0.32 μm, and 16% 0.43 μm particles. For 0.05 μm sulfuric acid drops, the doublets and triplets were 0.072 μm and 0.1 μm, respectively, and the percentages of singlets, doublets, and triplets were 90%, 9%, and 1%. The impacts of doublets and triplets on the homogeneous freezing experiments were discussed in section 2.3, and will not be discussed here. The existence of multiply charged particles complicated the interpretation of ice formation results to some degree. The likely effect of multiples was the onset conditions for ice formation were probably dominated by the largest particles, especially in the cases of the ammoniated sulfates. All multiplet sizes probably contributed to the total ice formation at higher activation fractions. Compensation for this factor in analyzing and interpreting results in discussed in the following. Prior to discussing the results, it is instructive to consider what happened to solution drops and dry particles inside the CFD under the experimental conditions.

The activated fraction was used as an indicator to represent the ice formation conditions. The activated fraction is the ratio of the ice crystal number concentration counted by the OPC divided by the input aerosol number concentration. In all experiments, 0.1%, 1%, and 10% activated fractions were determined. The 0.1% activated fraction was defined as the onset conditions for ice formation. At this level, it may not be possible to rule out a contribution from heterogeneous ice nucleation by contaminants within the reagent grade sulfate salts and deionized water used experiments. However, based on the low level of heterogeneous contamination noted by DeMott and Rogers [1990] for cloud droplets formed on similar aerosols and the fact that solutions were remade on a regular basis, we believe that heterogeneous effects were not significant even at the 0.1% activation level.

The residence time was assumed to be long enough for solution drops to reach equilibrium at all temperatures. Numerical calculations show that aerosol particles require at most several seconds to establish equilibrium with the surroundings, this time depending

on the mass of the particle, temperature and RH_w of the chamber. Experiments with lower flow rates (longer residence times) also confirm that the size distribution of solution drops does not change within the resolution of the OPC. This is the experimental proof that the residence time is sufficient for drops growing to size defined by Köhler equation.

One of the uncertainties is the growth rate under different temperatures and humidities. Previous theoretical study shows the exponential relation between the nucleation rate and temperature. So far there is no such information available in the temperature range -40 to -60°C. Estimation of nucleation rates from data obtained in this study, will be the topic of a future project, involving more numerical calculations.

5.2.1 Results from the experiments

There are a total of 101 tests conducted between -20°C to -60°C discussed here: 35 tests with 0.2 μm ammonium sulfate, 48 tests with 0.2 μm ammonium bisulfate, and 13 tests with 0.05 μm sulfuric acid. Several other sizes were selected to test the size effects of aerosol particles. The experiments, corresponding dates, and observed activated fractions are listed in Table 5.1. In the tables, all the experiments with pre-conditioner are underlined at the date. Those experiments without pre-conditioning are grouped as solution drops or dry crystals (low humidity in the case of bisulfate), depending on the comparison with pre-conditioned results. For example, there are a total of 8 tests with ammonium sulfate at ~60°C, 5 of them belong to the first stage of experiments without pre-conditioning. Considering the 0.1% activation conditions, 4 of them are between 82.5% to 84.5% RH_w, the other one is 94% RH_w. The three pre-conditioned experiments show that solution drops activate at 80% and 83% RH_w, dry crystals at 96% RH_w. It is clear that four of the tests with no pre-conditioning can be fitted into the group of solution drops, and the last one is dry crystal. Even from the viewpoint of statistics, the 94% RH_w sits outside of the other four, and can be distinguished with confidence. Basically, the ice onset in the low humidity pre-conditioning tests occurred at about 5% to 11% RH_w higher as compared to solution drop cases. More detailed discussion will be given in section 5.2.1.1. Since fewer cases at low humidity are available, only the onset conditions of solution drops are analyzed in the following discussion.

These laboratory ice formation results now will be related to the formation of cirrus cloud in the natural atmosphere, and also compared to experimental observations from other published studies.

$(NH_4)_2SO_4$

From the discussion in section 5.1.4, there are two possible mechanisms for the ice formation by $(NH_4)_2SO_4$ particles in the CFD and in the atmosphere: homogeneous freezing of solution drops and deposition nucleation by anhydrous particles. As the experiments were initially conceived (during the first stage of experiments), it was expected that when dry ammonium sulfate crystals were provided to the CFD, a consistent result would be achieved that reflected the fact that particles either deliquesced or remained dry in response to the set CFD conditions. It later became apparent that variability in the initial RH_w of the air provided to the CFD might actually have altered the phase state of the particles during the rapid cooling at the entry to the CFD. There were a total of 18 tests of ammonium sulfate without any pre-conditioning. Ten of these are more representative of dry crystals to the CFD on the basis of later pre-conditioned results.

To understand how the phase states of aerosol particles affect their ice formation behaviors, we need to go back to the thermodynamic phase diagram of ammonium sulfate (discussed in Chapter 1, and in section 5.1.4). The binary system is understood to be in equilibrium for the bulk system, but not for the meta-stable regions below the eutectic point. In the meta-stable region, there seems no physical reason not to extrapolate the ice line and the deliquescence lines to lower temperatures, despite some recent assertions to the contrary [Imre *et al.*, 1997; Tabazadeh and Toon, 1998] The position of the ice line is well known at lower temperatures. The position of the deliquescence line is not. If the temperature dependence of the deliquescence line can simply be extrapolated colder than the eutectic point, then initially dry particles at low temperature could deliquesce at high enough RH_w. Otherwise, the only mechanism to form ice would be direct deposition nucleation without any freezing processes.

The measurements of wet/dry aerosols are shown in Figures 5.4 and 5.5. Experiments conducted without the pre-conditioner are plotted as filled marks, and those pre-conditioned as empty marks. The freezing behavior of wet aerosols agreed with some of

the data in the initial experimental series with no pre-conditioner, while the behavior of initially dry particles agreed with some other early experiments. The onset of ice formation (corresponds to 0.1% activation, empty circles in Figure 5.4) is close to the $\lambda = 1.0$ line, defined for 0.2 μm dry size particles using equations (1.1) to (1.3), the Köhler equation (A.3) and $J_{hf}(T)$ from DeMott *et al.*[1997]. The cumulative effects of the multiple particle sizes were considered in making these calculations. Water activity was taken from the model of Clegg *et al.*[1998] in determining the equilibrium size and volume of particles at different RH_w conditions. The 1% activation result (triangles in Figure 5.4) agrees fairly well with the degree of supercooling proposed by Sassen and Dodd [1988], that is $\lambda = 1.7$ line. When relating the results for solution droplet freezing to cirrus cloud formation conditions, the degree of supercooling required for ice formation mostly exceeds the depression of the melting curve by 38°C (T_{hf0}), even more so at lower RH_w (higher solute concentration).

Particles that were pre-cooled only and thus should have remained dry, required higher RH_w than wet particles to form ice. The onset of ice formation (0.1% activation as diamonds) is shown in Figure 5.5. The humidities required by the dry particles are about 8% to 10% RH_w higher than those of droplets at the same temperature. At -60°C, the SSi is 67% for the onset of ice formation on dry particles. If this case represents deposition nucleation, these results indicate that dry 0.2 μm ammonium sulfate particles are very poor heterogeneous ice nuclei. If the ice formation mechanism is homogeneous freezing nucleation, then deliquescence is impeded for some reasons toward higher RH_w from the condition expected based on the model of Clegg *et al.* [1998] or a simple linear extrapolation of the existing experimental deliquescence RH_w results to these low temperatures. Otherwise, results would be expected to follow the "wet" case at all temperatures for which the onset RH_w of wet particles exceeded the deliquescence RH_w. Nevertheless, the results of dry ammonium sulfate particles might be evidence to support the predictions by Tabazadeh and Toon [1998], which suggested that no deliquescence would happen below the eutectic point.

These experiments demonstrate that the initial experimental series without the precooler had a wider variation of results. Apparently, the particles were deliquescing in some

cases and not in others. The state of the particle was sensitive to the thermodynamic path in going from dry room temperature conditions to humid low temperature conditions and the net result was not very predictable.

The results of other laboratory studies of ice formation from $(NH_4)_2SO_4$ particles are also shown in Figure 5.4. In both studies, sub-micron particles were used. The data from Detwiler [1980] were obtained in a static diffusion chamber using $(NH_4)_2SO_4$ particles of unknown phase state. His results for 1% ice activation are consistent with the freezing conditions of wet sulfate aerosols within the uncertainty of measurements. In particular, Detwiler [1980] noted the deeper supercooling with respect to the bulk phase needed to nucleate particles below - 50°C. In contrast, the flow tube experiments on wet $(NH_4)_2SO_4$ from Cziczo and Abbatt [1998] indicate ice formation at much lower relative humidity and decreasing degrees of supercooling with respect to the bulk phase as temperature lowers and droplets become more concentrated. That their results fall above the $\lambda = 1$ curve, appears to indicate an ordering effect of the solute on homogeneous freezing of solution droplets. This is contrary to the expected solution effects on freezing. The current results for the onset of freezing wet ammonium sulfate particles agree with Cziczo and Abbatt [1998] down to about 88% RH_w and then deviate to follow the $\lambda = 1$ line.

NH_4HSO_4

Experiments with NH_4HSO_4 aerosols could also be separated into two categories based on insights provided by later pre-conditioned experiments. The results of experiments are shown in Figures 5.6 and 5.7. The approach and experimental process were exactly the same as for the ammonium sulfate experiments, except that it was envisioned that the particles would be partially crystallized at low RH_w in our generation system, as discussed in Section 5.1.4. In the 44 experiments with 0.2 μm particles, there were 30 tests without any pre-conditioning (shown as filled marks); 14 tests were with controlled phase states (as empty marks). Among those without pre-conditioning, only six of them were suspected to reflect the partially crystallized phase state of particles generated at low humidity. This is consistent with the lower temperature and humidity of the eutectic point of ammonium

bisulfate compared to that of ammonium sulfate. In the other 24 cases, liquid bisulfate was presumed to be present after particles adjusted to the set CFD conditions.

There are some variations from test to test. The experiments with the pre-conditioner confirmed that different ice formation behaviors were related to differences in the phase states of ammonium bisulfate particles. With the saturator, the aerosol particles should have been retained as fully liquid drops without partial crystallization before entering the pre-cooler. At the outlet of the pre-cooler, the temperature and humidity of the sample stream is still above the eutectic point of NH_4HSO_4 - H_2O system, which ensures the particles are drops. These drops began to freeze (0.1% activated fraction) along a line defined by $\lambda = 1$ in equation (1.1) at temperature above -50°C. No impact of the requirement for dissolution of letovicite is detected in this case, since it never formed in the fully liquid drops. Similar ice formation behaviors were noted between wet or deliquesced ammonium bisulfate droplets and ammonium sulfate droplets. Perhaps this is not surprising since the homogeneous freezing process is responsible for ice formation in each case and the ionic compositions inside solution of $(NH_4)_2SO_4$ and NH_4HSO_4 are similar.

The situation was complicated in the experiments without the saturator but with the pre-cooler. These partially crystallized solution droplets of letovicite with acidic ammonium bisulfate required much higher RH_w for the onset of ice formation. Freezing didn't happen until water super-saturation at temperatures higher than -50°C and required RH_w above, 95% between -50°C to -60°C. With the information available, we cannot tell if the acidic solution ultimately freezes completely or if the dissolution of letovicite did not occur or if it is time dependent at relative humidities above the extrapolated deliquescence RH_w. In the latter case, longer residence time might be needed. Additionally, heat is released when concentrated sulfuric acid is diluted. The dilution warmed up the particles, therefore inhibited the homogeneous freezing mechanism at low humidity. Of course, the degree of crystallization of letovicite produced by the drying process could play a role. Low humidity crystallizes more letovicite, leaving a strongly acidic solution; high humidity generates less letovicite, and less acid in solution. In the extreme circumstance, only letovicite co-existed with a pure sulfuric acid shell.

H_2SO_4

Under ordinary laboratory conditions, sulfuric acid drops cannot be crystallized. Therefore the pre-conditioner was not needed for H_2SO_4 experiments. Investigations were conducted on ice formation with 0.05 μm monodisperse sulfuric acid droplets, as shown in Figures 5.8 and 5.9. Other sizes, from 0.016 μm to 0.1 μm, were also tested in a few cases, for the purpose of investigating the size effect on our results. It is infeasible to generate 0.2 μm sulfuric acid particles for comparison with ammoniated sulfate experiments with the sulfuric acid generation system used. The 0.05 μm sulfuric acid size is consistent with the observations of young aircraft exhausts [Schumann *et al.*, 1996], and are representative of tropospheric sulfuric acid drops generated via gas-to-particle conversion. Therefore the results are directly relevant to formation conditions of aircraft contrail, as well as formation of cirrus clouds. Applying the same procedure as for the ammoniated sulfate experiments, the conditions for 0.1%, 1%, and 10% activation freezing fraction were measured at -40°C, -45°C, -50°C, -55°C, and -60°C. As an example, the results for 0.05 μm diameter sulfuric acid particles are shown in Figure 5.8. Below -50°C, the data show that there was a 5% to 6% relative humidity increment between the conditions for activating 0.1% and 10% of particles as ice crystals in the CFD residence time. At -60°C, only 1% of the initially 0.05 μm sulfuric acid droplets are activated at 88.5% RH_w in the time available. At warmer temperatures, ice formation in these H_2SO_4 particles requires higher RH_w than for 0.2 μm liquid $(NH_4)_2SO_4$ and NH_4HSO_4 aerosols.

The degree of supercooling of $(NH_4)_2SO_4$ particles determined in the current study is greater than in Bertram *et al.*[1996], who used 0.4 μm particles. From Figure 5.9, our results for 0.05 μm sulfuric acid particles agree better with Koop *et al.*[1998], excepting that these authors studied much larger liquid particles. A consideration of size effects in homogeneous freezing as revealed by the present studies is given in section 5.2.3.

5.2.2 Statistical analysis

To conduct a statistical analysis of these data, the 0.1% activated fraction data were chosen because there are more data points than for the 1% or 10% fractions. To ensure the

sample standard deviation (s) are similar to the population standard deviation (σ), at least 20 replicates are needed. However, the experiments are time-consuming, so replicates of 20 independent tests under single conditions were not practical. Instead, with the assumption of the same sources of indeterminate error in all the experiments, pooled standard deviations are calculated on data from an accumulated series of tests. The equation for the pooled estimate of the standard deviation is [Skoog *et al.*, 1996]

$$s_{pooled} = [\frac{(s_1^2 \times (N_1 - 1) + s_2^2 \times (N_2 - 1) + s_3^2 \times (N_3 - 1) + ...)}{(N_1 + N_2 + N_3 + ... - N_s)}]^{1/2} \tag{5.1}$$

where N_1 is the number of data in set 1, N_2 is the number in set 2, and so forth. The term N_s is the number of data sets that are being pooled; s_1, s_2, ..., s_n are the sample standard deviations of the data in sets 1, 2, ..., n.

In the current experiments, it is difficult to estimate the population standard deviation of σ in RH_w accurately because of the relatively low number of degrees of freedom. Therefore, the Student's t test [*e.g.*, Skoog *et al.*, 1996] was used to calculate the confidence limits. The standard deviation calculated in this way from a small set of data may be quite uncertain. Thus the confidence limits are necessarily broader.

To account for the variability of the standard deviation, the statistical parameter t is defined as

$$t = \frac{x - \mu}{s} \tag{5.2}$$

where μ is the mean value, s is the pooled standard deviation, and t depends on the desired confidence level and the number of degrees of freedom N in the calculation of the standard deviation. The confidence limit can be calculated as

$$CL \ \ for \ \ \mu = \bar{x} \pm \frac{ts}{\sqrt{N}} \tag{5.3}$$

In the following calculation, the results were grouped according to temperature. The precision of the temperature measurement has ±0.6°C uncertainty at 95difference of 1.2°C represent the same conditions. With 1°C defined as the critical temperature difference to distinguish among groups, results with a temperature difference above 1°C were treated as a different group. The statistical technique was applied to the 0.1% activated fraction

of the ammoniated sulfate and sulfuric acid results to give the results in Tables 5.2 to 5.6. One thing to keep in mind, because of the grouping criteria, some data points cannot be included in the pooled standard deviation, but they are included in the plots of data, since they contribute to our understanding of the tendencies. Of course, they increase the confidence level, which cannot be seen from the calculation. The variability in temperature uncertainty impacts the grouped statistics results too, because although different results are treated together, they were not obtained under exactly the same conditions.

It was suspected that one of the sulfuric acid experiments on Nov. 13, 1998 was anomalous. The Q test for outliers was used here to check if this one is an outlier [Skoog *et al.*, 1996]. The nearest result is RH_w 90.1%, the difference in RH_w is 4.9%, and the widest spread in RH_w of the entire set is 9.5%.

$$Q_{exp} = \frac{|x_q - x_n|}{width} = \frac{4.9\%}{9.5\%} = 0.516 \tag{5.4}$$

where x_q is the questionable result, and x_n is its nearest neighbor, and width is the spread of the entire set. Here we have 7 measurements, with Q_{crit} of 0.507, 0.568 and 0.680 for confidence levels of 90%, 95% and 99%, respectively. Because $Q_{exp} > Q_{crit}$ at the 90% confidence level, we will not include that result in the following calculation.

Since ammonium sulfate and sulfuric acid are two different compounds with significantly different phase diagrams, and different sizes were used, it is possible that the ice formation conditions are not the same. Hypothesis testing was used to judge whether the experimental data support this hypothesis. In this test, if the observed difference in ice formation conditions is greater than or equal to the difference required, it will be considered questionable to assume the two groups of data are the same.

More specifically, it was judged whether the difference in the conditions of the ammonium sulfate and sulfuric acid measurements was real, and constitutes evidence that the behaviors of the samples are different. Since the data were collected in an identical way, it is reasonable to assume that the standard deviations of the two measurements are the same. If we assume that the pooled standard deviation of these two sets of experiments is a good estimate of both individual pooled standard deviations, we find that

$$RH_{sulfate} - RH_{sulfuricacid} = \pm t s_{pooled} \left[\frac{(N_{sulfate} + N_{sulfuric\ acid})}{(N_{sulfate} N_{sulfuric\ acid})}\right]^{1/2} \tag{5.5}$$

If the humidity difference is smaller than the computed value, there is no difference between the onset condition for ice formation from ammonium sulfate and sulfuric acid particles; otherwise, there is a distinguishable difference. The value of t is decided by the confidence level. The higher the confidence level, the larger the difference that is required to pass the test. From the viewpoint of chemistry, a 95% confidence level is generally acceptable. In the following, the tests are applied to the onset relative humidities (0.1% activated fraction) at individual temperatures.

First, the pooled standard deviation of the ammonium sulfate and sulfuric acid experiments is

$$S^2_{pooled} = \frac{[s^2_{pooled,sulf}(16-5) + s^2_{pooled,acid}(12-4)]}{(16-5+12-4)} \tag{5.6}$$

$$S_{pooled} = 1.3\% \tag{5.7}$$

The right-hand side of equation 5.5 computed at various confidence levels is compared to the expected difference between the means in Table 5.7.

From these calculations, it is concluded that at -45°C, -50°C, and -60°C, there are differences between the ice formation behaviors of 0.05 μm sulfuric acid and 0.2 μm ammonium sulfate haze particles at the 99% confidence level. Differences are seen at the 90% confidence level at -55°C. Generally, we conclude that there are differences between the ice formation conditions between 0.2 μm ammonium sulfate and 0.05 μm sulfuric acid at least at the 90% confidence level.

The confidence level of the difference between ammonium bisulfate with the other two compositions is not analyzed, because of the new phase present in the binary system, which generates a systematic difference. The details will be discussed in the next section.

To compare the difference between the 0.1% and 1% activation, the same steps above are followed to compute the standard deviations for the 1% activation results. These are shown in Table 5.8.

The pooled standard deviations for 0.1% and 1% with ammonium sulfate are 1.4% and 3.2%, respectively. Using equation 5.1, the pooled standard deviation for 0.1% and 1% activation is 2.3%. Similarly, the pooled standard deviation for 0.1% and 1% activation results for sulfuric acid is 1.3%. Applying the hypothesis test to these results, as shown in

Table 5.9, shows that differences between the 0.1% and 1% activated fraction exist only at the 80% confidence level.

Table 5.10 shows the hypothesis test results with the 1% activation of ammonium sulfate and sulfuric acid experiments. The pooled standard deviation of these two groups can be calculated with equation 5.2 as 2.6%. Only the results at -50°C passed the hypothesis test at 95% confidence level, whereas at -60°Cdifferences did not exist even at the 80% confidence level.

5.2.3 Comparison of different compositions and size effects on homogeneous freezing nucleation

To understand the role of particle size in ice formation, some additional experiments were conducted. Some experiments on sulfuric acid are shown in Figure 5.10. The onset freezing conditions (F = 0.001, or 0.1% activated fraction) of 0.05 μm particles are compared to those of polydisperse particles with a lognormal mode diameter of 0.016 μm and a geometric standard deviation (σ_g= 1.8). The 0.05 μm sulfuric acid particles are frozen relatively easier, either at warmer temperatures or at lower relative humidities. The differences of experimental results and theoretical calculation showed nice agreement, as plotted in Figure 5.10. The theoretical curves are based on the average experimental λ value used in equations (1.2) and (1.3).

The value of λ was calculated as follows. Given the mass of the initial "dry" particle, the concentration and the equilibrium size of the haze drop was calculated with the Köhler equation (A.3) at different relative humidities, with water activities from the model of Clegg *et al.* [1998]. For a chosen value of λ, the homogeneous nucleation rate $J_{hf}(T^*)$ was calculated [*i.e.*, DeMott *et al.*, 1997] at the effective temperature (T^*), and was used to define the activated fraction (F in equation (1.3)). Through several iterations, λ values for different F (0.001, 0.01, and 0.1 values) were determined at the experimental RH_w values. The average λ ($\pm$95% confidence interval) of 0.2 μm ammonium sulfate, 0.2 μm ammonium bisulfate, and 0.05 μm sulfuric acid particles were 1.75$\pm$0.35, 1.38$\pm$0.34 and 1.98$\pm$0.27, respectively. Since ΔT_m is the same for every substance as a function of water activity, these three similar values of λ suggest that the statistically significant difference between

the RH_w at which sulfuric acid and ammoniated sulfates froze in the previous section can be largely explained by the difference in particle sizes.

The mean value of λ of bisulfate (1.38 ± 0.34) is smaller than those of the other two compounds. The large standard deviations of the λ values decrease the confidence levels to distinguish the ice formation behaviors of ammonium bisulfate from those of the other two substances. Calculations showed 90% and 70% confidence levels to conclude that there are differences between ammonium sulfate and sulfuric acid, bisulfate and sulfuric acid. Calculation of λ based on data from another study on the freezing temperature of ammonium bisulfate drops [Koop *et al.*, 1999] showed a mean λ value of 2.3.

The calculations of λ for each data point also gave the equilibrium composition (in weight %) of solution drops; thereby, the values of ΔT_m could be determined (*via* Clegg *et al.*, 1998). Euqation (1.1) then gives the freezing point depression (ΔT_{hf}) for each data point. With $\Delta T_{hf} = T^* - T$, the results are plotted in Figure 5.11 as the freezing point depressions vs. the melting point depression. Different activated fractions for each substance are distinguished from each other by different symbols. The variation of λ value of sulfuric acid particles was almost independent of activated fraction. This agrees nicely with the relationship that nucleation rates depend on composition and particle size as defined by equations (1.2) and (1.3). The sulfate experiments did not support the same conclusion, as shown in Figures 5.4, 5.6, and 5.11a-b, the onset conditions (F=0.001) gave the smallest λ (close to 1.0). It is not clear whether this result was due to the experimental uncertainty or was a true reflection of nucleation rates in concentrated solution and small droplet sizes. More studies are needed.

The best way available to compare the results from different investigators is as shown in Figure 5.11. Since the value of λ is independent of particle sizes, chemical composition effects can be compared by using λ. It also eliminates inherent differences between experimental techniques that alter the appearance of freezing conditions on different phase diagrams (such as freezing temperature verses weight percentage or water activity). For example, particle size needs to be considered to convert from the freezing temperature versus weight percent to the temperature versus RH_w. Other confounding experimental

factors include fixing composition (weight %) versus allowing particles to equilibrate with a water vapor field, and the inherent ability or inability to assign a fraction of particles freezing at a stated freezing point.

The recent laboratory results from other investigators are also plotted in Figure 5.11. The homogeneous freezing point depressions of ammonium sulfate particles in this study (Figure 5.11a) agree with those from another diffusion chamber study [Detwiler, 1980]. Although Detwiler was not clear about the phase state of the particles used, they were in similar size range to those in this study. On the other hand, the homogeneous freezing point depressions from the flow tube experiments [Cziczo and Abbatt, 1999] indicate a much lower supercooling at high ΔT_m (higher solute concentration). High supercooling across the entire range of ΔT_m was also found in ammonium bisulfate emulsion studies with supermicron particles conducted by Koop *et al.*[1999]. Their results bound the high side of these obtained in this study. Koop *et al.* did not provide the uncertainty of their results, although their emulsion thermograms inferred freezing over a temperature range increasing with solution concentration and was as large as 4 °C(T. Koop, personal communication).

The freezing point depressions for sulfuric acid droplets in this study (Figure 5.11c) were consistent with those obtained in microscopic investigations of larger ($\sim$ 10 to 20 μm) particles by Koop *et al.*[1998]. Contradicting results were found in the flow tube experiments of Bertram *et al.*[1996], with a significantly lower λ value. The systematic difference of lower λ in the flow tube studies might originate from the definition of weight percent composition in their experiments. Another artifact is the unknown activated fraction of droplets used to define their ice formation conditions.

5.3 Implication for cirrus cloud formation

Some observations of the temperature and humidity conditions for cirrus cloud formation in the natural troposphere have been made. Heymsfield and Miloshevich [1995] found that the maximum conditions (RH_{wnuc}) for clear air around continental cirrus and orographic wave clouds could be bounded by

$$RH_{wnuc} = 1.8892 + 0.0281T + 1.3336 \times 10^{-4}T^2 \tag{5.8}$$

with T (temperature) in °C. This is the solid line called "Cirrus onset" in Figures 5.4, 5.6 and 5.9. In contrast to continental cirrus clouds, Heymsfield *et al.*[1998] found no dependence of the RH_w (~95%) on temperature for cirrus formation in air masses over the eastern Pacific Ocean.

Our laboratory results (Figures 5.4, 5.6, and 5.9) suggest that even the 0.1 % onset activation results all require colder temperatures, or higher humidities, than suggested by equation (5.9) for continental cirrus clouds. When particles are in the liquid state, the degree of neutralization by ammonium in the atmosphere may not greatly affect the relative humidity required for ice formation in cirrus clouds, since the values of λ do not distinguish from each other at high confidence level. Meanwhile, if ammoniated sulfate particles are effloresced at low humidity, such as when cirrus precipitate into dry layers, it will be difficult for them to be activated as ice crystals. Much higher humidities may then be required for ice formation. This is a possible interpretation for the occasional circumstance when high humidity is required for cirrus cloud formation, as in Heymsfield *et al.*[1998]. Furthermore, the sizes of particle are very important for their ice formation behaviors. Small particles in the range of 0.05 μm require above 95% RH_w to initiate ice phase, while slightly larger particles of 0.2 μm lower the required humidity by 10% RH_w. This factor could explain the onset conditions observed by Heymsfield *et al.*[1998] in some oceanic cirrus, if the ambient aerosol particles were quite small. Small particle sizes can explain the high onset conditions (¿ 95%) observed in some oceanic cirrus. Thus, differences in particle sizes, composition and phase state must exist in order to explain regional differences in cirrus cloud formation conditions via nucleation of pure sulfates. Unless there remain unidentified solutes or solute mixtures that more readily form ice at lower humidities, heterogeneous nucleation is the likely explanation for the full range of observed conditions of cirrus formation [*e.g.*, DeMott *et al.*, 1997].

5.4 Summary

The homogeneous formation of ice in ammonium sulfate, ammonium bisulfate, and sulfuric acid aerosol particles has been studied with a continuous flow thermal diffusion chamber. Several conclusions can be drawn from these results:

- The phase states of salt particles are very important in these experiments, since these determine the ice formation mechanism(s). The relative humidities required for ice formation between dry and liquid aerosol particles could be different up to 10% respect to water at upper tropospheric conditions. Solution particles freeze at lower RH_w, and need to be diluted before homogeneous nucleation and freezing starts. The ice formation mechanism for dry ammonium sulfate is not well understood, nor is it clear why partially crystallized ammonium bisulfate particles activated ice formation in a different manner than liquid drops. Direct deposition might be taking place inside the CFD.

- For liquid ammonium sulfate, ammonium bisulfate, and sulfuric acid drops, the depressions of homogeneous freezing point greatly exceed their equivalent melting point depressions. The mean values of the melting point depression coefficient are 1.75 ± 0.35, 1.38 ± 0.34, 1.98 ± 0.27 for ammonium sulfate, ammonium bisulfate, and sulfuric acid, respectively. Relatively high humidities are required to form cirrus clouds, especially at lower temperatures.

- Between these three substances, the differences in chemical compositions is unlikely to be important to form cirrus clouds. Only liquid sulfate particles with accumulation mode size can satisfy the observations of continental cirrus formation conditions [Heymsfield and Miloshevich, 1995]. Small sulfuric acid particles cannot explain the onset conditions of continental cirrus.

- The size effects is likely to explain the different ice formation behaviors of liquid 0.2 μm ammoniated sulfates and 0.05 μm sulfuric acid particles. More experiments are needed to understand the chemical composition effects.

- Based on previous observations [Heymsfield *et al.*, 1998], the RH_w above 95% required for the formation of some oceanic cirrus clouds could be explained in two ways: either homogeneous freezing of small sulfate or sulfuric acid particles, or ice formation of anhydrous sulfate particles.

- With the existed knowledge, it seems like that heterogeneous nucleation is the only viable explanation of the existing observations of the full range of cirrus cloud onset conditions, since sulfate and sulfuric acid require higher humidities than those available in the natural atmosphere.

Table 5.1: The saturation ratios (with respect to water) for different activated fractions in ice formation by (a) ammonium sulfate, (b) ammonium bisulfate, and (c) sulfuric acid. Underlined dates are experiments with pre-conditioner.

Temp(°C)	Solution Drops			Dry Crystals				Date
	0.1%	1%	10%	0.1%	1%	10%	0.1% SSi	
-40.0	1.040			1.030			52.9	02/05/99
-40.3	1.026		1.060					12/31/97
-42.2					1.050			01/15/98
-44.7				1.020			50.5	01/12/98
-45.0				1.000		1.020	54.7	11/23/98
-45.0	0.930	0.985		0.995			54.0	02/04/99
-45.5	0.965							12/31/97
-45.5	0.945							02/09/98
-45.6	0.945			0.950			46.7	01/25/99
-47.2				0.965			51.2	01/20/98
-47.5				0.955			49.8	01/07/98
-50.0				0.960			55.2	01/20/98
-50.0		0.885						11/19/98
-50.0		0.875	0.950					11/19/98
-50.0	0.860	0.910	0.975					11/25/98
-50.0	0.870	0.950	0.980					02/08/99
-50.2				0.940			53.0	01/05/98
-51.2				0.955			56.4	01/13/98
-51.3				0.940			55.2	01/14/98
-53.2				0.945			56.1	01/13/98
-55.0	0.865	0.975		0.970			66.0	02/03/99
-55.2				0.940			60.4	01/15/98
-56.0	0.850							01/21/98
-60.0	0.845	0.930						01/21/98
-60.0	0.840	0.930						02/03/98
-60.0	0.830				0.960			02/02/99
-60.3	0.845	0.903	0.940					02/06/98
-60.5	0.825	0.928	1.055					01/06/98
-60.8				0.940	0.960	1.025	67.0	02/04/98
-60.0	0.800	0.855	0.990					02/16/99

Temp(°C)	Solution Drops			Low Humidity			Date
	~ 0.1%	~ 1%	~ 10%	~ 0.1%	~ 1%	~ 10%	
-20.0	1.020						05/04/98
-30.0		1.060					04/09/98
-31.0			1.080				11/11/97
-40.0		1.020	1.055				11/07/97
-40.0	1.040						12/30/97
-40.0	1.030		1.055	1.030		1.040	02/19/99
-41.8	1.070						12/30/97
-42.5	1.020						12/12/97
-42.5	1.030	1.046					12/19/97
-43.0		0.915					11/19/97
-43.5	0.960						12/03/97
-45.0			0.900				11/06/97
-45.0	0.890	0.914					11/24/97
-45.0	0.895						11/24/97
-45.0				1.020			02/23/99
-45.0	0.940	1.010		1.005			02/24/99
-45.0	0.960						03/01/99
-45.9					1.035		03/26/98
-47.5	0.857						11/24/97
-48.0	0.905						12/03/97
-50.0	0.895	1.025	1.045				03/23/98
-50.0				1.010			02/22/99
-50.0	0.925	0.950	0.985				02/24/99
-50.0	0.950	0.975					03/01/99
-51.0	0.835	0.845	0.890				11/18/97
-52.0	0.820	0.895	0.923				11/24/97
-52.5	0.895						11/26/97
-54.5				0.955	0.985	1.020	03/20/98
-55.0		0.950					11/25/97
-55.0	0.835						11/26/97
-55.0				0.980			03/10/98
-55.0	0.850	0.895		0.975			02/18/99
-55.8	0.840						12/04/97
-57.5				0.960			12/15/97
-57.5				0.970			12/17/97
-60.0	0.843						12/10/97
-60.0	0.840	0.890		0.970			02/17/99
-60.3	0.860						12/15/97
-60.3	0.830						03/25/98

Temp(°C)	Sulfuric Acid Drops			Date
	0.1%	1%	10%	
0.016 μm				
-35.0		1.055	1.165	09/28/98
-45.0	1.015	1.030		09/22/98
-50.0	0.990	1.015	1.030	09/22/98
-55.0	0.980			09/24/98
-60.0	0.975	1.005		09/24/98
0.05 μm				
-44.9	0.990			05/26/99
-45.0	0.984	1.004		10/29/98
-45.0	0.995	1.015		11/02/98
-50.0	0.940	0.960	0.980	10/29/98
-50.0	0.940	0.955	0.975	11/12/98
-50.0	0.935	0.950	0.973	11/12/98
-55.0	0.870	0.895	0.990	10/28/98
-55.2	0.901			05/25/99
-56.0	0.890	0.915		11/10/98
-59.9	0.883			05/25/99
-60.0	0.855	0.890	0.940	10/27/98
-60.0	0.885	0.925	0.940	11/11/98
-60.0	0.950	0.970		11/13/98

Table 5.2: Summary statistics–freezing of wet ammonium sulfate (0.1% activated fraction).

Temp (°C)	RH_w (%)	Mean RH_w (%)	S.D. (%)	Pooled S.D.(%)	80% t	95% t	CI at 80%(%)	CL at 95%(%)	CL at 90%(%)
-40.00	104.0	103.3	1.0	1.4	1.89	4.3	±1.9	±4.3	±2.9
-40.30	102.6								
-45.00	93.0	94.6	1.4		1.53	2.78	±1.2	±2.8	±1.7
-45.50	96.5								
-45.50	94.5								
-45.60	94.5								
-50.00	86.0	86.5	0.7		1.89	4.30	±1.9	±4.3	±2.9
-50.00	87.0								
-55.00	86.5	85.8	1.1		1.89	4.30	±1.9	±4.3	±2.9
-56.00	85.0								
-60.00	84.5	83.1	1.7		1.44	2.45	±0.8	±1.4	±1.1
-60.00	84.0								
-60.00	83.0								
-60.30	84.5								
-60.50	82.5								
-60.00	80.0								

Table 5.3: Summary statistics–freezing of dry ammonium sulfate particle (0.1% activated fraction).

Temperature (°C)	RH_w (%)	Mean RH_w (%)	S.D. (%)	Pooled S.D.(%)	80% t	95% t	CL at 80%(%)	CL at 95%(%)
-40.0	103.0			2.2				
-44.7	102.0	99.1	2.9		1.53	2.78	±1.7	±3.1
-45.0	100.0							
-45.0	99.5							
-45.6	95.0							
-47.2	96.5	96.0	0.7		1.89	4.30	±2.9	±6.7
-47.5	95.5							
-50.0	96.0	95.0	1.4		1.89	4.30	±2.9	±6.7
-50.2	94.0							
-51.2	95.5	94.8	1.1		1.89	4.30	±2.9	±6.7
-51.3	94.0							
-53.2	94.5							
-55.0	97.0	95.5	2.1		1.89	4.30	±2.9	±6.7
-55.2	94.0							
-60.8	94.0							

Table 5.4: Summary statistics–freezing of wet ammonium bisulfate particles (0.1% activated fraction).

Temperature (°C)	RH_w (%)	Mean RH_w (%)	S.D. (%)	Pooled S.D.(%)	80% t	95% t	CL at 80%(%)	CL at 95%(%)
-40.0	103.0	103.5	0.7	2.8	1.89	4.30	±3.7	±8.5
-40.0	104.0							
-41.8	107.0							
-42.5	102.0	104.0	2.6		1.64	3.18	±2.6	±5.1
-42.5	103.0							
-43.5	96.0							
-45.0	94.0							
-45.0	96.0	92.9	3.4		1.48	2.57	±1.8	±3.2
-45.0	89.0							
-45.0	89.5							
-47.5	85.7	88.1	3.4		1.89	4.30	±3.7	±8.5
-48.0	90.5							
-50.0	89.5							
-50.0	92.5	92.3	2.7		1.64	3.18	±2.6	±5.1
-50.0	95.0							
-51.0	83.5							
-52.0	82.0	85.0	4.0		1.64	3.18	±2.6	±5.1
-52.5	89.5							
-55.0	85.0							
-55.0	83.5	84.2	0.8		1.64	3.18	±2.6	±5.1
-55.8	84.0							
-60.0	84.3	84.3	1.2		1.53	2.78	±2.1	±3.9
-60.3	86.0							
-60.3	83.0							
-60.0	84.0							

Table 5.5: Summary statistics–freezing of "dry" ammonium bisulfate particles (0.1% activated fraction).

Temperature (°C)	RH_w (%)	Mean RH_w (%)	S.D. (%)	Pooled S.D.(%)	80% t	95% t	CL at 80%(%)	CL at 95%(%)
-40.0	103.0			1.1				
-45.0	100.5	101.2	1.1		1.89	4.30	±1.5	±3.3
-45.0	102.0							
-50.0	101.0							
-54.5	95.5	97.0	1.3		1.64	3.18	±1.0	±2.0
-55.0	98.0							
-55.0	97.5							
-57.5	96.0	96.5	0.7		1.89	4.30	±1.5	±3.3
-57.5	97.0							
-60.0	97.0							

Table 5.6: Summary statistics–freezing of 0.05 μm sulfuric acid particles (0.1% activated fraction).

Temp (°C)	RH_w (%)	Mean RH_w (%)	S.D. (%)	Pooled S.D.(%)	80% t	95% t	CL at 80%(%)	CL at 95%(%)	CL at 90%(%)
-44.9	99.0	99.0	0.5	1.2	1.64	3.18	±1.1	±2.2	±1.5
-45.0	98.4								
-45.0	99.5								
-50.0	94.0	93.8	0.3						
-50.0	94.0								
-50.0	93.5								
-55.0	87.0	88.7	1.6						
-55.2	90.1								
-56.0	89.0								
-59.9	88.3	87.4	1.7						
-60.0	85.5								
-60.0	88.5								

Table 5.7: Summary–hypothesis testing at different confidence levels (0.1% activation). The underlined cells pass the tests.

T (°C)	RH_{onset} for sulfate	RH_{onset} for sulfuric acid	Difference between means	t at 90% CL	t at 95% CL	t at 99% CL	Computed difference at 90% CL	Computed difference at 95% CL	Computed difference at 99% CL
-45	94.6	99	4.4	2.02	2.57	4.03	2.0	2.6	<u>4.0</u>
-50	86.5	93.8	7.3	2.35	3.18	5.84	2.8	3.8	<u>6.9</u>
-55	85.8	88.7	2.9	2.35	3.18	5.84	<u>2.8</u>	3.8	6.9
-60	83.1	87.4	4.3	1.90	2.36	3.50	1.7	2.2	<u>3.2</u>

Table 5.8: Summary of 1% activated results for ammonium sulfate and sulfuric acid and their pooled standard deviation. (a) 1% activated, ammonium sulfate experiments, (b) 1% activation, sulfuric acid experiments.

Temp	Solution Drops			Dry Crystals			Pooled
(°C)	1%	Mean	S.D.	1%	Mean	S.D	S.D.
-42.2				1.050			0.032
-45.0	0.985						
-50.0	0.950	0.905	0.033				
-50.0	0.885						
-50.0	0.910						
-50.0				1.010			
-60.0	0.930	0.909	0.032				
-60.0	0.930			0.960			
-60.3	0.903						
-60.5	0.928						
-60.8				0.960			
-60.0	0.855						

Temp(°C)	RH_w	Mean	S.D.	Pooled S.D.
-45.0	1.004	1.010	0.008	0.01
-45.0	1.015			
-50.0	0.960	0.955	0.005	
-50.0	0.955			
-50.0	0.950			
-55.0	0.895	0.905	0.014	
-56.0	0.915			
-60.0	0.890	0.908	0.025	
-60.0	0.925			

Table 5.9: The hypothesis test on the confidence level to distinguish the differences between the RH_w required for 0.1% and 1% activation. AS: ammonium sulfate; SA: sulfuric acid; the underlined cells are smaller than the RH_w difference, therefore pass the test.

T (°C)		RH_{onset} for 0.1%	RH_{onset} for 1%	Difference between means	t at 80% CL	t at 90% CL	t at 95% CL	Computed difference at 80% CL	Computed difference at 90% CL	Computed difference at 95% CL
AS	-50	86.5	90.5	4.0	1.53	2.13	2.78	3.0	4.2	5.5
	-60	83.1	90.9	7.8	1.38	1.83	2.26	1.9	2.5	3.1
SA	-45	99.0	101.0	2.0	1.64	2.35	3.18	1.9	2.8	3.8
	-50	93.8	95.5	1.7	1.53	2.13	2.78	1.5	2.3	2.9
	-55	88.7	90.5	1.8	1.64	2.35	3.18	1.9	2.8	3.8
	-60	87.4	90.8	3.4	1.64	2.35	3.18	1.9	2.8	3.8

Table 5.10: The hypothesis test on the confidence level to distinguish the differences between the RH_w required for 1% activation results for ammonium sulfate and sulfuric acid. The underlined cells pass the test.

T (°C)	RH_{onset} for sulfate	RH_{onset} for sulfuric acid	Difference between means	t at 80% CL	t at 90% CL	t at 95% CL	Computed difference at 80% CL	Computed difference at 90% CL	Computed difference at 95% CL
-50	90.5	95.5	5.0	1.42	1.90	2.36	2.7	3.6	<u>4.4</u>
-60	90.9	90.8	0.1	1.44	1.94	2.45	3.1	4.2	5.3

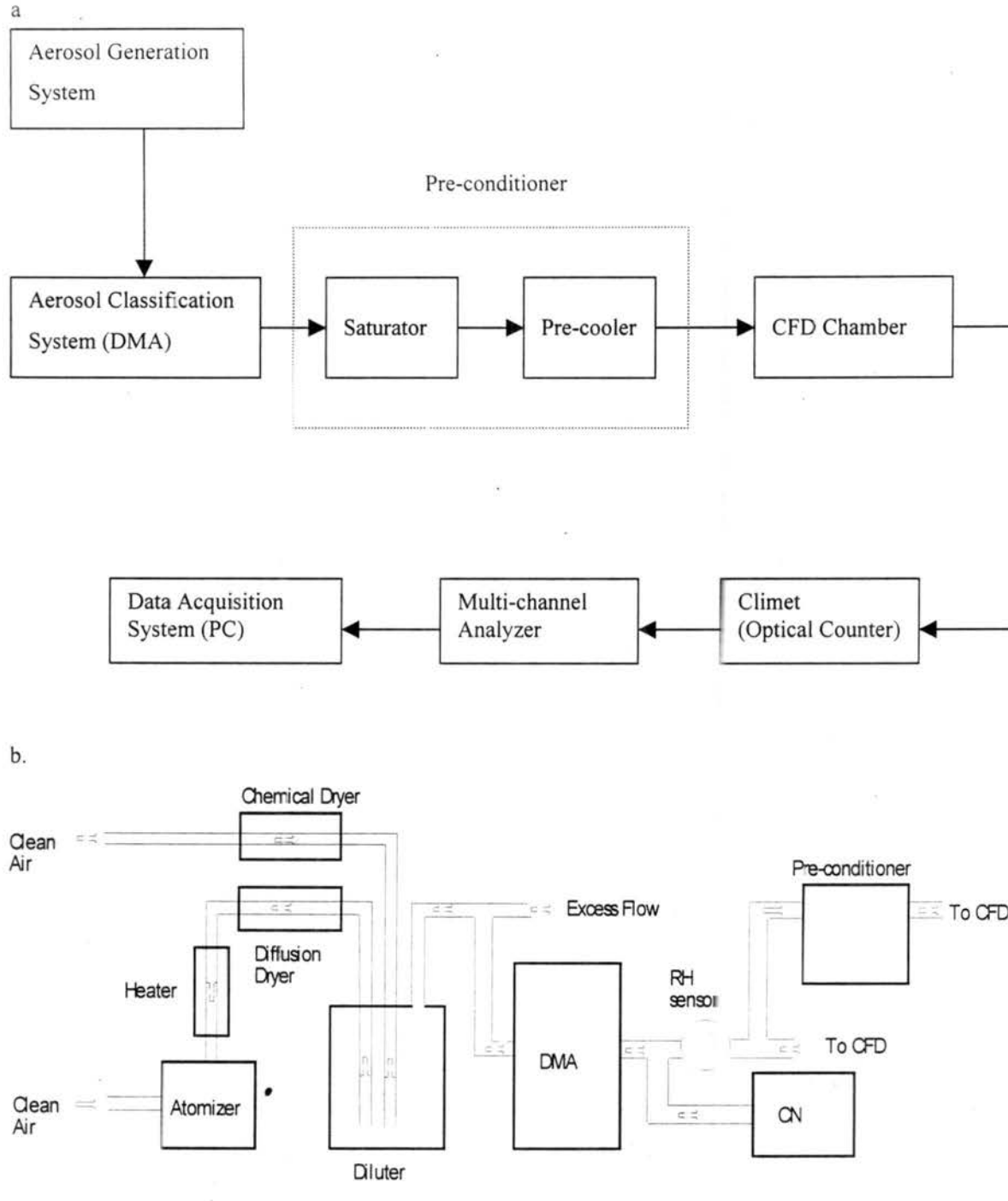

Figure 5.1: Schematic of the experimental configuration. Aerosol particles are generated as wet and poly-dispersed, then dried and selected by the DMA. Before they enter the CFD, the pre-conditioner presets their phase state. (a) Flow chart; (b) System configuration.

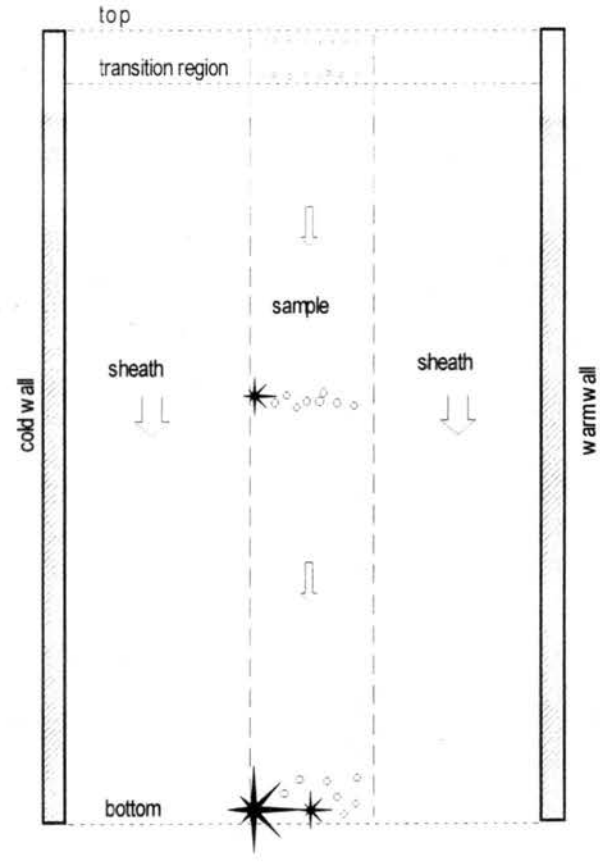

Figure 5.2: Evolution of solution drops and ice crystals inside the CFD. Some ice crystals are frozen later than others, therefore are small at the exit.

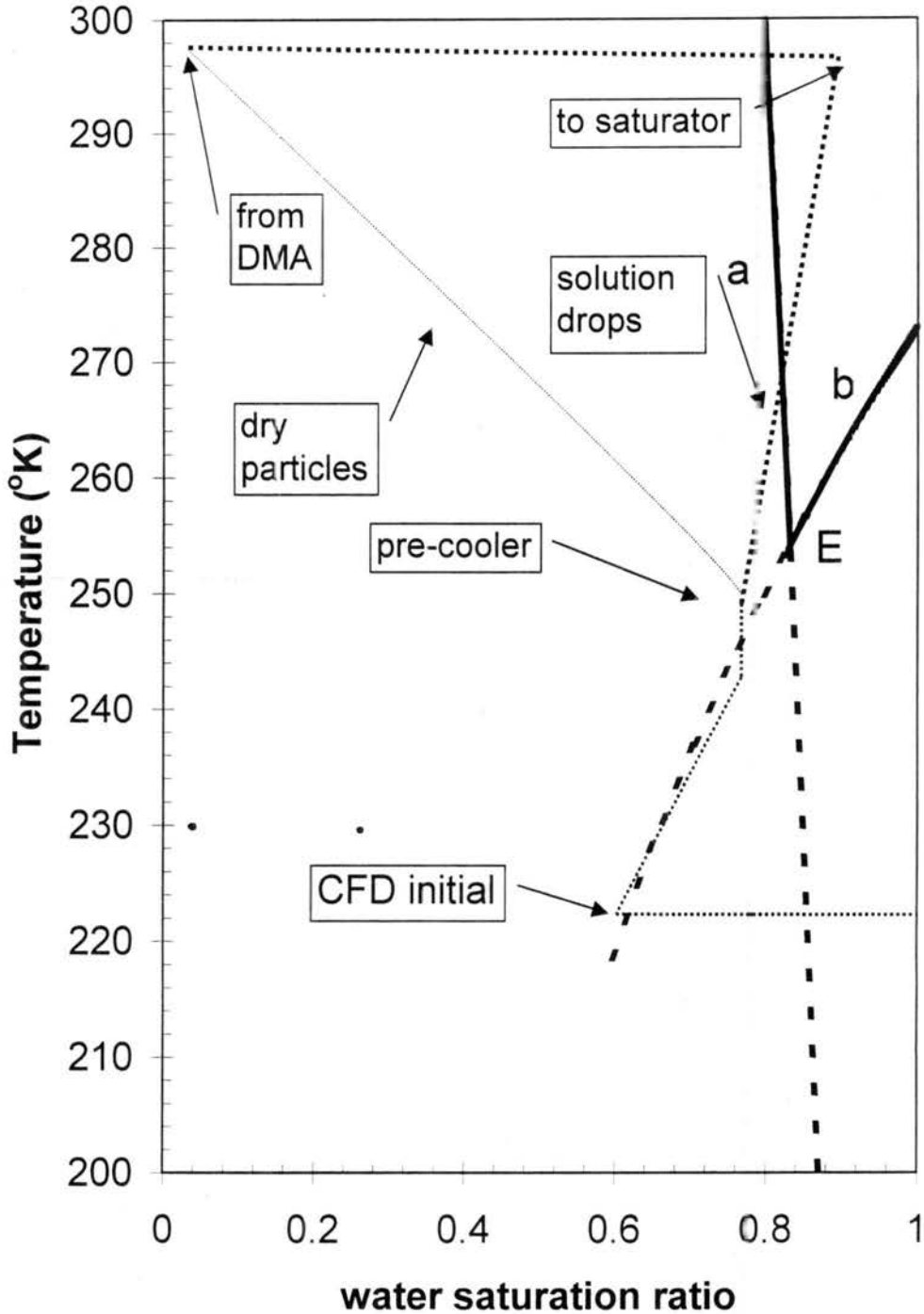

Figure 5.3: The relative humidity and temperature trajectories of aerosol particles from the generation system to the CFD. The thick dotted line represents the experimental trajectory followed by solution drops for CFD sampling at -50°C. Similarly, the thin dotted line is for dry crystals.

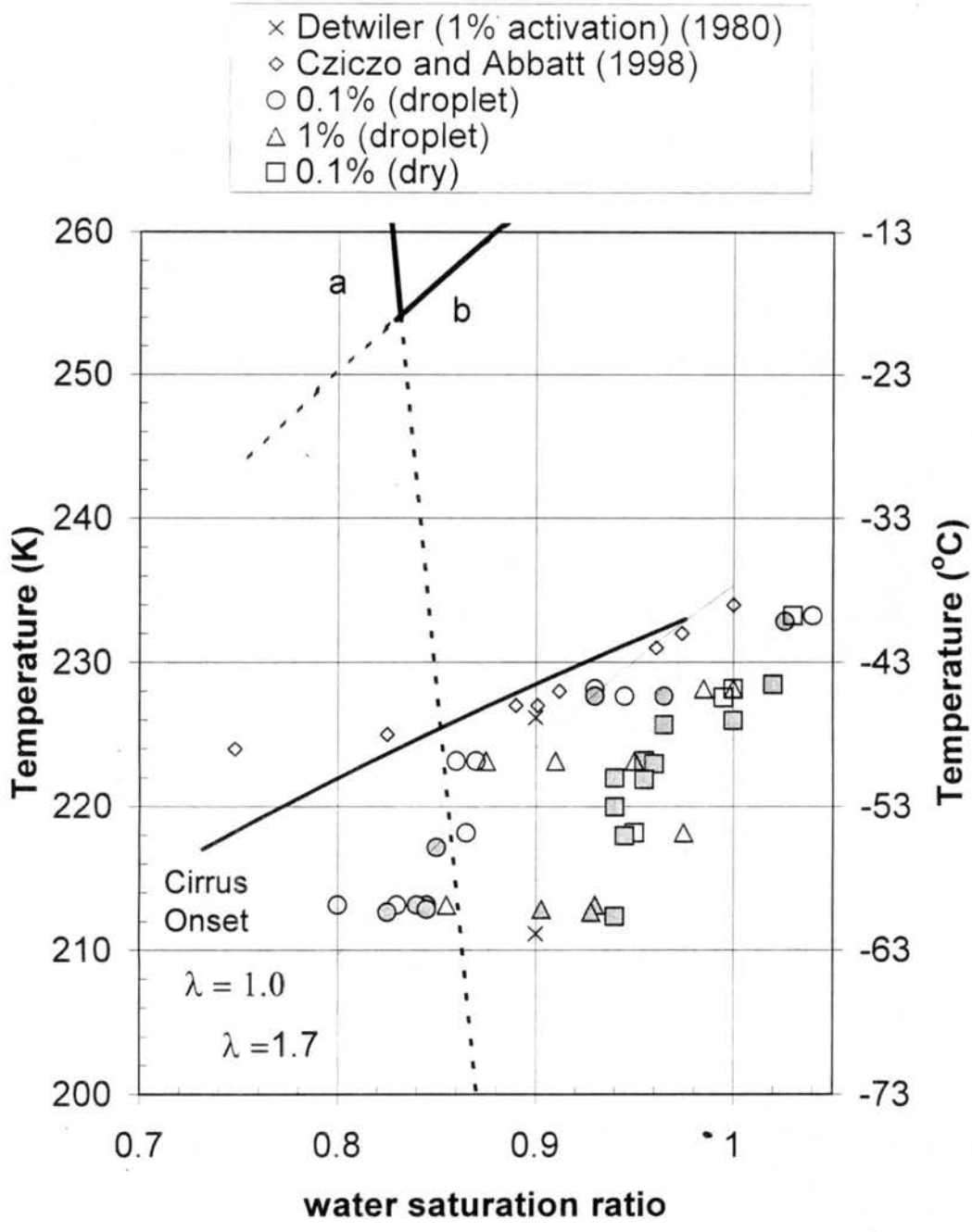

Figure 5.4: Phase diagram of $(NH_4)_2SO_4$-H_2O system for bulk solution and super-cooling curves. Bulk solution (a) and super-cooling (b) curves are given as thick solid curves, extrapolated below the eutectic temperature as thick dashed curves. Circles (F = 0.001, wet), squares (F = 0.001, dry), and triangles (F = 0.01, wet) mark data for initial 0.2 μm diameter particles in this work; crosses (Detwiler, 1980; F = 0.01; average dry diameter = 0.2 μm) and diamonds (Cziczo and Abbatt, 1998; F undefined; average wet diameter = 0.35 μm) are from other studies. A line representing conditions for continental cirrus formation (Heymsfield and Milosevich, 1995) is also identified. Thin and dotted lines of λ = 1 and 1.7 are based on equations (2) and (3), with F = 0.01 and haze particles at diameters in equilibrium with the vapor (diameter = 0.2 μm at RH_w = 2%). Filled marks represent the experiments without the pre-conditioner, while open marks are pre-conditioned results.

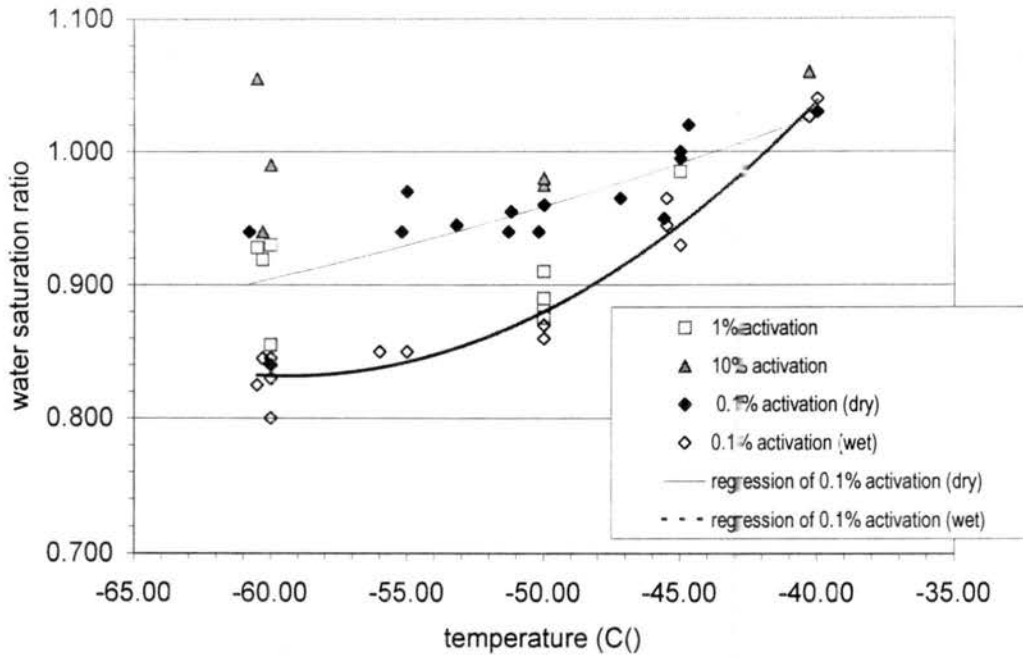

Figure 5.5: Ice formation temperatures and RHs of $(NH_4)_2SO_4$ particles with diameters of 0.2 μm. Black line represents the trend line of 0.1% of input solution drops activated as ice crystals, and dotted line is the trend line of 0.1% activated fraction with dry crystals.

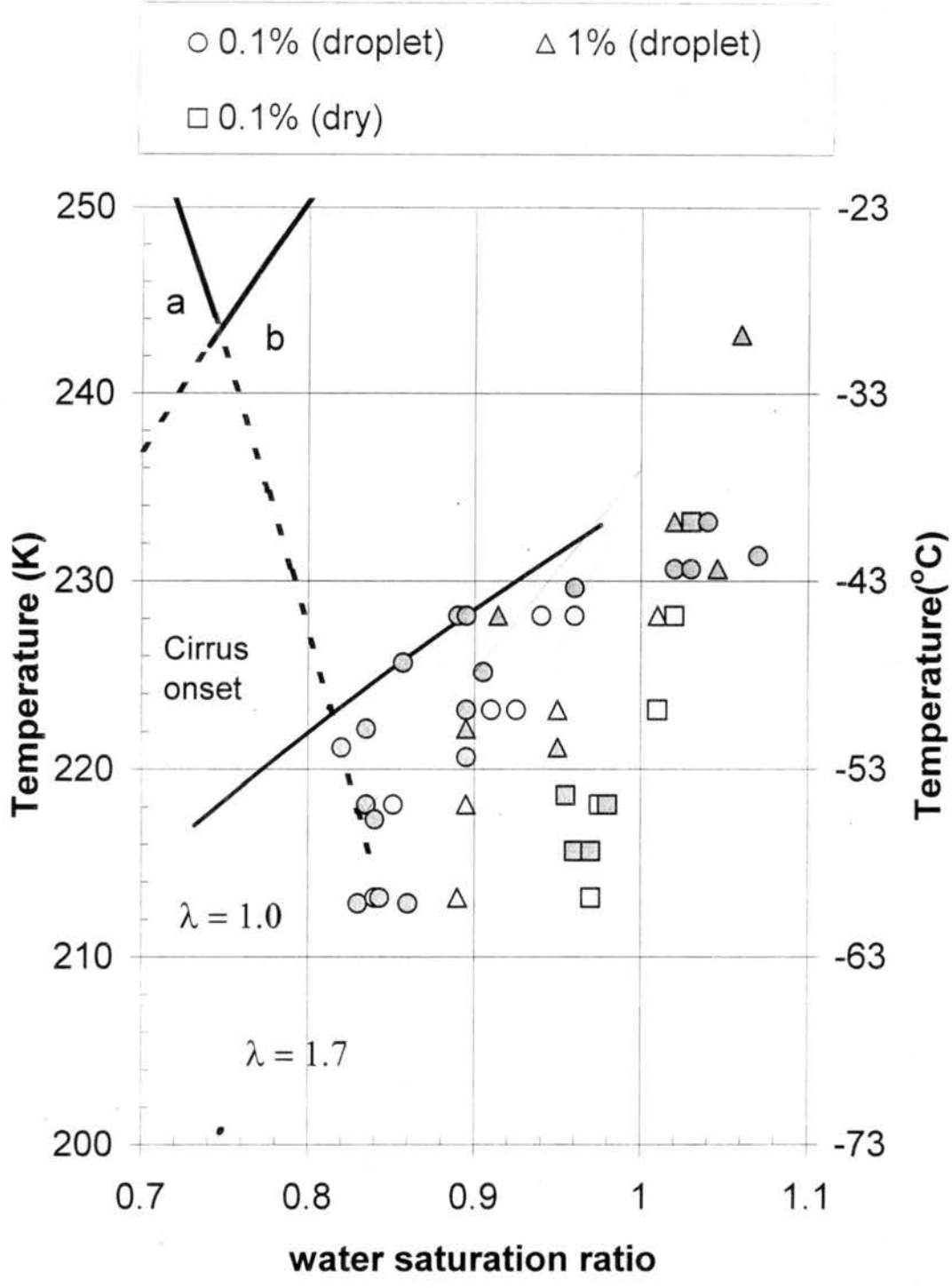

Figure 5.6. Phase diagram of NH_4HSO_4 - H_2O system for bulk solution and super-cooling curves. Bulk solution (a), super-cooling (b), and "cirrus onset" curves are indicated as in Figure 5. Circles (F = 0.001, wet), squares (F = 0.001, dry), and triangles (F = 0.01, wet) mark data for initial 0.2 μm diameter particles in this work. Thin and dotted lines of $\lambda = 1$ and 1.7 are based on equations (2) and (3), with F = 0.01 and haze particles in equilibrium with vapor (diameter = 0.2 μm at $RH_w = 2\%$). Filled and opened marks have the same meaning as in Figure 5.4.

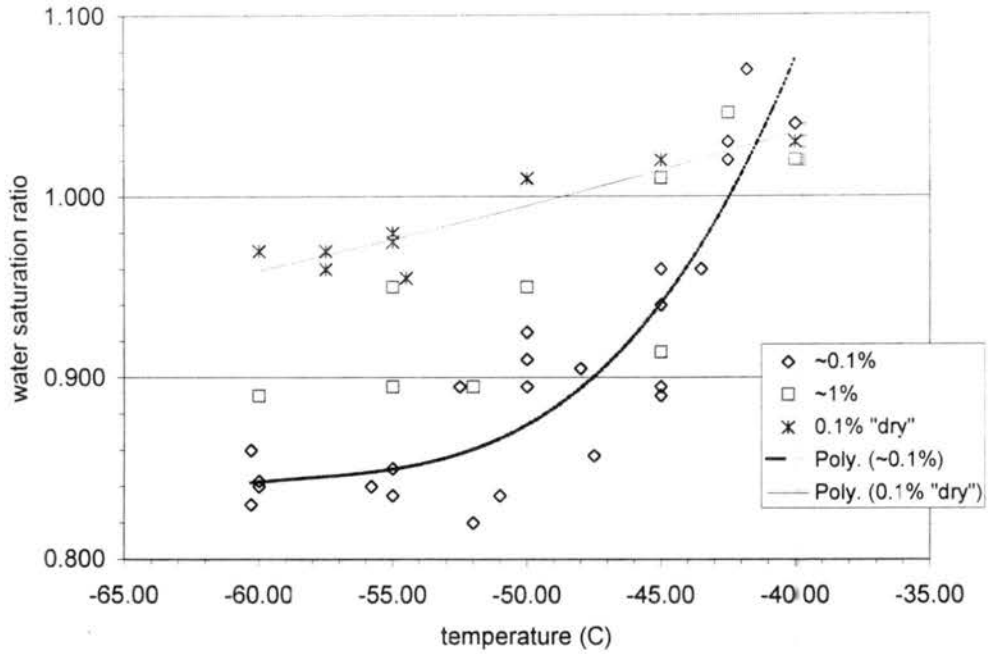

Figure 5.7. Ice formation temperatures and RHs of NH_4HSO_4 particles with diameters of 0.2 μm. Black line represents the trend line of 1% of input aerosol particles activated as ice crystals, and dotted line is the trend line of 0.1% activated fraction.

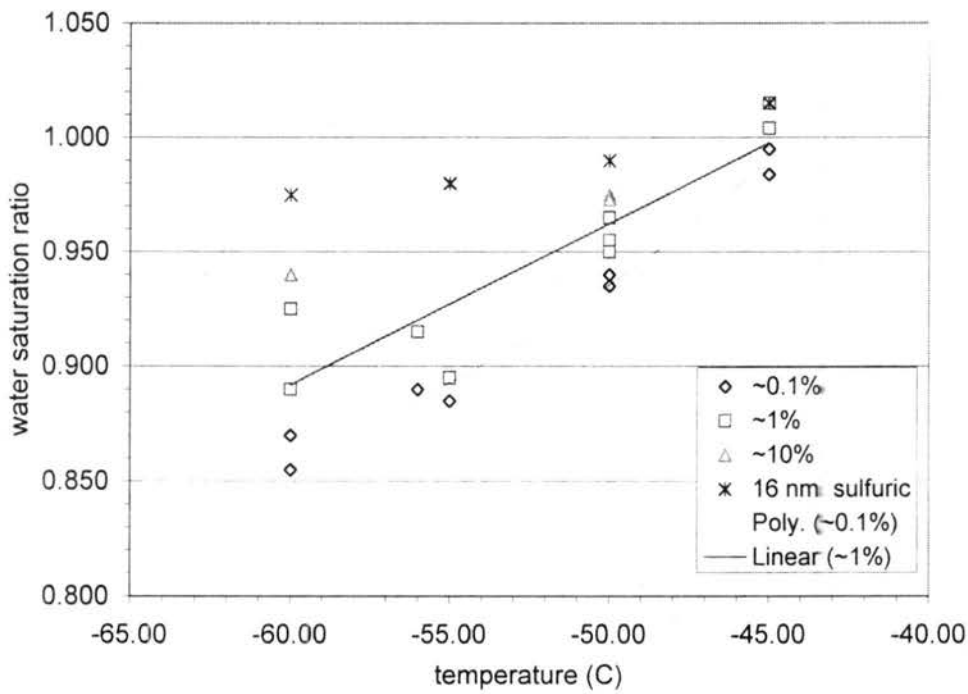

Figure 5.8. Ice formation temperatures and RHs of 0.05 μm H_2SO_4 particles. The black line represents 1% activated fraction of sulfuric acid as ice crystals. Diamonds mark 0.1% activated fraction, empty squares 1%, solid triangles 10%. The solid line is the regression line for 1% activated fraction.

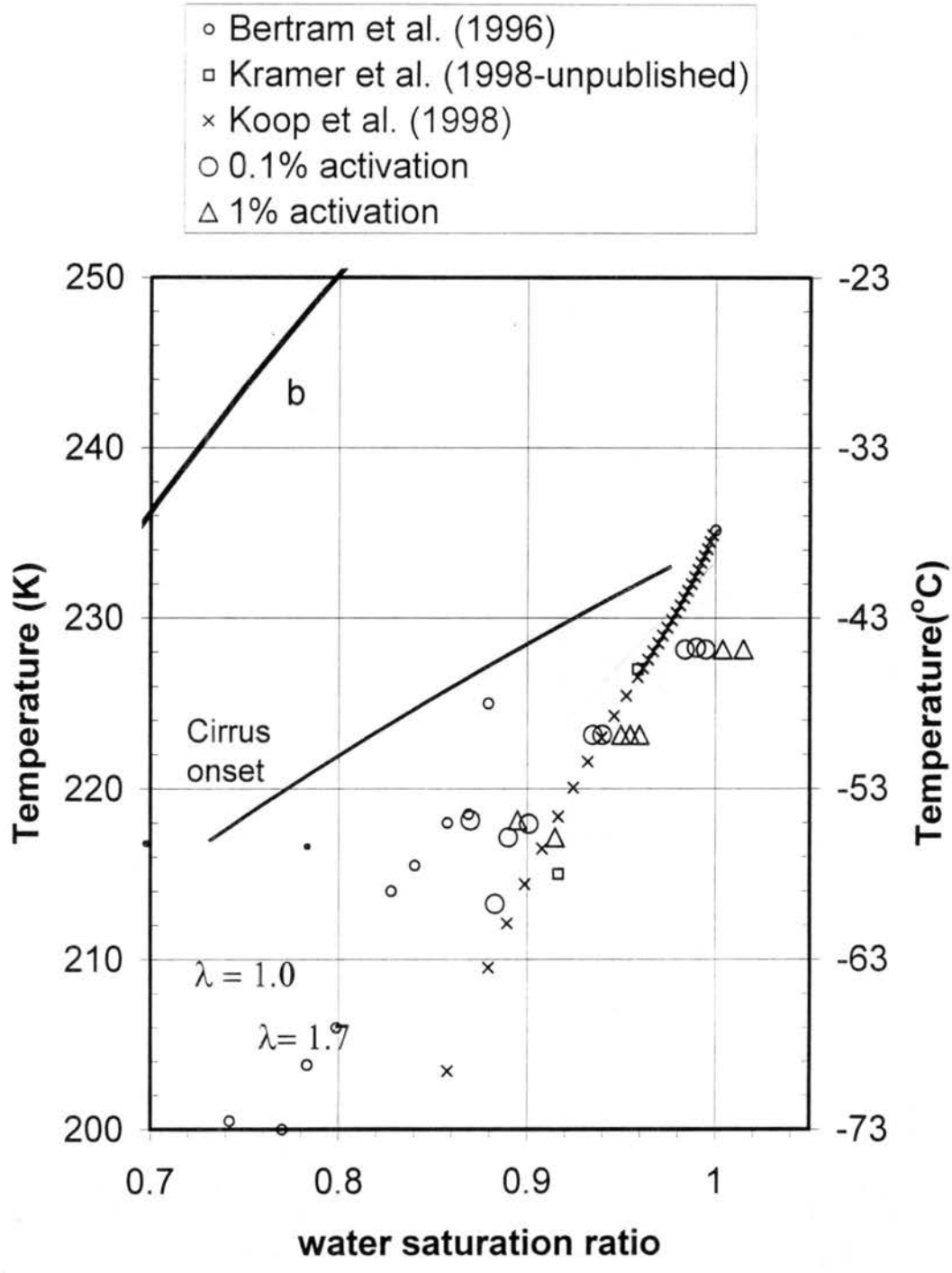

Figure 5.9: Phase diagram of H_2SO_4 - H_2O system for bulk solution and super-cooling curves. Super-cooling (b) and "cirrus onset" curves are indicated as in Figure 5. Circles (F = 0.001) and triangles (F = 0.01) mark data from this work. Comparisons between results from different groups are also superimposed. Empty small circles mark data from Bertram et al. (1996; F undefined; average wet diameter = 0.4 μm), crosses are based on a fit to data given by Koop et al. (1998; F = 0.5; average wet diameter = 10 μm), small squares are from Krämer (1998; F ≈ 0.5; average wet diameter = 50 μm). The lines of constant λ = 1 and 1.7 are based on equations (2) and (3), with F = 0.01 and haze particles at diameters in equilibrium with the vapor (diameter =0.05 μm at RH_w = 2%).

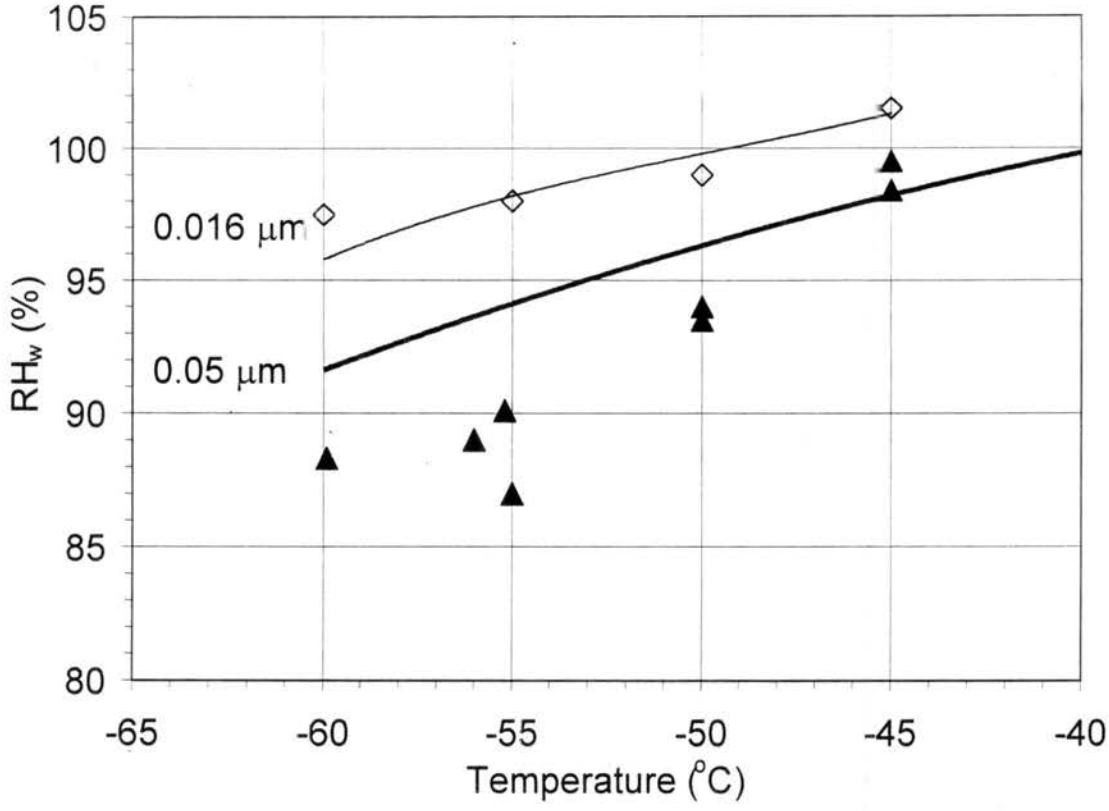

Figure 5.10. Particle size dependence of the RH_w required for freezing 0.1% of sulfuric acid droplets during the CFD residence time. The particles used were 0.05 μm "monodisperse" (filled triangles) and a narrow distribution of polydisperse particles with mean diameter 0.016 μm (open diamonds). The thick and thin curves are calculated for F = 0.001 using (1.2) and (1.3), and assuming $\lambda = 1.98$. See the text for additional details.

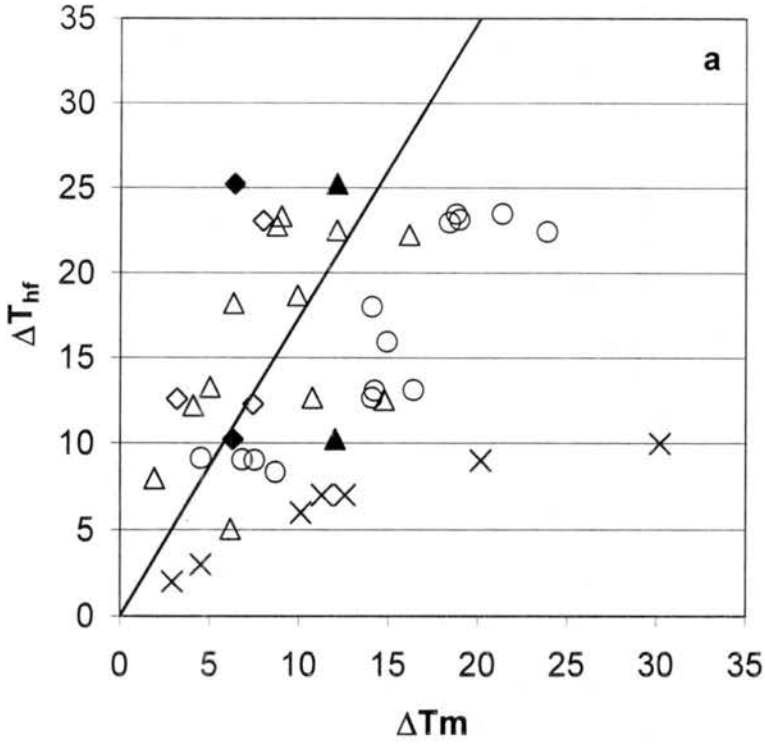
a
35
30
25
20
15
10
5
0
0
5
10
15
20
25
30
35
ΔThf
ΔTm

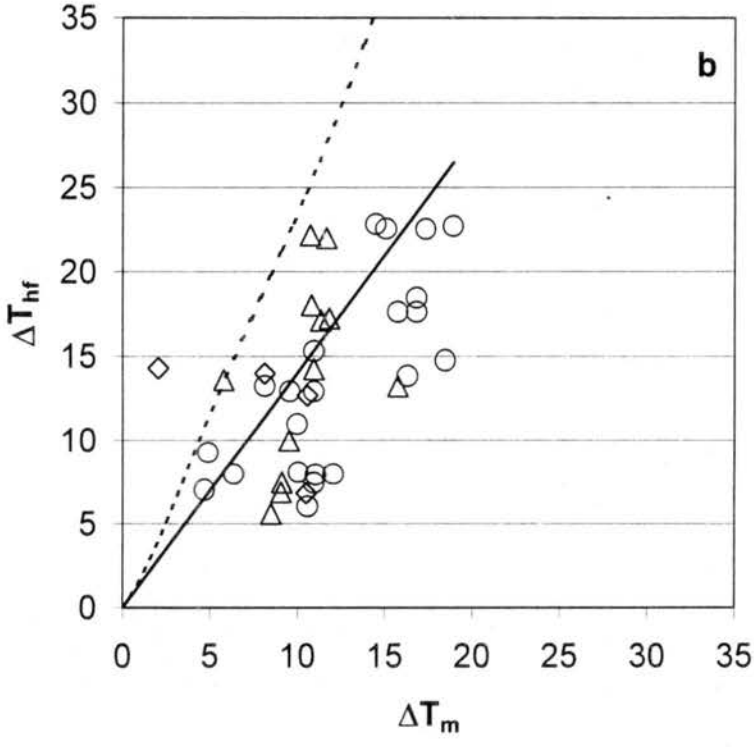
b
35
30
25
20
15
10
5
0
0
5
10
15
20
25
30
35
ΔThf
ΔTm

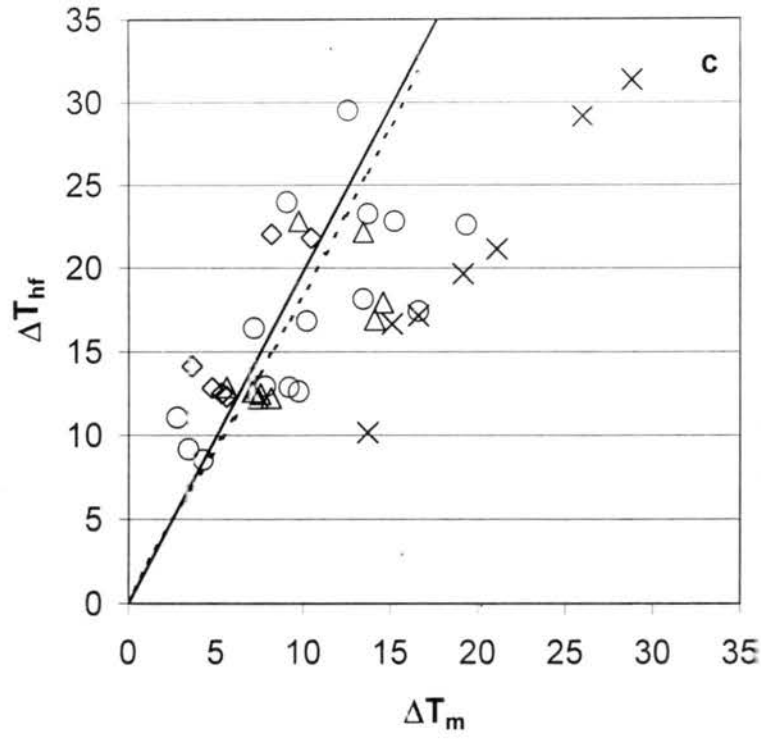

Figure 5.11. Plots of the depression of the homogeneous freezing temperature (ΔT_{hf}) of solution droplets compared to pure water drops of the same size versus the melting point depression (ΔT_m) associated with the solution droplet composition. Panels a to c are for ammonium sulfate, ammonium bisulfate and sulfuric acid, respectively. The ΔT_{hf} values are determined (see text) for conditions of 0.1% (F = 0.001, circles), 0.1% (F = 0.01, triangles) and 10% (F = 0.1, diamonds) particles freezing. Filled data points in panel a are for the same fractions activating, but are based on static diffusion chamber data from Detwiler (1980). Data from flow tube studies (F is undefined) are indicated by X symbols in a (Cziczo and Abbatt, 1999) and c (Bertram et al., 1996). Dashed lines in b and c are based on fits to fixed droplet freezing data ($F \approx 0.5$) from Koop et al. (1999) and Koop et al. (1998), respectively. The solid line in each panel is for the average λ determined from the data in the current study.

Chapter 6

IMPACT OF AIRCRAFT EXHAUST ON CIRRUS CLOUD FORMATION – ICE FORMATION IN SOOT PARTICLES WITH DIFFERENT COVERAGES OF SULFURIC ACID

In the upper troposphere and lower stratosphere, carbonaceous particles are found to be an important category of particulate matter (see discussion in Chapters 1, 4 and 5). Carbonaceous particles can be further classified into two sub-categories, soot (black carbon) and organic. Soot particles are mainly generated by anthropogenic sources, like incomplete combustion, while organic particles can have both natural and anthropogenic sources. As high-altitude jet aircraft traffic has increased, soot particles have become a larger concern for global climate change. This concern stems from the direct radiative effect of soot particles due to their low albedo, and the indirect role of soot particles in atmospheric chemistry, clouds, and climate due to their serving as sites for cloud particle formation and chemical reactions.

This chapter describes ice formation tests on various types of soot particles, mainly at temperatures below -40°C. The carbon particles used include pure soot particles, soot particles coated with an approximate monolayer of sulfuric acid, soot particles coated with more than a monolayer of sulfuric acid, and monodisperse soot particles produced by combustion of aircraft jet fuel. Results of experiments with the last type of particle are used to compare with the field measurements from SUCCESS.

6.1 Experimental section

The primary instrument for the experiments described in this chapter was the continuous flow thermal diffusion chamber (CFD III), as described in Chapter 2. The experimental

configuration was similar to the one used in Chapter 5, except that a different aerosol generation system was used. The principle of the soot generation system is described in Chapter 2. The amorphous carbon particles tested in these experiments are manufactured by Degussa Corporation (Frankfurt, Germany), primarily for use as pigments and in printing. The material used was so called "lamp black", specified to have an average size of 0.095 μm in diameter, volatile content of 1.1% by weight at 950°C, and bulk density of 1.9 g cm^{-3}. Jet fuel soot particles were generated by combustion of jet fuel with a camp stove in a large particle free storage vessel (grain bin).

The Degussa carbon particles were broken up by the vibration of the surface of an audio speaker, which was operated at 650 Hz with ~0.8 V of amplitude. High purity nitrogen (4.8 degree) was used as the carrier gas. The schematic of the soot generator is shown in Chapter 2 (Figure 2.5). The size distribution of the output, as measured by the DMA, was a lognormal distribution with a mode at ~0.24 μm in diameter and geometric standard deviation $\sigma = 1.6$. Due to the limitation of the low-concentration aerosol output from the speaker generator, all the soot particles were sampled by the CFD without size classification by DMA. Therefore in this study, the Degussa soot particles were polydispersed. To coat these particles, they were passed through the sulfuric acid generator (as described in Chapter 2). The heating temperature of sulfuric acid determined the coverage of sulfuric acid on the particles if all others parameters were constant. A CCN counter (Mee Industries) was used to help quantify the amount of sulfuric acid coating as described by DeMott *et al.* [1999]. It is a static thermal gradient diffusion chamber (TGDC), using similar principles as the CFD to create a super-saturation profile between wetted plates in a horizontal configuration. A measurement of the critical supersaturation and simplified Köhler theory were the basis for determining the weight percent H_2SO_4 composition of the mean-sized soot particle and thereby estimating surface coverage.

Changes in room temperature during tests could change the super-saturation of sulfuric acid in the quenching region. Therefore slightly different amounts of sulfuric acid might condense onto the soot particles for the same heater condition at different times. The low temperatures in upper tropospheric conditions make it possible that homogeneous

mechanisms participate in the ice formation process, while soot particles could serve as IN for heterogeneous nucleation freezing. Therefore the CCN measurement was necessary to identify whether or not the soot particles and their possible activation mechanisms were comparable from test to test. The heating temperature of the sulfuric acid generator was adjusted to achieve the same CCN activated fraction at the same supersaturation.

To generate aircraft exhaust-like soot particles in the laboratory, a camp stove was used to simulate the high temperature combustion process of fuel (Jet A with PRIST) inside an aircraft jet engine. The fuel was first vaporized in a small tube and then ignited in a blue flame (1400°C). The stove was then put into the closed and pre-cleaned grain bin (volume $\sim$ 50 m^3) for a certain time period (about 2 minutes in this study). After the stove was taken out, a recirculation blower was turned on for 1 minute to mix the air inside the bin. After ten minutes measurements showed that the total condensation nucleus concentration was on the order of 10^5 cm^{-3}. The evolution of the size distribution was observed from a series of DMPS (Differential Mobility Particle Spectrometer) scans, and is shown in one example in Figure 6.1. The first scan started about 10 minutes after the blower was stopped. The distributions show that strong coagulation inside the grain bin caused the mode size of the distribution to grow to larger sizes over time. However, the number concentrations of 0.05 μm particles were fairly stable, even 80 minutes later. This stability allowed a time window to conduct CFD measurements on stable concentrations of a monodisperse aerosol (0.05 μm), generated by passing the combustion particles through a DMA before sending them to the CFD. Additionally, to monitor the real-time variation of the number concentration of soot particles, a CN counter was set up in parallel with the CFD.

The CCN activities of the jet fuel soot particles were measured to infer the soluble fraction of the mixed insoluble particles, with the assumption that the insoluble part serves as a core. Köhler theory (see Appendix A) was used to calculate the equivalent CCN size or the soluble fraction at certain critical water vapor saturation [Pruppacher and Klett, 1997]. The critical supersaturation here is defined as 50% of input soot particles activated as cloud droplets.

The soot particles from either generation system passed though the pre-cooler that was operated at -30°C, before entering the CFD III. Details of this instrument can be found in Chapter 2. The approach to determine activated fractions was the same as the sulfate/sulfuric acid homogeneous ice formation experiments (details can be found in Chapter 5). Since the experimental procedure was to step up the humidity of the CFD at fixed temperature, the observed activated fraction did not always sit at 0.1%, 1% or 10% fraction. Therefore, interpolation had to be used to deduce the conditions at which these fractions occurred. Each data point is an average of four to five size distribution spectra, while the humidities presented here are based on 8 to 10 measurements. The precision and uncertainty of CFD measurements are discussed in Appendix B.

6.2 Results and discussion

There were two series of experiments in this study: freezing of commercial soot particles untreated or coated with different amounts of sulfuric acid, and freezing of untreated, mono-dispersed combusted jet fuel soot particles.

6.2.1 Commercial soot particles with and without sulfuric acid coating

Figure 6.2 shows the CCN active fractions of treated/untreated commercial soot particles at different water supersaturations. The untreated soot particles were the least active as CCN. Within the supersaturation range that the TGDC reliably produces, a critical level of activation was not observed. This was expected because of the hydrophobic surface of these carbon particles. After absorbing some sulfuric acid vapor, the CCN activation of soot particles was enhanced dramatically, and the degree of activation was a function of how much sulfuric acid was on the particles. At 70°C and 75°C, when the vapor pressure over the sulfuric acid drop used in the coating system was slightly elevated over the ambient conditions, no detectable homogeneous nucleation of sulfuric acid particles happened in the generator. But at 75°C, the active fraction of soot particles jumped from below 0.2% to ~30% at 0.6% supersaturation with respect to water. At 85°C, homogeneous nucleation formed some small H_2SO_4 drops, evident as small (~0.016 μm) particles detected by the CN counter. At the same time, the active fraction of soot particles increased to 75%

at 0.6% supersaturation. Calculations showed that to activate 50% of particles as CCN, with 0.25% and 2% (by weight) of sulfuric acid on soot particles required 0.7% and 0.25% water super-saturation. These two percentages correspond to ~1 and a few layers of single molecule coverage on the mean sized soot following the assumption of solid spherical soot particles with uniform coating, as suggested by Wyslouzil *et al.* [1994]. If the particles are not spheres but chain aggregates of 0.24×0.24 μm size, 5 monomers would be lined up (0.09×0.45 μm). The same calculations then show 1.3 and 9.6 layers for 50% activation at 0.7% and 0.25% supersaturation. The uncertainties of the CCN measurements can be found in DeMott *et al.*[1999]. Hereafter, these two conditions are referred to monolayer and multilayer coverage.

Table 6.1 lists the ice formation conditions of monolayer soot particles at the CFD

Table 6.1: Relative humidity with respect to water for 0.1%, 1%, and 10% activation of commercial soot particles as ice crystals as a function of CFD temperature in the case of monolayer coverage of H_2SO_4.

Freezing temperature (°C)	-45	-47.5	-50	-53	-56	-57.5	-61
RH_w for 10%	101	100	99.5	99	98.5	96	95
RH_w for 1%	100	99	98	96.5	96.5	94	92
RH_w for 0.1%	98.5	97	96.5	91.5	94.5		88.5

temperature and relative humidity conditions. Similar to the results of sulfates, the conditions for 0.1%, 1%, and 10% activation are spread over the order of several percent relative humidity. This might be an inherent feature of the CFD, or may be the result of a combination of nucleation rates at different RH_w values and the relatively short residence time (~12 sec.) in the CFD.

Figure 6.3 shows the 1% activation humidities required for ice formation by untreated, monolayer, and multilayer coated soot particles. The activation humidities of untreated soot particles have a nearly linear relationship with temperature. It is most likely that heterogeneous nucleation, not homogeneous nucleation, is the mechanism of ice formation in this case. The relatively low concentration and short residence time in the CFD make contact freezing not important, and immersion freezing cannot be detected by the CFD,

therefore condensation and deposition freezing are the two modes that can initiate nucleation in these experiments. Deposition is mainly driven by the supersaturation with respect to ice (SSi). The 1% ice formation conditions for untreated soot from -40°C to -60°C have a mean value of 56.3% SSi with standard deviation of 5.1% SSi (Figure 6.4). With a monolayer coating of sulfuric acid, the capability of heterogeneous ice formation on soot particles seems to be suppressed, although there are too few tests to establish statistical significance. The average 1% activation humidity is 59.2% SSi, about 3% SSi higher than untreated soot, and the standard deviation is 3.0% SSi. Differences compared to untreated particle results were not significant. Nevertheless, we believe that the conditions for ice formation are most consistent with homogeneous freezing of diluted sulfuric acid in this case.

With multilayer sulfuric acid coverage on the commercial soot particles, apparent homogeneous ice formation dominated at temperatures above -52.5°C. Below that temperature, heterogeneous nucleation clearly is increasingly important. At -60°C, the 1% activation humidities are about 10% lower than those required by untreated soot. At -60°C, 1% of the soot particles formed ice at 82% RH_w. Since the densities of concentrated sulfuric acid and the commercial soot particles are 1.98 g cm^{-3} and 1.86 g cm^{-3}, the 2% by weight sulfuric acid coating on the average size soot particles equates to the volume of a 0.05 μm pure sulfuric acid drop. Calculations show that it is not possible that the lower RH_w freezing conditions could be achieved even for a bulk quantity of sulfuric acid, much less for 0.05 μm particles, and dramatic change around -52.5°C cannot be explained only by the homogeneous freezing. The most likely explanation is that soot particles were catalyzing heterogeneous freezing nucleation.

The elevated sulfuric acid vapor pressure in the generator in the multilayer case also initiated homogeneous nucleation of small pure sulfuric acid droplets (~0.016 μm diameter) in the air stream. Results of freezing of these pure sulfuric acid droplets (see Chapter 5) showed that 0.016 μm sulfuric acid particles required at least 100% RH_w at -60°C, and 103% RH_w at -45°C for 1% fractional activation. This is higher than the conditions for 0.05 μm monodisperse sulfuric acid particles, as was shown in Chapter 5. The observation

that these small pure sulfuric acid drops can not form ice crystals at the humidities at which ice was detected in the commercial soot experiments provides some assurance that it is the multilayer coated soot particles which nucleate ice crystals below -52.5°C. This situation is similar to what happens in contrails where large soot particles coexist with much smaller sulfuric acid drops [Kärcher, 1998].

6.2.2 Jet fuel soot particles

To simulate ice formation by aircraft exhaust aerosols under conditions close to those in the upper troposphere and lower stratosphere, 0.05 μm jet fuel soot particles were selected by the DMA. This particle size is close to the size of fresh aircraft exhaust particles [Anderson *et al.*, 1998]. The coagulation timescale of our burning system was similar to those provided by Schumann *et al.* [1996]. Since the coagulation time depends on the particle number density, $t \sim N^{-1}$, we conclude that the soot emission index of the jet fuel soot generation system is similar to the turbofan engines described in that paper. In this series of experiments, the pre-cooler was put inline to reduce the sample humidity from the grain bin to ~74% RH_w at -30°C. CCN measurements showed 50% of these combustion soot particles were activated at 1.2% SSw, corresponding to 10% soluble matter by weight [via Köhler theory]. This is far more than a monolayer coating.

The dependence of the ice formation humidity on temperature is plotted in Figure 6.5. Similar to all of the previous CFD experiments, the RH_w values for activation at 0.1%, 1% and 10% fractions show a broad range at all temperatures, while their tendencies are in good agreement. From the figure, these soot particles need high humidity close to water saturation to initiate the ice phase. It is unlikely that heterogeneous nucleation occurs, otherwise ice formation would initiate at much lower humidity.

The studies described in Chapter 5 showed that the phase state of the soluble fraction has a strong influence on the ice formation of particles. After aging for about 10 minutes, there was a chance that the acid in jet fuel soot particles was neutralized by ammonia in the air. If this were the case, and the solution crystallized, this would support a requirement of high humidity to form ice. As a test of the state of neutralization, the particles were purposely deliquesced in a few experiments. Based on the results given in Chapter 5, this

exercise should have led to ice formation at a lower RH_w if the particles were initially crystalline; otherwise, it can be concluded that the soluble fractions in all our experiments were already in solution, and not crystalline. An experiment at -55°C with the saturator showed no difference between the "wet" and "dry" experiments, confirming that the soluble part exists in solution on the soot particles. This statement must be tempered by the lack of knowledge of any organic components or their effects.

Comparison was made between the jet fuel soot results, 0.016 μm sulfuric acid, and 0.05 μm sulfuric acid (average RH_w values from Chapter 5), as shown in Figure 6.5. The results of jet fuel soot parallel the other two series of conditions, and are closer to the 0.016 μm results. If the soluble fraction is sulfuric acid, the 10% by weight coating on a 0.05 μm soot particle would form a pure sulfuric acid drop of 0.023 μm. In both 0.016 μm and 0.05 μm sulfuric acid experiments, homogeneous freezing is the mechanism of ice formation. Since the volume of 0.023 μm particles is similar to that of 0.016 μm, its freezing behavior is more close to that of 0.016 μm particles, which suggests homogeneous freezing as the mechanism that jet fuel soot particles were frozen.

6.3 Summary and conclusions

The results presented here are from preliminary experiments. Some conclusions can still be drawn based on these studies. First, heterogeneous nucleation, *e.g.* deposition or sorption, seems responsible for ice formation on untreated commercial soot particles of the sizes used below -40°C. After coating with a small amount of sulfuric acid, their capability as IN did not exhibit a statistically significant change, but may have been slightly disabled. We also infer that this altered the ice formation mechanism to homogeneous freezing. The dashed line in Figure 6.3 is the set of conditions for which 1% of 0.24 μm particles are expected to freeze in 12 seconds by homogeneous freezing of the diluted sulfuric acid on their surface. The method of calculation is the same as the discussion in section 5.2.2.3. The observed results of the monolayer coated soot particles can be closely fitted to the dashed curve. Therefore it can be concluded that homogeneous nucleation plays a role. With multilayer coverage, heterogeneous nucleation dominated below -52.5°C, and lowered the ice formation conditions by about 10% RH_w.

These are the first laboratory observations of heterogeneous nucleation on soot particles below -40°C, and suggest the potential role of aircraft exhausts particles in cirrus/contrail formation. The results from this study imply that the role of soot particles in the formation of contrails strongly depends on the content of sulfur in jet fuel. With more sulfuric acid deposits on the exhaust soot particles, more ice crystals will be formed at a certain humidity. This is consistent with the observations of quick growth, larger optical thickness, and more contrast of high-sulfur contrails [Schumann *et al.*, 1996]. Pure soot particles, or a small amount of sulfuric acid coated particles suggest that fresh exhaust soot particles require nearly water saturation to form a contrail, which is consistent with observations [Jensen *et al.*, 1998].

Hagen *et al.* [1992] reported that up to 10% soluble material is mixed with fresh exhaust soot particles, which is consistent with what we found in the 0.05 μm jet fuel soot particles. From the experimental results, homogeneous freezing is the main mechanism for these particles. This is direct evidence that soot particles in fresh exhaust require high humidity to form cirrus / contrails. However, after aging and aggregation, larger soot particles may begin to form ice at lower humidities by heterogeneous freezing nucleation.

More tests are needed to characterize additional aspects of the ice formation mechanisms for a variety of jet fuel soot particles, including the impact of the sulfuric acid coating and the size effect. To improve the confidence levels of all these results, more replicate experiments are needed. Furthermore, chemical analysis is important to define the initial phase state of the soluble fraction of the jet fuel soot particles.

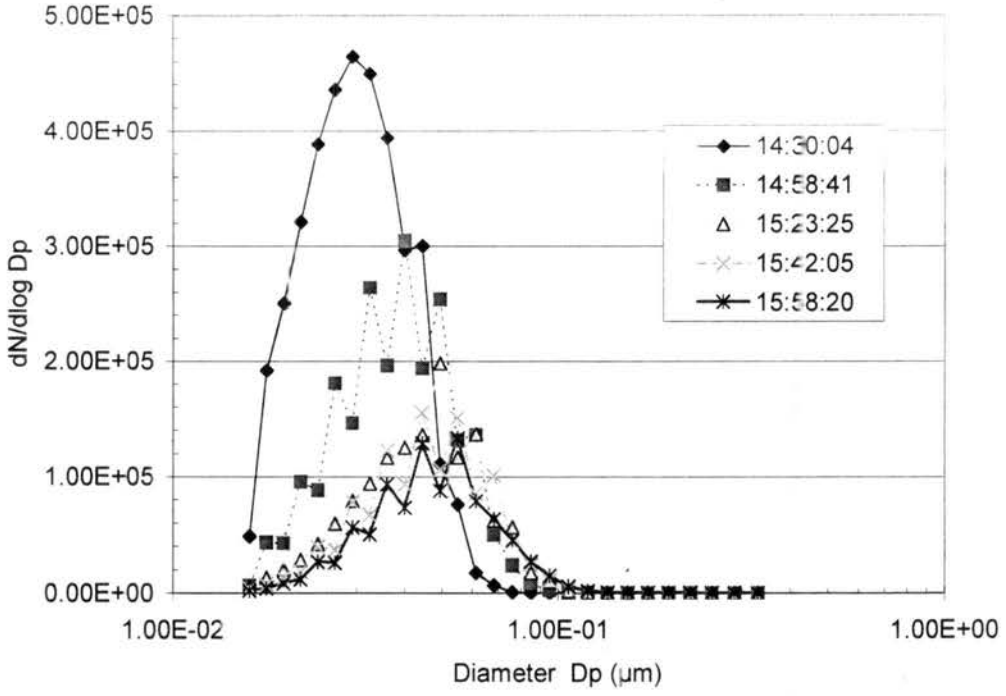

Figure 6.1: The variation of the size distribution of jet fuel soot particles with time in the grain bin.

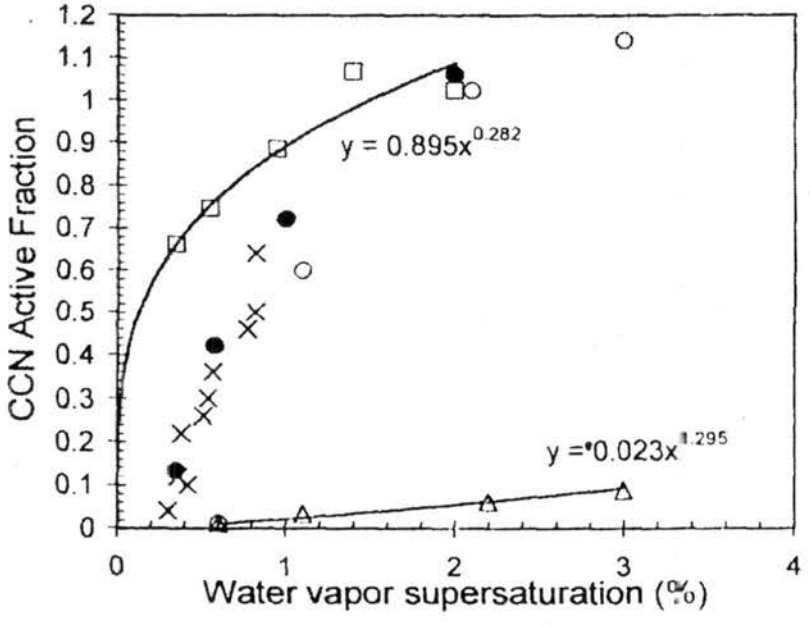

Figure 6.2: CCN activities of commercial soot particles subject to different treatments. The active fraction was determined by comparison of activated CCN concentration versus CN concentrations. Empty triangles represent untreated commercial soot particles; empty circles, crosses, solid circles, and empty squares indicate particles passed over sulfuric acid at 70, 75, 75 and 85°C, respectively.

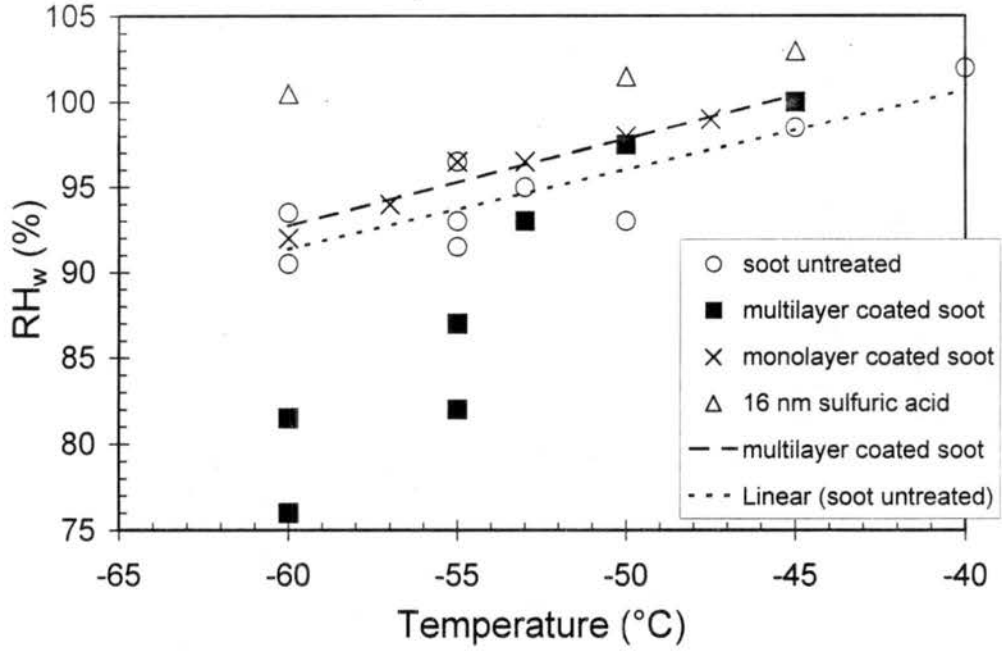

Figure 6.3: Relative humidity with respect to water required for 1% activation of commercial soot particles with different treatments and for 1% activation of 16 nm sulfuric acid particles as a function of CFD temperature.

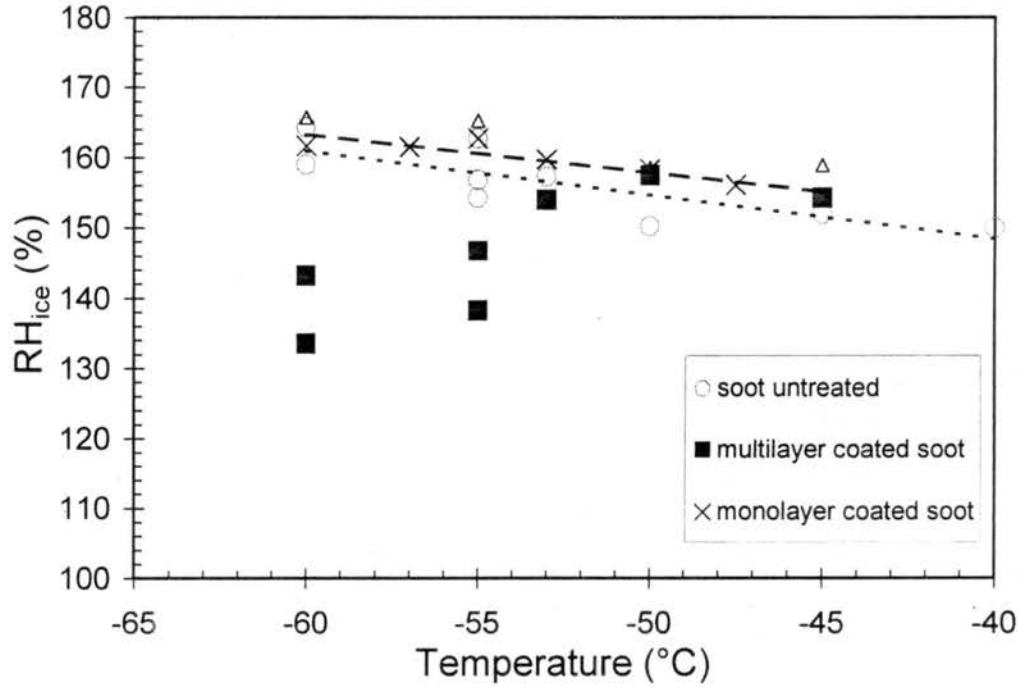

Figure 6.4: The relative humidity with respect to ice (%) required for ice formation (1% activation) with different COMMERCIAL soot particles at the CFD temperatures.

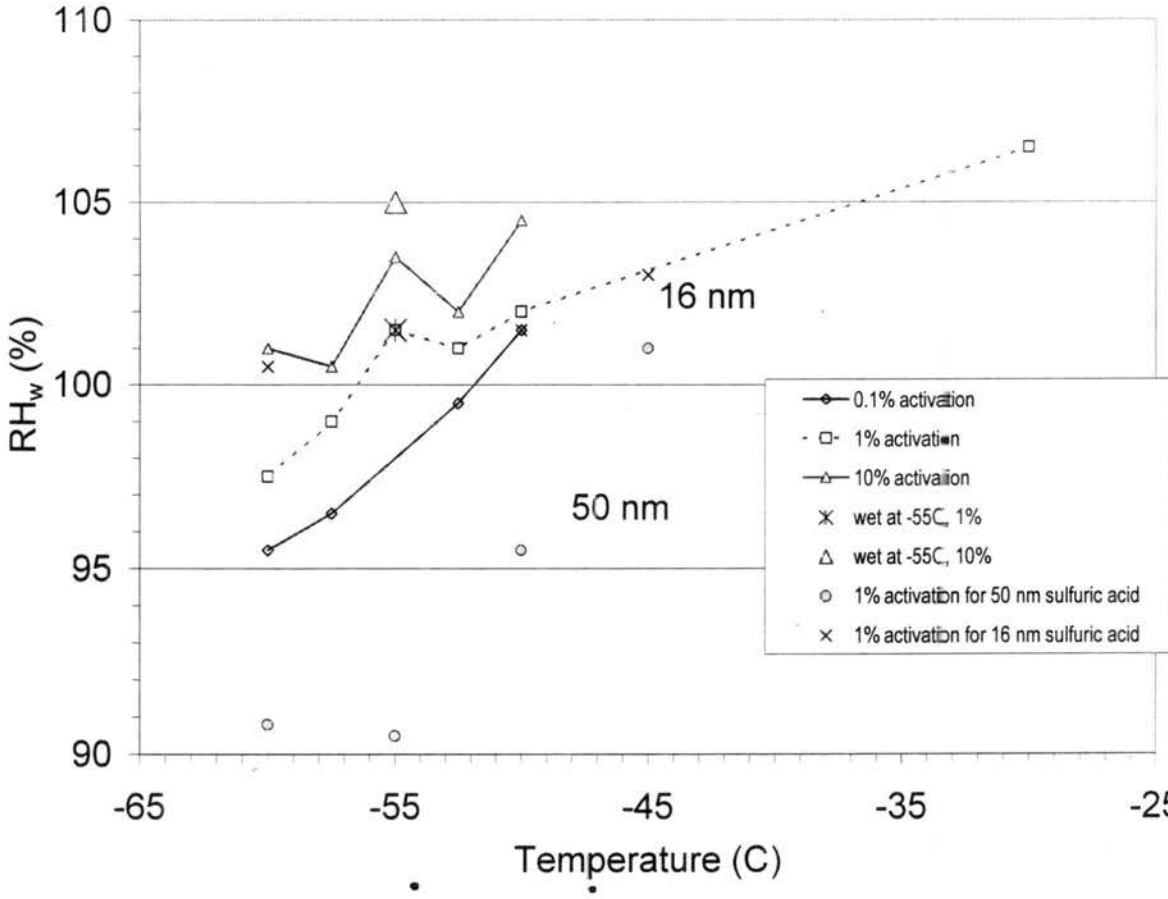

Figure 6.5. Summary of conditions for ice formation by jet fuel soot particles. "Wet" refers to the experiments that included the saturator to deliquesce the soluble portion of the jet soot particles.

Chapter 7

SUMMARY, CONCLUSIONS AND FUTURE WORK

7.1 Summary and conclusions

7.1.1 The CFD instrument

A continuous flow thermal diffusion chamber (CFD) uses two parallel, ice-coated walls to create the temperature and water vapor pressure profiles within the gap. By varying the temperatures of the walls, gradients of temperature and water vapor pressure establish a range of humidities from ice saturation to super-saturation with respect to water inside the chamber. Aerosol particles are directed/contained within a certain humidity region by two equivalent sheath flows, and they can grow as either water drops or ice crystals at fixed temperature and humidity.

Over the past few years, several types of CFD chambers were built for different applications beyond the prototype (CFD I) for development and testing. These include the airborne version (CFD II) for field measurements, and a longer version for laboratory studies (CFD III). The design principles common to all three enable ice crystals to nucleate and grow via both heterogeneous and homogeneous mechanisms. When operated in a "warm" temperature range between -30°C to -15°C, the CFD can nucleate ice crystals mainly through deposition freezing and condensation freezing. Contact freezing can increase the ice formation at most 1-2%, and therefore is not considered to be effective within the CFD. The initial phase state of aerosol particles does not impact the experimental results very much at a "warm" temperature, since the CFD is always operated close to water saturation, and all aerosol particles are going to uptake some water or ice by either condensation or deposition, without homogeneous freezing nucleation. Therefore the pre- conditioning system is not required for all heterogeneous experiments.

The two experiments with mixtures of AgI and NaCl or $(NH_4)_2SO_4$ reported in chapter 2 confirmed that the CFD is capable of nucleating the IN subset of an aerosol sample and growing them into ice crystals. Ice crystals grow rapidly and can be detected or collected at the outlet of the CFD. As a consequence, the IN and non- IN fractions can be separated chemically. The first application of the CFD to natural aerosol samples showed that crustal (silicate) and metallic particles are the two major groups favoring ice nucleation, while pure soluble sulfate is a poor IN, and could be found only in the non-IN fraction. The capability of heterogeneous ice formation by soot mixed with sulfate is likely to be explained by the active sites on soot surface.

The CFD can be used to study homogeneous freezing nucleation below -40°C. Nevertheless, a preconditioning system is recommended for most future work in this environmental regime. Reliable control of particle phase state was seen to be essential for interpretation of results such as those contained in this dissertation. More efficient cooling devices (*e.g.*, bath circulators) will be necessary to extend studies to temperatures below -60°C.

Some inherent limitations in the CFD technique were identified in this study, especially in the lowest temperature range. First of all, the vertical temperature gradient from the top to the bottom of the outside wall causes temperature and humidity inhomogeneities along the sample lamina. The longer the CFD chamber, the worse the inhomogeneities are. These temperature and humidity variations broaden the size distribution of ice crystals, since the ice crystals do not nucleate ice at the same time; some of them start near the top part, while some close to the outlet of the chamber. Although the use of a threshold size resolves the problem of miscounting droplets as ice crystals, it might cause an underestimate of the number of ice crystals. Collection of full size spectral data aids interpretation. A second limitation of the current CFD technique is the relatively short residence time. The current configuration of the CFD III gives aerosol particles on the order of 10 seconds within the CFD. Calculations show that this is enough time for heterogeneous and homogeneous ice formation to occur, but the growth relaxation times for particles in meta-stable states are not well known. A longer chamber or lower total flow rate helps to increase the residence

time, but both approaches have their own restrictions. The vertical temperature gradient of a longer chamber is worse, and the total flow cannot be below a critical rate to keep laminar flows within the CFD. The third limitation in the CFD III system is the frosting problem. When frost builds up, some fractured frost crystals could get into the flow and be counted as ice crystals. Since there is a vapor flux from the warm wall toward the cold wall, it is just a matter of time before the frost problem is severe enough to impact the results. A sensitive site where frosting can occur is the inlet transition region. If the sample is too humid, frost can be deposited onto the inlet walls. Fortunately, the frost problem only occurs after a number of hours of experimentation, depending on the ambient temperature and humidity. This provides, typically, about 2 hours duration for measurements.

Summarizing all the discussions above, it can be generally concluded that the CFD provides an effective technique to study ice formation behaviors of aerosol particles.

7.1.2 Aerosol particles in the upper troposphere and lower stratosphere and their ice formation properties

IN and ambient aerosol particles were collected in the upper troposphere and lower stratosphere, followed by individual particle analysis. The results indicated sulfate or sulfuric acid particles dominate the ambient aerosol particles, although not as much as claimed by Sheridan *et al.* [1994]. Soot particles were collected in relatively low numbers. As shown in chapter 3, the CFD separates chemically the IN from non-IN particles, and shows the different chemical characteristics between IN and the ambient aerosol particles. Among all the five aerosol categories, crustal and carbonaceous particles were good IN, while sulfate particles were poor. Clear differences were observed between the aircraft exhaust/contrail and the upper tropospheric air: larger fractions of metallic and carbonaceous particles and smaller fractions of crustal particles were found in the contrail. The origins of background aerosols were also found to influence the chemical compositions of IN particles. The continental based IN sample contained 11-31% ($\pm$7%) crustal particles, and $<$ 16% sulfate related particles. The marine IN samples had less than 10% crustal, but 40-60% sulfate particles. Interestingly, many metallic particles, possibly pure metals, oxides, or carbonates were collected in the IN samples, especially those influenced by the exhaust/contrail.

Among these, Ti is a major constituent that can be related to the materials in aircraft engines.

At the low temperatures of upper tropospheric conditions, homogeneous freezing of particles is also possible, given high enough humidity. To focus on homogeneous freezing, we performed experiments with totally soluble CCN particles to eliminate the heterogeneous freezing mechanisms. As dominant CCN species in the upper tropospheric aerosols, sulfate and sulfuric acid particles were tested with the CFD chamber in the laboratory to measure the onset conditions of ice formation. In order to observe the condensation growth of droplets, 0.2 μm ammoniated sulfate particles were selected by the DMA, followed by the pre-conditioner to establish their initial phase state before freezing. This size, 0.2 μm, is consistent with what we observed in ambient aerosol samples of the upper troposphere, although it is possible that collection and analytical techniques might bias the distribution. The sulfuric acid experiments used a different size, 0.05 μm, reflecting the limitation of the sulfuric acid generator, and the observation [Schumann et al., 1996] that sulfuric acid particles are mostly between 0.018 μm to 0.1 μm in young aircraft exhausts. A detailed discussion of the experimental procedures and approach was given in chapter 5, and statistical analyses were outlined there.

With the understanding of heterogeneous IN particles and the homogeneous freezing of pure soluble CCN particles, some preliminary measurements were conducted to investigate the ice formation of pure commercial soot particles, sulfuric acid coated soot particles, and jet fuel soot particles. These results helped to explain the formation of contrail and cirrus clouds in the upper troposphere, as well as to estimate the impact of anthropogenic pollution (aircraft exhaust) on global climate change. In the jet fuel soot experiments, 0.05 μm particles were selected, based on the observations of Pueschel [1996].

The following major conclusions may be drawn from this part of the work:

- The history of the phase state of a particle decides its ice formation conditions. For a deliquesced solution drop, freezing requires much lower humidity than for a dry crystalline particle. For ammonium sulfate at -55°C, the difference between these two could be as large as 10.5±1% RH. The two onset freezing conditions merge together at warmer temperatures, close to -40°C.

- There are significant differences between ice formation in 0.2 μm ammonium sulfate and 0.05 μm sulfuric acid particles. After correcting for size effects by looking at the melting point depression coefficient, it is concluded that there is no significant difference between the ice formation conditions of ammonium sulfate and sulfuric acid. In general, results for other compounds, for example, ammonium nitrate or sodium chloride, are needed to confirm that composition plays a smaller role than does particle size.

- After comparing these results with field observations of the onset conditions for cirrus clouds [Heymsfield and Miloshevich, 1995; Heymsfield *et al.*, 1998], it was concluded that small sulfuric acid particles are unlikely to serve as ice nuclei for continental cirrus clouds. Submicron ammoniated sulfate particles are possible candidates at temperatures below -45°C. Both particle types could satisfy the onset conditions of cirrus clouds over oceans.

- Pure (commercial) soot particles are not good CCN particles. Heterogeneous freezing nucleation on these particles starts at subsaturations with respect to water. A monolayer of sulfuric acid coating does not appear to improve the ice nucleating ability of ~0.250 μm commercial soot particles, but seems to be disabled it. More sulfuric acid coating does not enhance ice formation either above -52.5°C; below this temperature, freezing of heavily coated particles occurred at about 10% lower humidity than untreated particles.

- The anomalous behaviors of soot particles with different treatments can be explained by the combination of heterogeneous and homogeneous freezing mechanisms. The primary pathways are heterogeneous deposition nucleation for untreated soot particles, homogeneous freezing for monolayer coated soot particles and for multilayer coated particles above -52.5°C, and heterogeneous freezing nucleation for multilayer coated soot particles.

- The jet fuel soot particles generated in our laboratory contain about 10% by weight soluble materials, and 0.05 μm particles required at least 95% RH at -60°C to initiate

freezing. This result implies that fresh exhaust requires high humidity conditions to form contrails. After aging and aggregating into larger soot particles, their onset conditions are probably close to the envelope of observed cirrus cloud conditions.

7.2 Recommendations for future work

While this study has addressed many issues related to the ice formation mechanisms in the upper troposphere, it left many questions unanswered, due to limits of instrumentation and time. The main suggestions for future studies are offered here:

- Chemical analytical evidence is needed for the presence of letovicite in the laboratory. Bulk solution of ammonium bisulfate could be crystallized at low humidity, and followed by the separation of solid and liquid phases. Either pH measurements of the solution or ion chromatograph analysis of the solid phase will verify the existence of a new phase.

- Aerosol particles composed of different compounds can be frozen with the same approach as the sulfate experiments, to understand whether or not the chemistry of particles is important to the onset ice formation conditions. Sodium chloride and ammonium nitrate are two compounds that are important for understanding the ice formation of cirrus clouds with ocean origins and cirrus clouds with excess amounts of ammonia present.

- Additional experiments are needed in the jet fuel soot and the commercial soot study. Some chemical or freezing analyses would be helpful to identify the chemical composition of the soluble fraction of the jet fuel soot particles. One approach is to pass the particles through a bath of ammonia water solution, to neutralize the particles, and compare freezing behavior with that for particles without ammonia treatment. If a difference is observed, it would suggest that the soluble fraction is not ammonium sulfate.

- The ice formation of clay or crustal particles would be another very interesting project, since crustals were found to be one of the major components of ice nucleating particles in the upper troposphere [Chen *et al.*, 1998]. After mixing with

soluble materials, their freezing behaviors are expected to change, based on what was observed for commercial soot particles.

- In the natural atmosphere, numerous organic compounds exist. Some of them can be dissolved into solution drops, and some of them condense onto the insoluble aerosol particles. More specifically, most of soot particles in aircraft exhaust might be coated or absorb some fuel vapors, hence will change their ice formation mechanisms.

- So far there have been several campaigns to measure heterogeneous ice nucleating particles from the lower troposphere to the lower stratosphere with the CFD II on aircraft. Nevertheless, the chemical compositions of ice nuclei are still not well understood in the free troposphere. Some surface observations, *e.g.* in the Smoky Mountains, at Niwot Ridge(Colorado), or at Storm Peak Laboratory, would help advance understanding of ice formation processes in lower clouds, such as stratus or cumulonimbus. Linking a CFD with real time mass spectrometric techniques for analyzing IN in real time would be particularly useful.

- Some CFD refinements are recommended, such as improving the temperature monitoring and control system, and the optical particle detection system. Replacing the thermocouples with thermistors will decrease the uncertainty of temperature measurement by an order of magnitude, hence improve the precision of temperature and humidity dramatically. A cold bath around the outer CFD wall could reduce the temperature gradient from the top to the bottom, and reduce the ice crystal size broadening problem. The current optical counter can not detect small particles below 0.3 μm, which is critical for the measurement of haze drop growth.

Appendix A

THERMODYNAMIC BASIS OF SOLUTION DROPS AND HOMOGENEOUS FREEZING

A.1 Equilibrium between an aqueous solution drop and humid air

The following development is taken from the text by Pruppacher and Klett [1997].

From thermodynamics, we can write the equilibrium vapor pressure surrounding a solution drop with radius r as

$$\ln(\frac{e_a}{e_{sat,w}}) = \ln a_w + \frac{2M_w\sigma_{s/a}}{RT\rho_w r} \tag{A.1}$$

where e_a is the vapor pressure around the drop, $e_{sat,w}$ is the vapor saturation pressure over a flat surface of water, a_w is the water activity of solution, M_w is the molecule weight of water, $\rho_{s/a}$ is the surface tension between the interface of solution and air, R is the gas constant, T is the temperature of the drop, ρ_w is the density of water, and r is the radius of the drop. Here we assume that the density of diluted solution is the same as the density of water.

Due to the limitations of current knowledge, we do not know the dependence of the activity coefficient of water on curvature, and therefore neglect it based on understanding in other similar situations. The water activity can be written as

$$a_w = \exp[-\frac{3v\Phi_s m_s M_w}{M_s(4\pi a^3\rho_s'' - m_s)}] \tag{A.2}$$

For a sufficiently dilute solution, we assume $m_s << m_w, \sigma_{s/a} < \sigma_{w/a}, \Phi_s \simeq 1, and\ \rho_s'' \simeq \rho_w$, and we have the more familiar form as

$$S_{v,w} = 1 + \frac{A}{a} - \frac{B}{a^3} \tag{A.3}$$

where A = $\frac{2M_w\sigma_{w/a}}{RT\rho_w}$, and B = $\frac{3\nu m_s M_w}{4\pi M_w \rho_w}$. This is called the Köhler equation; $\frac{A}{a}$ is called the curvature term, and $\frac{B}{a^3}$ is called the solute term.

The Köhler equation is interesting, because it has opposite signs before the curvature term and solute term. When the solute term is smaller than the curvature term, the vapor pressure over a solution drop is larger than the saturation vapor pressure, and vice versa. When we apply a partial differential with respect to radius to $S_{v,w}$, we have

$$\frac{\partial S_{v,w}}{\partial a} = -\frac{A}{a^2} + \frac{3B}{a^4} \tag{A.4}$$

When $\frac{\partial S_{v,w}}{\partial a} = 0$, we have $a = \sqrt{\frac{3B}{A}}$. This a is called the critical radius. It corresponds to the maximum humidity that a solution drop can be in equilibrium with without spontaneously growing to larger sizes. Below this humidity and the critical radius, the solution drop exists in stable equilibrium with its environment. Above this humidity, the drop will continuously grow as long as water vapor is available.

This equilibrium state of the solution drop is important, since it defines how big a solution drop can grow under certain temperature and humidity conditions. In the CFD studies, we started with small drops or dry crystals. At the outlet of the CFD, they have grown to a size in equilibrium with the preset humidity in the CFD. That equilibrium was achieved was confirmed by slowing the total flow rate to provide a longer residence time (18 seconds). No size changes were observed within the resolution of our optical detector.

A.2 Homogeneous nucleation of water drops and ice crystals

In this section, we will discuss the theories and assumptions for homogeneous nucleation.

The phase transformation of water can be described by the Clausius-Clapeyron equation [pp. 116, Pruppacher and Klett, 1997]. With this equation, the relation between two phases separated by a flat interface, for example, between liquid water and ice, or water vapor and liquid water, or water vapor and ice, can be derived as the slope of the phase boundary curve in the $p - T$ plane.

$$\frac{dp}{dT} = \frac{L_{phase1,phase2}}{T(\nu' - \nu'')} \tag{A.5}$$

where p is the pressure of water, T is the equilibrium temperature of the system, ν' and ν'' are the volumes of phase 1 and phase 2, and $L_{phase1,phase2}$ is the latent heat for phase transformation between phase 1 and phase 2.

Considering the bulk phases to be ice and water vapor, and assuming that the volume of ice is negligible compared with the volume of water vapor, the saturation vapor pressure $e_{sat,ice}$ is determined from the equation

$$\frac{de_{sat,ice}}{dT} \simeq \frac{L_s}{T\nu_{V,0}} \tag{A.6}$$

With the assumption of water vapor as an ideal gas, and applying the ideal gas law, we have the temperature dependence of water saturation vapor pressure as

$$\frac{dlne_{sat,i}}{dT} \simeq \frac{L_s}{RT^2} \tag{A.7}$$

All these approximations are sufficient in cloud physics, because of low pressure and relatively low temperature in most atmospheric conditions.

To extend the equilibrium equation to a curved interface, we need to include the surface tension and the curvature effect, and have

$$\frac{e_{a,i}}{e_{sat,i}} = \exp(\frac{2M_w\sigma_{i/v}}{RT\rho_i a}) \tag{A.8}$$

In this equation, $e_{a,i}$ is the vapor pressure over the ice particle, $e_{sat,i}$ is the saturation vapor pressure at that temperature, $\sigma_{i/v}$ is the surface tension between the ice and vapor phases, a is the radius of ice crystal, ρ_i is the density of the ice crystal, and R is the gas constant.

All of the above are based on thermodynamic principles. Thermodynamics outlines the equilibrium state of a system, and is insufficient for kinetic processes like ice crystal formation. Nucleation to establish equilibrium cannot happen before suitable solid surfaces are presented. This occurs not in a continuous manner, but as a fluctuation in time and space of temperature and density in the parent phase. As we discussed in Chapter 1, heterogeneous nucleation is one pathway to start it. Here we talk about the other possible pathway, homogeneous nucleation. In this case, no foreign substances are present in the water droplets. In the following, we start with the homogeneous nucleation of water from

vapor; similar operations can be applied to the process of ice crystal formation from water droplets.

Water molecules keep moving no matter what phases they exist in. The movements help to form clusters of water molecules. The number of molecules varies in a cluster and can be from several to hundreds. The binding energy mainly comes from the hydrogen bond between hydrogen and oxygen of water molecules. From physical chemistry measurements, we understand that this kind of bond is very weak, and easily broken. Therefore under certain conditions, the process of cluster formation and dissociation reaches equilibrium with the same reaction rates. These clusters are called embryos. At a critical vapor pressure, some embryos with more water molecules will grow big enough to form a germ size. A germ will proceed to grow spontaneously and thereby produce a macroscopic phase change. To reach the critical vapor pressure for this process, it requires supersaturation in the system, which can be produced by supercooling of the vapor.

For homogeneous nucleation of water drops, the observable quantity is the number of water drops formed per unit time. Thus in experiments, we are interested in the rate of drops appearing in the system as a function of the prevailing saturation ratio $S_{v,w}$. The rate is called the nucleation rate by J, representing the number of drops appearing per unit volume and per unit time. The assumption behind this is that there is a one-to-one relation between the germs and the drops. As one germ is formed, it will grow into a drop, and every drop contains only one germ. Thus we estimate the nucleation rate as

$$J = \frac{\alpha}{\rho_w}\left(\frac{2N_A^3 M_w \sigma_{w/v}}{\pi}\right)^{1/2}\left(\frac{e_{sat,w}}{RT}\right)^2 S_{v,w} \exp\left[\frac{-\Delta F_g}{kT}\right] \tag{A.9}$$

where α is the condensation coefficient; ρ_w is the density of water; N_A is Avogadro's number; M_w is the molecule weight of water; $\sigma_{w/v}$ is the surface tension between water and water vapor; ΔF_g is the energy per molecule of water germ formation; and k is the Boltzmann constant.

Before conducting the same derivation for a supercooled water system, we need to discuss the differences between the nucleation of water embryos from supersaturated vapor and ice embryos from supercooled water. In the supercooled water, water molecules are

closer to each other, so the interactions are stronger. The formation of germs is a reorientation of water molecules from water-to-water bonds to water-to-ice bonds. More energy is needed in the homogeneous freezing process from the water drop than that in the water-vapor system. The difference can be represented by the molar Gibbs free energy difference between those two states. Using this, we can rewrite the nucleation rate of homogeneous ice germs in supercooled water as

$$J = 2N_c(\frac{\rho_w kT}{\rho_i h})(\frac{\sigma_{i/w}}{kT})^{1/2} \exp[-\frac{\Delta g\ddagger}{RT} - \frac{\Delta F_g}{kT}] \qquad \text{(A.10)}$$

Here N_c is the number of monomers of water in contact with unit area of the ice surface; k is Boltzmann constant, and g is the activation energy per mole for the transfer of water molecules across the ice-water interface.

So far, it looks like we could determine the nucleation rate, as long as we know the energy barriers to form germs from supercooled water, and the surface tension between ice and liquid water. Unfortunately, all those parameters are not accessible by experiment unless assumptions are made. In past work, people have identified the Gibbs free energy with the activation energy $(\Delta g\ddagger)_{act,w}$ for self-diffusion in water. The comparisons between theoretical computations, cloud chamber studies and field observation made by Pruppacher and Klett [1997] show that this approach underestimates the nucleation rate especially in the temperature range between -43 and -33°C. A similar situation exists in estimating the energy of germ formation. Although there are two avenues to proceed, either the classical approach based on thermodynamic arguments, or the molecular model, uncertainty between the classic theory and the laboratory and field measurements still cannot be resolved from current available thermodynamic data.

Several conclusions can be drawn from the equation (A.10). First, the nucleation rate of pure water drops strongly depends on the temperature, as $T^{1/2} * \exp(T^{-1})$. The ice nucleation rate is below 1 cm^{-3} s^{-1} before the system is supercooled 30°C. For a drop with 0.1 μm diameter, the nucleation rate has to be 2.0×10^{15} cm^{-3} s^{-1} to produce a germ. This nucleation rate requires the drop to be supercooled by at least 42.5°C [Pruppacher, 1995]. The other issue affecting the nucleation rate is the density of water. As extrapolated

by Pruppacher [1995], the density of water decreases from 0.98 g cm^{-3} at -30°C to 0.93 g cm^{-3} at -44°C. Thus it adds an additional dependence of the nucleation rate on the temperature. In the supercooled water system, no supersaturation ratio can be calculated. This is a difference between the homogeneous nucleation mechanisms of ice-water and vapor-water systems. But there are also temperature dependencies in the activation energy $\Delta g\ddagger$ and the energy of germ formation. Since those two energy barriers have exponential forms, J is extremely sensitive to them. Summarizing the discussion, the homogeneous nucleation rate of ice from supercooled water increases with the temperature supercooling. The relationship is as shown in Figure A.1.

In the case of a supercooled solution, equation (A.10) can be used to calculate the homogeneous nucleation rate. But as expected, the solution changes various parameters that characterize supercooled homogeneous nucleation. First, the presence of solute in drops decreases the viscosity of water and the specific heat. Therefore the increased clustering in supercooled water with decreasing temperature is hindered. For the solution drops, the interface energy (surface tension) between water and ice and the interface transfer of water molecules is increasingly affected by salt ions. Additionally, salt ions are selectively absorbed at the ice-water interface. Thus it is obvious that the net effect will lower the homogeneous nucleation rate.

While the germ grows, more water molecules are removed from the liquid phase, and leave the solution more concentrated. As we have said, the concentrating solution will decrease the growth rate, and the glaciation becomes impossible to complete unless more water vapor is available to dilute the liquid phase. Higher concentrations of solution require lower humidity for equilibrium. In an open system, water vapor will proceed to condense. The combination of ice formation and condensation is the complete freezing and growth of the ice crystal, and is the process occurring in our CFD chamber. Fixed humidity is provided by the steady-state flow in the space between two iced walls. While the ice germ starts to form inside the aerosol drops, the vapor source (from the warm wall) provides a continuous incoming vapor flux to the drops for dilution and growth.

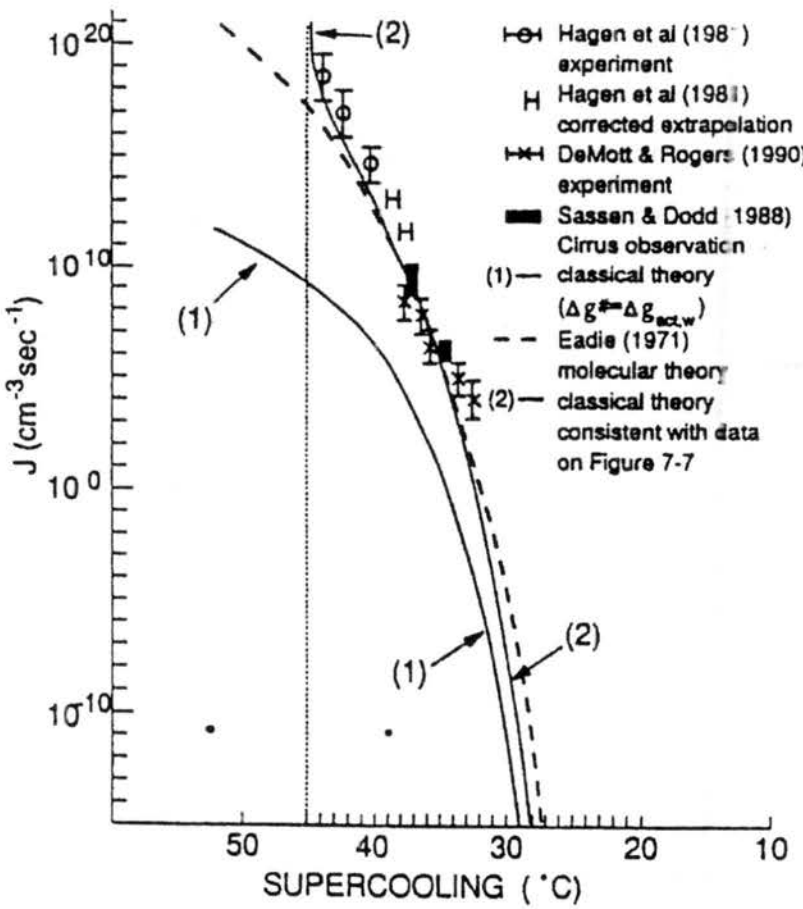

Figure A.1: Variation of the rate of homogeneous ice nucleation in supercooled water. (1) Classical theory; (2) Classical theory based on recent values for surface tension, latent heat and energy barrier. Dashed line: molecular model. Cloud chamber experiments: O Hagen *et al.*[1981]. H data of Hagen *et al.*[1981] extrapolated by Pruppacher and Klett [1997], × DeMott and Rogers [1990], and observations at the cirrus cloud level [Sassen and Dodd, 1988]. (Scanned from Pruppacher and Klett [1997] without permission).

Appendix B

UNCERTAINTY ANALYSIS FOR THE CFD MEASUREMENTS

The temperatures and relative humidities are the two most important variables we measure, and they define the ice formation behaviors of aerosol particles. For laboratory measurements, the uncertainty of the results is very important to evaluate the quality of data, and to make comparisons among results from different techniques. In this section, we will discuss the uncertainties of the key measurements made in our experiments and will evaluate the magnitudes of the associated errors.

B.1 Temperature measurements

There are two sets of temperature probes attached to the two walls of the CFD. One consists of thermocouples, and the other one is thermistors. In the chamber, a thermistor was attached at the half-height of every wall, to measure the temperature. The precision of the thermistor is higher than that of the thermocouple, about $\pm$ 0.1°C vs. $\pm$ 1.0°C. But only one temperature point on each wall may not represent the conditions of the whole chamber. Therefore for all our experiments, we used the thermocouples to measure the wall temperature.

A thermocouple is a temperature measurement sensor that consists of two dissimilar metals joined together at one end (a junction) that produces a small thermoelectric voltage when the junction is heated. The change in thermoelectric voltage is proportional to the voltage. All of the thermocouples used on the CFD are "T" type, which is made from copper and constantan. As temperature varies, copper serves as the positive, and constantan as the negative junction. The "T" type thermocouple can be used in oxidizing, reducing, inert or vacuum atmospheres up to 370°C. The error limit is $\pm$ 0.5°C or 0.4% (Omega Inc., 1992).

There are a total of seven thermocouples attached on the CFD walls, three on the cold wall, four on the warm wall. The cold cylinder of the CFD is the inner one, cooled by a reservoir of Syltherm. Hence the temperature distribution over the cold wall is more uniform. The three thermocouples were attached at the top, middle and bottom positions. The outside cylinder works as the warm wall, and was cooled by coils soldered to it. Even though four layers of insulation were used to reduce the heat exchange with room air, the warm wall still experiences some heat transfer. With the combination of the small heat capacity of coolant flowing through the coil, the temperature distribution over the warm wall was not as good as the cold wall. Hence more thermocouples were used for better measurements. Then the averages were used to represent the temperature on each wall.

So far when we talked about the wall temperatures, we meant the temperatures of the two cylinders, not the temperatures of the ice layers covering the cylinders. But in the calculation of vapor profiles, the temperatures of the ice surface are the ones to be used. There is a small difference between those temperatures. Of course, this adds one more uncertainty to the accuracy of our temperature measurements. As a good approximation, we assume that the wall and ice surface temperatures are equal.

Thermocouples 0, 1, 5, and 6 are on the warm wall, and 2, 3, and 4 are on the cold wall. From the discussion above, we can derive the uncertainties in the wall temperatures as follows.

$$T_{warm} = \frac{T_3 + T_4 + T_2}{3} \tag{B.1}$$

$$T_{cold} = \frac{T_1 + T_5 + T_6 + T_0}{4} \tag{B.2}$$

where T_n corresponds to the temperature of thermocouple n.

Next, we examine the vertical profiles of temperature. As an example on Feb. 18, the experiment was set up at -55°C. When both walls reached -55°C, the temperatures for each thermocouple were recorded as Table B.1.

The standard deviations are representative of those observed in our experiments. Therefore we use these values in the following calculations.

Table B.1: The temperatures measured by thermocouples along the warm wall of the CFD on Feb. 18, 1999.

Thermocouple	0	1	5	6	2	3	4
Temperature(°C)	-53.0	-54.5	-55.5	-55.0	-53.0	-55.0	-54.5
Average(°C)	-54.5				-54.2		
S.D. (°C)	=1.1				±1.0		

B.2 Flow rate measurements

The laboratory CFD measures the total flow and the sheath flow with two mass flow meters (Microbridge AWM 5104VN). There are another two conventional flow meters for monitoring sample flow and total flow. The sampling flow rate is calculated as the difference between the total and sheath. Knowing these flow rates, the ratio of sampling to total flow can be calculated, setting the position of the sample flow. The program needs all these values for the relative humidity and temperature calculations.

Calibration was conducted on the mass flow meters with a NIST (National Institute of Standard and Technology) traceable primary volumetric flow meter (Gilibrator Model 11616-B, Gillian Inc., NJ). Two flow cells were used, a low-flow cell (Model 17218-S, 0.02-6 LPM) with an accuracy of ± 0.196% at 2 LPM, and a high-flow cell (Model 17073-H, 2 - 30 LPM) with an accuracy of ± 0.198% at 5 LPM.

B.3 Data acquisition and RH calculation

Before we use the error propogation technique, let us discuss it briefly. For the equations as follows

$$y = \frac{m - n - p}{k} \tag{B.3}$$

$$z = \frac{mn}{p} \tag{B.4}$$

where k is a constant, and m, n, and p are independent variables with uncertainty, the error of dependent variable y and z can be written as

$$\Delta y = \frac{\sqrt{\Delta m^2 - \Delta n^2 + \Delta p^2}}{k} \tag{B.5}$$

$$\frac{\Delta z}{z} = \sqrt{(\frac{\Delta m}{m})^2 + (\frac{\Delta n}{n})^2 + (\frac{\Delta p}{p})^2} \tag{B.6}$$

where $\Delta y, \Delta z, \Delta m, \Delta n$, and Δp are the standard deviations of variables y, z, m, n, and p. These equations will be needed in the following derivations.

As discussed in Chapter 2, the temperatures, pressure, flow rates and the particle size spectra were all collected and processed by a data acquisition card installed on the computer. To calculate the temperature and humidity inside the sample lamina, there are several assumptions. First, all three layers of flows are assumed laminar. Under turbulent conditions, the aerosol particles will spread out across the annulus, hence we have no way to define the temperature and humidity they experience. Second the heat transfer and vapor mass transfer processes are quick enough to build up a thermodynamically stable state. Another important assumption is the parallel plates approximation. Compared with the diameter of the chamber, the gap between the concentric cylinders can be treated as that between parallel plates. With flow passing through the ice-coated annulus, a quasi-equilibrium state between heat diffusion and mass transfer can be established. In this steady state, both the temperature and pressure gradients between the two walls are treated as constants, which means that we can calculate the temperature and water vapor pressure at any point by simply interpolating. After we know the temperature at a point, the water saturation vapor pressure can be calculated with the Clausius-Clapeyron equation. The ratio of supersaturation vapor pressure and actual vapor pressure is calculated as the super-saturation ratio (SSw), or is expressed as the relative humidity (RH_w = SSw + 100%). The same calculations can be applied on the supersaturation with respect to ice (SSi).

Besides the temperatures of the walls, the distances of the sample flow from the walls affect its temperature and humidity. As discussed before, the sample flow was sandwiched by two equally divided sheath flows. When the temperatures of both walls are the same, no temperature gradient exists. The sample flow is located right in the middle of the annular gap. As the temperature difference increases, the sheath flows are cooled. Applying the ideal gas law again, the volumetric flow close to the cold wall becomes smaller, and pushes the sample flow away from the middle of the gap, closer to the cold wall side. Furthermore, the viscosity of air is also a function of temperature. It becomes higher

under low temperature, and changes the drag force generated by the walls. The sample flow between the sheath flows will be shifted away from the central position, and its location changes with temperature variation. In the CFD software, the interfaces of the sample and sheath flows are located first.

The program for data logging used on the laboratory CFD chamber was called "$cfd-lab.pas$", written in Pascal by David C. Rogers. The thermal diffusion and mass transfer equations and a theoretical discussion for the non-flow situation can be found in Rogers [1988]. Analog signals from thermocouples and mass flow meters are collected by a RM data acquisition card, and converted to digital signals. The computer reads these digital signals, compares them with the reference values, and computes the corresponding temperatures and flow rates. From the specification of the "T" type thermocouple, the uncertainty is $\pm$ 0.5°C [Omega and flow Co., 1996], which is two orders of magnitude higher than the errors coming from the conversion process. Therefore we can neglect error from A/D conversion without losing any accuracy.

The function to calculate the position of the aerosol sample flow is called the procedure "$Calculate-Sample-Thermodynamics$". The approach uses iteration to match the sheath flow fluxes on both sides of sample lamina. In this procedure, the air pressure inside the chamber, wall temperatures, total and aerosol flow rates were required. Besides the sample flow position, it also calculates the coefficient γ under given conditions. Here γ is a constant related to the geometry of the CFD. As the initial condition $t = 0$, the sample flow is assumed right in the middle of the annular space between two walls. Defining f as the ratio of sample flow to total flow, a and b are the positions of the two edges of the sample layer (Figure B.1). The initial values of a and b are both equal to

$$f_{a0} = f_{b0} = 0.5(1 - f) \tag{B.7}$$

The flux at position x (x is the distance from the middle point between two walls) is

$$flux = 1.5 \times mean\ velocity \times (x - \frac{x^{\frac{3}{2}}}{3d^2}) + \gamma \times \Delta T \times (\frac{x^4}{4d^3} - \frac{x^2}{2d}) \tag{B.8}$$

Then we rewrite the total flow rate in cm^3/s and the mean velocity of aerosol particles in the flow stream as

$$Q = Mass\ of\ total\ air\ flow \times volume\ ratio \times \frac{1000}{60} \tag{B.9}$$

$$Mean\ velocity = \frac{Q}{2 \times d \times circumference} \tag{B.10}$$

$$function\ F = Flux(a) \times Flux(-d) - \frac{f_{a0} \times Q}{circumference} \tag{B.11}$$

$$function\ G = Flux(a) \times Flux(b) - \frac{f_{b0} \times Q}{circumference} \tag{B.12}$$

$$\frac{dF}{da} = 1.5 \times mean\ velocity \times (1 - \frac{a^{\frac{1}{2}}}{d^{\frac{1}{2}}}) + \gamma \times \Delta T \times (\frac{a^{\frac{3}{2}}}{d^{\frac{3}{2}}} - \frac{a}{d}) \tag{B.13}$$

$$\frac{dG}{db} = 1.5 \times mean\ velocity \times (-1 + \frac{b^{\frac{1}{2}}}{d^{\frac{1}{2}}}) + \gamma \times \Delta T \times (\frac{-b^{\frac{3}{2}}}{d^{\frac{3}{2}}} + \frac{b}{d}) \tag{B.14}$$

Here d is the diameter of the center position in the annular space, and functions F and G are the integration of flux from the walls to location a and b, respectively. After integrating the flux of sheath flows, we relate the special function F and G to the mass flow rates that are easy to compare.

When both functions F and G are equal, the solutions a and b are the positions under steady state flow. Newton's method is used to find a and b, where F and G are both forced to be smaller than a preset small value $\frac{\sigma}{2}$. Here we have

$$\Delta a = \frac{Function\ F}{\frac{dF}{da}} = \frac{\sigma}{2 \times \frac{dF}{da}} \tag{B.15}$$

$$\Delta b = \frac{Function\ G}{\frac{dG}{db}} = \frac{\sigma}{2 \times \frac{dG}{db}} \tag{B.16}$$

The temperature and humidity of the aerosol sample are defined as those in the middle of aerosol lamina, where $x = 0.5 + \frac{a+b}{4d}$, is the distance from cold wall. Using equation (B.5), we have

$$\Delta x = \frac{\sqrt{(\Delta a)^2 + (\Delta b)^2}}{4d} \tag{B.17}$$

Similar to position, the temperature is calculated from

$$T_x = T_c + x \times (T_w - T_c) = T_c - x \times T_c + x \times T_w \tag{B.18}$$

Applying equations (B.5) and (B.6), we can write the error in equation (B.18) as

$$\Delta T_x = \sqrt{(\Delta T)^2(1 + 2x^2) + (\Delta x)^2(T_c^2 + T_w^2)} \tag{B.19}$$

Here we assume ΔT_w and ΔT_c are equal to ΔT.

Therefore the uncertainty in temperature depends not only on the position of the sample flow, but also on the temperatures and the temperature difference between the two walls. As discussed in the experimental procedure, both walls started with the same temperature, and the sample flow was centered between the walls, therefore the only error was from the uncertainty in the wall temperatures. As the humidity increases, the temperature difference increases and was as high as 18 K (under -60°C, 100% RH). In warmer experiments, the difference was smaller. The errors in position are important especially at high humidity and colder temperature because the gradients are steeper, leading to larger ΔT and ΔRH.

Once the temperature of the aerosol sample is known, the saturation water vapor pressure at that location can be calculated by the following equations (Buck, 1981).

Water vapor pressure over water surface above 0°C

$$\begin{aligned} &= 10^3 \times [6.1378 \times exp(17.368 \times \frac{T}{T+238.88})] \\ &= 6.1378 \times 10^3 exp[17.368 - 17.368 \times \frac{238.88}{T+238.88}] \\ &= 6.1378 \times 10^3 \frac{exp(17.368)}{exp[17.368 \times \frac{238.88}{T+238.88}]} \end{aligned} \tag{B.20}$$

Water vapor pressure over super-cooled water surface

$$\begin{aligned} &= 10^3 \times [6.1378 \times exp(17.966 \times \frac{T}{T+247.15})] \\ &= 6.1378 \times 10^3 \frac{exp(17.966)}{exp[17.966 \times \frac{247.15}{T+247.15}]} \end{aligned} \tag{B.21}$$

Water vapor pressure over ice surface

$$\begin{aligned} &= 10^3 \times [6.1378 \times exp(22.542 \times \frac{T}{T+273.48})] \\ &= 6.1378 \times 10^3 \frac{exp(22.542)}{exp[22.542 \times \frac{273.48}{T+273.48}]} \end{aligned} \tag{B.22}$$

where T is in °C, vapor pressure is in g cm^{-1} s^{-2} (dyne cm^{-2}).

Similar to the diffusion chamber of a CCN counter, the water vapor is provided by the ice surface on both walls. The vapor pressures over both walls can be calculated by the ice equation. From the error propagation table from Skoog *et al.* [1996], we have the

propagation of antilogarithm as $y = \text{antilog}_{10}\ a = 10^a$, $\frac{s_y}{y} = 2.303\ s_a$. Similarly, if $y = e^a$, $\frac{s_y}{y} = s_a$. Therefore the water pressure uncertainty over each ice surface is

$$\frac{\Delta e_{ice}}{e_{ice}} = \frac{\Delta T}{T + 273.48} \tag{B.23}$$

The water vapor pressure at the location of the aerosol lamina is interpolated from the vapor pressures over the iced walls. We have

$$\begin{aligned} e_x &= e_{ice}(T_{cold}) + x[e_{ice}(T_{warm}) - e_{ice}(T_{cold})] \\ &= e_{ice}(T_{cold}) + x e_{ice}(T_{warm}) - x e_{ice}(T_{cold}) \end{aligned} \tag{B.24}$$

$$\begin{aligned} \Delta e_x &= \sqrt{[\Delta e_{ice}(T_{cold})]^2 + (\Delta x)^2[e_{ice}^2(T_{warm}) + e_{ice}^2(T_{cold})] + x^2[\Delta e_{ice}^2(T_{warm}) + \Delta e_{ice}^2(T_{cold})]} \\ &= \sqrt{\begin{array}{l} e_{ice}^2(T_{cold})(\frac{\Delta T}{T_{cold}+273.48})^2 + (\Delta x)^2[e_{ice}^2(T_{warm}) + e_{ice}^2(T_{cold})] + \\ x^2[e_{ice}^2(T_{cold})\frac{(\Delta T)^2}{(T_{cold}+273.48)^2} + e_{ice}^2(T_{warm})\frac{(\Delta T)^2}{(T_{warm}+273.48)^2}] \end{array}} \end{aligned} \tag{B.25}$$

The relative humidity of the sample flow can be then obtained by ratioing the water vapor pressure in the center of the sample lamina with the saturation vapor pressure at that temperature. Therefore

$$RH = \frac{e_x}{e_{ice}(T_x)} \tag{B.26}$$

The uncertainty propagation for the above equation is

$$\frac{\Delta RH}{RH} = \sqrt{(\frac{\Delta e_x}{e_x})^2 + (\frac{\Delta e_{ice}(T_x)}{e_{ice}(T_x)})^2} \tag{B.27}$$

$$= \sqrt{\frac{\left\{ \begin{array}{l} e_{ice}^2(T_{cold})(\frac{\Delta T}{T_{cold}+273.48})^2 + (\Delta x)^2[e_{ice}^2(T_{warm}) + e_{ice}^2(T_{cold})] \\ +x^2[e_{ice}^2(T_{cold})\frac{(\Delta T)^2}{(T_{cold}+273.48)^2} + e_{ice}^2(T_{warm})\frac{(\Delta T)^2}{(T_{warm}+273.48)^2}] \end{array} \right\}}{e_x^2} + \frac{(\Delta T)^2}{(273.48 + T_x)^2}}$$

The uncertainty of different combinations of temperatures and flows may vary. To estimate the maximum error that could be generated by the system, we used the coldest conditions reached in the experiments. Under -60°C, to create 100% RH inside the CFD with 17 lpm total flow, the wall temperatures must be kept at -66.5°C and -48.5°C. Assuming that ΔT is within ± 1 K, we substitute these values into equation (B.27) to yield

$$\frac{\Delta RH}{RH} = \sqrt{\frac{\left\{ \begin{array}{l} 2.3342 \times 10^{-5} e_{ice}^2(206.98) + (\Delta x)^2[e_{ice}^2(224.98) + e_{ice}^2(206.98)] \\ +x^2[1.9757 \times 10^{-5} e_{ice}^2(224.98) + 2.3342 \times 10^{-5} e_{ice}^2(206.98)] \end{array} \right\}}{e_x^2} + 2.194 \times 10^{-5}}$$

and

$$
\begin{aligned}
e_{ice}(206.98) &= 10^3 \times [6.1378 \times exp(22.542 \times \frac{-66.5}{-66.5+273.48})] \\
&= 4.3917 \\
e_{ice}(224.98) &= 10^3 \times [6.1378 \times exp(22.542 \times \frac{-48.5}{-48.5+273.48})] \\
&= 47.595
\end{aligned}
$$

$$
\frac{\Delta RH}{RH} = \sqrt{\frac{4.502 \times 10^{-4} + 2.284 \times 10^3 (\Delta x)^2 + 4.520 \times 10^{-2} x^2}{e_x^2} + 2.194 \times 10^{-5}} \quad \text{(B.28)}
$$

Based on the computation of $cfd - lab.pas$, x equal 0.4 under this condition. The threshold we use in the Newton's method is very small, therefore the term including Δx can be neglected compared with the other terms in the equation. Therefore

$$
\begin{aligned}
\frac{\Delta RH}{RH} &= \sqrt{\frac{4.502 \times 10^{-4} + 4.520 \times 10^{-2} \times 0.4^2}{[4.3917 + 0.4 \times (47.595 - 4.3917)]^2} + 2.194 \times 10^{-5}} \\
&= 6.19 \times 10^{-3} \\
&= 0.62\% \qquad \text{(B.29)}
\end{aligned}
$$

which means, even at 110% RH (also as 10% SSw), the error is within ±0.7% RH.

The estimation of the temperature errors from averaging three or four thermocouples on each wall is simple. Neglecting the position variation term, and using the larger ΔT on the warm wall of 0.6°C, we have

$$
\begin{aligned}
\Delta T_x &= \sqrt{(\Delta T)^2(1+2x^2) + (\Delta x)^2(T_{cold}^2 + T_{warm}^2)} \\
&= \Delta T \sqrt{1+2x^2} \\
&= 0.7°C < 1.0°C \qquad \text{(B.30)}
\end{aligned}
$$

The uncertainty is still lower than the accuracy of the thermocouple, which is ±1°C.

There are some other uncertainties not considered here, as discussed in detail by Rogers [1982]. The calculation program $CFD - lab.pas$ assumes steady state profiles of temperature, q, and velocity and ignores their development. Also, it ignores surface roughness and transitions where the sections of the walls are joined, and the thickness of the ice layer, which changes the distance between the two walls.

Error can also come from the time for air and aerosol particles to equilibrate at the entrance to the chamber where the temperature and relative humidity fields are developing. The finite width of the sample lamina results in a range of temperature and RH across the sample. These differences in RH and temperature may favor growth of some aerosol particles over others. This is one of the reasons that some of the aerosol particles activate before others, rather than all activating at the same time.

Most of these errors in the CFD are second order when compared to the calculation we made above. Therefore they are not further investigated.

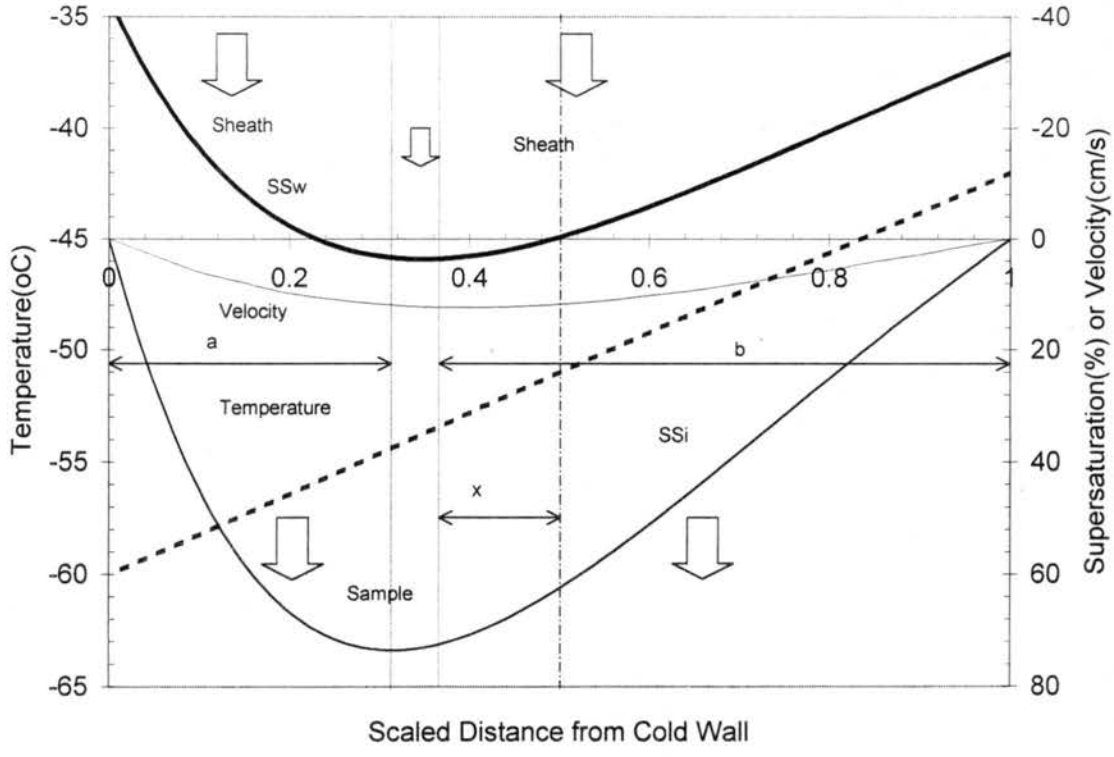

Figure B.1: Schematic of CFD temperature, velocity, SSw and SSi profiles, and the variables used in humidity and temperature calculations.

REFERENCES

American Society for Testing and Materials (ASTM), Standard specification for aviation fuels, D 1655-93a, in Annual Book of ASTM Standards, 05.01, Philadelphia, PA., pp. 555-563, 1994.

Anthony, S.E., R.T. Tisdale, R.S. Disselkamp, M.A. Tolbert, and J.C. Wilson, FTIR studies of low temperature sulfuric acid aerosols, *Geophys. Res. Lett.*, **22**, 1105–1108, 1995.

Baker, M.B., Cloud microphysics and climate, *Science*, **276**, 1072–1078, 1997.

Beard, K.V., Cloud and precipitation physics research 1983-1983, *Rev. Geophys. Space Phys.*, **25**, 357–370, 1987.

Bertram, A.K., D.D. Patterson, and J.J. Sloan, Mechanisms and temperatures for the freezing of sulfuric acid aerosols measured by FTIR extinction spectroscopy, *J. Phys. Chem.*, **100**, 2376–2383, 1996.

Bertram, A.K., and J.J. Sloan, Temperature-dependent nucleation rate constants and freezing behavior of submicron nitric acid dihydrate aerosol particles under stratospheric conditions, *J. of Geophys. Res.*, **103**, 3553–3561, 1998.

Beyer, K.D., S.W. Seago, H.Y. Chang, and M.J. Molina, Composition and freezing of aqueous H_2SO_4/HNO_3 solutions under polar stratospheric conditions, *Geophys. Res. Lett.*, **21**, 871–874, 1994.

Bigg, E.K., Some properties of the aerosol at Mauna Loa observatory, *J. Appl. Meteor.*, **16**, 262–267, 1977.

Brechtel, F.J., and S.M. Kreidenweis, Predicting particle critical supersaturation from hygroscopic growth measurements in a humidified TDMA, Part II: Laboratory and ambient studies, *J. Atmos. Sci.*, 57, in press, 1999.

Brock, C.A., P. Hamill, J.C. Wilson, H.H. Jonsson, and K.R. Chan, Particle formation in the upper tropical troposphere: a source of nuclei for the stratospheric aerosol, *Science*, **270**, 1650–1653, 1995.

Buck, A.L., New equations for computing vapor pressure and enhancement factor, *J. Appl. Meteor.*, **20**, 1527–1532, 1981.

Busen, R., and U. Schumann, Visible contrail formation nfrom fuels with different sulfur contents, *Geophys. Res. Lett.*, **22**, 1357–1360, 1995.

Byers, .R., J.R. Sievers, and B. Tufts, *Artificial Stimulation of Rain*, Pergamon, pp.47, 1957.

Campos, T.L., A.J. Weinheimer, J. Zheng, D.D. Montzka. J.G. Walega, F.E. Grahek, S.A. Vay, J.E. Collins, Jr., L.O. Wade, G.W. Sachse., B.E. Anderson., W.H. Brune, D. Tan., I. Faloona, S.L. Baughcum, and B.A. Ridley, Measurement of NO and NO_y emission indices during SUCCESS, unpublished, 1997.

Charlson, R.J., S.E. Schwartz, J.M. Hales, R.D. Cess, J.A. Coadley, J.E. Hansen, and D.J. Hofmann, Climate forcing by anthropogenic aerosols, *Science*, **255**, 423–430, 1992.

Chelf, J.H., and S.T. Martin, Laboratory measurements of H_2O vapor pressures and equilibrium freezing temperature of aqueous $(NH_4)_2SO_4$ solution from -30 to 20°C, *Geophys. Res. Lett.*, **26**, 2391-2394, 1999.

Chen, Y., S.M. Kreidenweis, L.M. McInnes, D.C. Rogers, and P.J. DeMott, Single particle analyses of ice nucleating aerosols in the upper troposphere and low stratosphere, *Geophys. Res. Lett.*, **25**, 1391–1394, 1998.

Clegg, S.L., P. Brimblecombe, and A.S. Wexler, Thermodynamic model of the system H^+-NH_4^+-SO_4^{2-}-NO_3^--H_2O at tropospheric temperatures, *J. Phys. Chem.*, **102**, 2137–2154, 1998.

Cooper, W .A., Research in cloud and precipitation physics: review of US theoretical and observational studies, 1987-1990, *Rev. Geophys. Suppl.*, 69–79, 1991.

Cotton, W., Notes for Cloud Physics Class, 1994, Dept. of Atmos. Sci., Colorado St. Univ., Fort Collins.

Cziczo, D.J., J.B. Nowak, J.H. Hu, and J.P.D. Abbatt, Infrared spectrscopy of model tropospheric aerosols as a function of relative humidity: Observation of deliquescence and crystallization, *J. Geophys. Res.*, **102**, 18843–18850, 1997.

Cziczo, D.J., and J.P.D. Abbatt, Deliquescence, efflorescence and supercooling of ammonium sulfate aerosols at low temperature: implications for cirrus cloud formation and aerosol phase in the atmosphere, submitted to *J. Geophys. Res.*, 1998.

DeMott, P.J., Laboratory studies of cirrus cloud processes, In *Cirrus*, edited by David Lynch, Oxford, University Press (in press), 2000.

DeMott, P.J., Y. Chen, S.M. Kreidenweis, D.C. Rogers, and D.E. Sherman, Ice formation by black carbon particles, *Geophy. Res. Lett.*, **26**, 2427-2431, 1999.

DeMott, P.J., D.C. Rogers, S.M. Kreidenweis, and Y. Chen, The role of heterogeneous freezing nucleation in upper tropospheric clouds: Inferences from SUCCESS, *Geophy. Res. Lett.*, **25**, 1387–1390, 1998.

DeMott, P.J., D.C. Rogers, and S.M. Kreidenweis, The susceptibility of ice formation in upper tropospheric clouds to insoluble aerosol components, *J. Geophys. Res.*, **102**, 19,575–19,584, 1997.

DeMott, P.J., A.B. Super, G. Langer, D.C. Rogers, and J.T.McPartland, Comparative characterizations of the ice nucleus ability of AgI aerosols by three methods, *J. Weath. Modif.*, **27**, 1–16, 1995.

DeMott, P.J., M.P. Meyers, and W.R. Cotton, Parameterization and impact of ice initiation processes relevant to numberical model simulations of cirrus clouds, *J. Atmos. Sci.*, **51**, 77–90, 1994.

DeMott, P.J., and D.C. Rogers, Freezing nucleation rates of dilute solution droplets measured between -30°C and -40°C in laboratory simulation of natural clouds, *J. Atmos. Sci.*, **47**, 1056–1064, 1990.

DeMott, P.J., An exploratory study of ice nucleation by soot aerosols, *J. Appl. Meteor.*, **29**, 1072–1079, 1990.

Detwiler, A., Clean-air Seeding, 201pp., Ph.D. dissertation, Department of Atmospheric Science, State University of New York at Albany, 1980.

Diehl, K., and S.K. Mitra, A laboratory study of the effects of a kerosene-burner exhaust on ice nucleation and the evaporation rate of ice crystals, *Atmos. Environ.*, **32**, 3145–3151, 1998.

Ferek, R.J., A.L. Lazrus, and J.W. Winchester, Electron microscopy of acidic aerosols collected over the nonheastern United States, *Atmos. Environ.*, **17**, 1545–1561, 1983.

Fuchs, N.A., The Mechanics of Aerosols, 154pp, Pergamon Press, New York, 1964.

Gorgii, H.W., D. Jost, and W. Vitze, *Ber. Inst. Meteor. U. Geophys.*, **23**, Univerisyt of Frankfurt, Frankfurt, 1971.

Grieken, R.V., and C. Xhoffer, Microanalysis of individual environmental particles: plenary lecture, *J. Anal. At. Spectrom.*, **7**, 81–88, 1992.

Hagen, D.E., M.B. Trueblood, and P.D. Whitefield, A field sampling of jet exhaust aerosol, *Particulate Sci. Technol.*, **10**, 53–63, 1992.

Hagen, D.E., J. Podzimek, A.J. Heymsfield, M.B. Trueblood, and C.K. Lutrus, Potential role of nuclei in cloud element formation at high altitudes, *Atmos. Res.*, **31**, 123–135, 1994.

Hallett, J., Progress in cloud physics 1979-1982, *Rev. Geophys. Space Phys.*, **21**, 965–983, 1983.

Hallett, J. and R.E.J. Lewis, Mother-of-pearl clouds, *Weather*, **22**, 56–65, 1967.

Hanson, D.R., and E.R. Lovejoy, The reaction of $ClONO_2$ with submicrometer sulfuric acid aerosol, *Science*, **267**, 1326–1328, 1995.

Heintzenberg, J., K. Okada, and J. Ström, On the composition of non-volatile material in upper tropospheric aerosol and cirrus crystals, *Atmos. Res.*, **33**, 81–88, 1996.

Heymsfield, A.J., and R.M. Sabin, Cirrus crystal nucleation by momogeneous freezing of solution droplets, *J. Atmos. Sci.*, **46**, 2252–2264, 1989.

Heymsfield, A.J., and L.M. Milosevich, Relative humdity and temperature influences on cirrus formation and evolution: Observations from wave clouds and FIRE II, *J. Atmos. Sci.*, **52**, 4302–4326, 1995.

Heymsfield, A.J., R.P. Lawson, and G.W. Sachse, Growth of ice crystals in a precipitating contrail, *Geophys. Res. Lett.*, **25**, 1335–1338, 1998.

Hinds, W.C., *Aerosol technology: properties, behavior, and measurement of airborne particles*, 483 pages, 2nd ed., New York: Wiley–Interscience, New York, 1999.

Hoffman, D.J., and S. Solomon, Ozone destruction through heterogeneous chemistry following the eruption of El Chichon, *J. Geophys. Res.*, **94**, 5029–5050, 1989.

Houze, R.A., Jr., *Cloud Dynamics*, Academic Press, Inc., San Diego, 1993.

Huffman, P., *Supersaturation dependence of ice nucleation by deposition for silver iodide and natural aerosol.* Ph. D. dissertation, Department of Atmospheric Science, University of Wyoming, 1973.

Ikegami, M., K. Okada, Y. Zaizen, and Y. Makino, Aerosol particles in the middle troposphere over the Northwestern Pacific, *J. Meteor. Soc. Jpn.*, **71**, 517–528, 1993.

Imre, D.G., J. Xu, and A.C. Tridico, Phase transformations in sulfuric acid aerosols: Implications for stratospheric ozone depletion, *Geophys. Res. Lett.*, **24**, 69–72, 1997.

Isaac, G.A., and P.H., Daum, Winter study of air, cloud and precipitation chemistry in Ontario, Canada, *Atmos. Environ.*, **21**, 1587–1600, 1987.

Jensen, E.J., O.B. Toon, S. Kinne, G.W. Sachse, B.E. Anderson, K.R. chan, C.H. Twohy, B. Gandrud, A.J. Heymsfield, and R.C. Miake-Lye, Environmental conditions required for contrail formation and persistence, *J. Geophys. Res.*, **103**, 3929–3936, 1998.

Jensen, E.J., O.B. Toon, D.L. Westphal, S. Kinne, and A.J. Heymsfield, Microphysical modeling of cirrus 1. Comparison with 1986 FIRE IFO measurements, *J. Geophys. Res.*, **99**, 10,421–10,442, 1994.

Kächar, B., Physicochemistry of aircraft-generated liquid aerosol, soot, and ice particles, 1, Model description, *J. Geophys. Res.*, **103**, 17111–17128, 1998.

Kächar, B., Aircraft-generated aerosols and visible contrails, *Geophys. Res. Lett.*, **23**, 1933–1936, 1996.

Khvorostyanov, V. and K. Sassen, Toward the theory of homogeneous nucleation and its parameterization for cloud models, *Geophys. Res. Lett.*, **25**, 3155–3158, 1998.

Kikuchi, K., M. Murakami, and Y. Sanuki, Preliminary measurements of the center nucleus of snow crystals using and energy dispersive X-ray microanalyzer, *Proceeding of the 4th Symposium on Polar Meteorology and Glaciology*, Memoirs of National Institute of Polar Research Special Issue, **No. 24**, 157–174, 1982.

Koop, T, H.P. Ng, L.T. Molina, and M.J. Molina, A new optical technique to study aerosol phase transitions: the nucleation of ice from H_2SO_4 aerosol, submitted to *J. Phys. Chem.*, 1998.

Koop, T., A.K. Bertram, L.T. Molina, and M.J. Molina, Phase transitions in aqueous NH_4HSO_4 solutions. Submitted to *J. Phys. Chem.*, 1999.

Kramer, B., *Freezing of single levitated micro-droplets of water, sulfuric acid and ternary $H_2SO_4/HNO_3/H_2O$ solutions*, Ph.D. Dissertation, Dept. of Physics, Frie Univ. of Berlin, 183 pp., 1998.

Kreidenweis, S.M., Y. Chen, D.C. Rogers, and P.J. DeMott, Isolating and identifying atmospheric ice-nucleating aerosols: A new technique, *Atmos. Res.*, **46**, 263–278, 1998.

Kumai, M., Identification of nuclei and concentrations of chemical species in snow crystals sampled at the South Pole, *J. Atmos. Sci.*, **33**, 833–841, 1976.

Liou, K.N., Influence of cirrus clouds on weather and climate processes: A global perspective, *Mon. Weath. Rev.*, **114**, 1167–1199, 1986.

Maenhaut, W., and W.H. Zoller, Determination of the chemical composition of the south pole aerosol by instrumental neutron activation analysis, *J. Radioanal. Chem.*, **37**, 637–650, 1997.

Maenhaut, W., G. Ducastel, C. Leck, E.D. Nilsson, and J. Heintzenberg, Multi-elemental composition and sources of the high Arctic atmospheric aerosol during summer and autumn, *Tellus*, **48B**, 300–321, 1996.

Martin, S.T., Phase Transformations of the ternary system $(NH_4)_2SO_4$ -H_2SO_4-H_2O and the implications for cirrus cloud formation, *Geophys. Res. Lett.*, **25**, 1657–1660, 1998.

McInnes, L.M., D.S. Coven, and B.M. Baker, The number of sea-salt, sulfate, and carbonaceous particles in the marine atmosphere: EM measurements consistent with the ambient size distribution, *Tellus*, **49B**, 300–313, 1997.

Middlebrook, A.M., D.S. Thomson, and D.M. Murphy, On the purity of laboratory-generated sulfuric acid droplets and ambient particles studied by laser mass spectrometry, *Aerosol Sci. and Technol.*, **27**, 293–307, 1997.

Murakami, M., and K. Kikuchi, Some considerations on the center nuclei of snow crystals, *Proceeding of the 4th Symposium on Polar Meteorology and Glaciology*, Memoirs of National Institute of Polar Research Special Issue, **No. 24**, 175–183, 1982.

Murphy, D.M., D.S. Thomson, and M.J. Mahoney, Organics, meteoritic material cercury, and other elements in high altitude aerosols, *Science*, **282**, 1664–1669, 1999.

Omega Co., *Temperature handbook*, **vol. 28**, pp. H4, 1994.

Podzimek, J., D.E. Hagen, and E. Robb, Large aerosol particles in cirrus type clouds, , bf 38, 263–282, 1995.

Pruppacher, H.R., and J.D. Klett, *Microphysics of Clouds and Precipitation*, Kluwer Acadcmic Publishers, Boston, 954pp, 1997.

Pruppacher, H.R., A new look at homogeneous ice nucleation in supercooled water drops, *J. Atmos. Sci.*, **52**, 1924–1933, 1995.

Pueschel, R.F., S. Verma, G.V. Ferry, S.D. Howard, S. Vay, S.A. Kinne, J. Goodman, and A.W. Strawa, Sulfuric acid and soot particle formation in aircraft exhaust, *Geophys. Res. Lett.*, in press, 1997 .

Pueschel, R.F., Stratospheric aerosols: Formation, properties, effects, *J. Aerosol Sci.*, **27**, 383–402, 1996.

Pueshel, R.F., K. Boering, S. Verma, S.D. Howard, G.V. Ferry, J. Goodman, D.A. Allen, and P. Hamill, Soot aerosol in the lower stratosphere: Pole-to-pole variability and contributions by aircraft, *J. Geophys. Res.*, , 1995.

Pueschel, R.F., D.F. Blake, K.G. Snetsinger, A.D.A. Hanse, S. Verma, and K. Kato, Black carbon (soot) aerosol in the lower stratosphere and upper troposphere, *Geophys. Res. Lett.*, **19**, 1659–1662, 1992.

Reiter, E.R., W. Carnuth, H.J. Kanter, K. Pötzl, R. Reiter, and R. Sladkovic, Measurements of stratospheric residence time, *Arch. Meteorol. Geophys. Bioklimatol. Ser. A*,,**24**, 41–51, 1975a.

Reiter, R., R. Sladkovic, and K. Pötzl, Die wichtigsten chemischen Bestandteile des Aerosol uber Mitteleuropa unter Reinluftbedingungen in 1800 m Seehohe, *Meterol Rundsch.*, **28**, 37–55, 1975b.

Reiter, R., R. Sladkovic, and K. Pötzl, Chemical components of aerosol particles in the lower troposphere above central Europe measured under pure-air conditions, *Atmos. Environ.*, **10**, 841–853, 1976.

Reiter, R., R. Sladkovic, and K. Pötzl, Chemische Komponente des Reinluftaerosols in Abhangigkeit von Luftmassenchrakter und meterologischen Bedingungen, *Ber. Bunsen-Ges. Phys. Chem.*, **82**, 1188–1193, 1978.

Rogers, D.C., P.J. DeMott, S.M. Kreidenweis, and Y. Chen, Measurements of ice nucleating aerosols during SUCCESS, *Geophys. Res. Lett.*, **25**, 1383–1386, 1998.

Rogers, D.C., Detecting ice nuclei with a continuous flow diffusion chamber: Some exploratory texts of instrument response, *J. Atmos. Ocean. Tech.*, **11**, 1042–1047, 1994.

Rogers, D.C., Measurements of natural ice nuclei with a continuous flow diffusion chamber, *Atmos. Research*, **29**, 209–228, 1993.

Rogers, D.C., Development of a continuous flow thermal gradient diffusion chamber for ice nucleation studies, *Atmos. Res.*, **22**, 149–181, 1988.

Rogers, D.C., *Field and laboratory studies of ice nucleation in winter orographic clouds*, Ph.D dissertation, Department of Atmospheric Science, University of Wyoming, 1982.

Rosinski, J., and P.L. Haagenson, Ice-forming nuclei of maritime origin, *J. Aerosol Sci.*, **17**, 23–46, 1986.

Rosinski, J., P.L. Haagenson, C.T. Nagamoto, and F. Parungo, Nature of ice-forming nuclei in marine air masses, *J. Aerosol Sci.*, **18**, 291–309, 1987.

Rosinski, J., and G. Morgan, Cloud condensation nuclei as a source of ice-forming nuclei in clouds, *J. Aerosol Sci.*, **22**, 123–133, 1991.

Rucklidge, J., The examination by electron microscope of ice crystal nuclei from cloud chamber experiments, *J. Atmos. Sci.*, **22**, 301–308, 1965.

Sassen, K., D. O'C. Starr, G.G. Mace, M.R. Poellot, S.H. Melfi, W.L. Eberhard, J.D. Spinhirne, E.W. Eloranta, D.E. Hagen, and J. Hallett The 5-6 December 1991 FIRE IFO II jet stream cirrus case study: Possible influences of volcanic aerosols, *J. Atmos. Sci.*, **52**, 97–123, 1995.

Sassen, K., and G.C. Dodd, Homogeneous nucleation rate for highly supercooled cirrus cloud droplets, *J. Atmos. Sci.*, **45**, 1357–1369, 1988.

Schumann, U., J. Storm, R. Busen, R. Baumann, K. Gierens, M. Krutstrunk, F.P. Schroder, and J. Sting, In situ observations of particles in jet aircraft exhausts and contrails for different sulfur-containing fuels, *J. Geophys. Res.*, **101**, 6853–6869, 1996.

Sheridan, P.J., C.A. Brock, and J.C. Wilson, Aerosol particles in the upper troposphere and lower stratosphere: Elemental composition and morphology of individual particles in northern mid-latitudes, *Geophys. Res. Lett.*, **21**, 2587–2590, 1994.

Sheridan, P.J., Characterization of size segregated particles collected over Alaska and the Canadian high Arctic, AGASP-II flights 204-206, *Atmos. Environ.*, **23**, 2371–2386, 1989.

Skoog, D.A., D.M. West, and F.J. Holler, *Fundamentals of Analytical Chemistry*, 7th. ed., pp. 22, Fort Worth, Saunders College Pub., 1996.

Song, N., and D. Lamb, Experimental investigations of ice in supercooled clouds: II. Scavenging of an insoluble aerosol, *J. Atmos. Sci.*, **51**, 104–116, 1994.

Ström, J., B. Strauss, T. Anderson, F. Schroder. J. Heintzenberg, and P. Wendling, In-situ observations of the microphysical properties of young cirrus clouds, *J. Atmos. Sci.*, in. press, 1997.

Ström, J., J. Heintzenberg, K.J. Noone, K.B. Noone, J.A. Orgen, F. Albers, and M. Quante, Small crystals in cirriform clouds: A case study of residue size distribution, cloud water content and related cloud properties, *Atmos. Res.*, **32**, 125–141, 1994.

Szyrmer, W., and I. Zawadzki, Biogenic and Anthropogenic sources of ice-forming nuclei: A review, *Bull. American Meteor. Soc.*, **78**, 209–228, 1997.

Tabazadeh, A., and O.B. Toon, The role of ammoniated aerosols in cirrus cloud nucleation, *Geophys. Res. Lett.*, **25**, 1379–1382, 1998.

Talbot, R.W., J.E. Dibb, and M.B. Loomis, Influence of vertical transport on free tropospheric aerosols over the central USA in spingtime, *Geophys. Res. Lett.*, **25**, 1367–1370, 1998.

TSI Incorp., *TSI 3071 Instruction Manual*, St. Paul, Minnesota, September 1994.

TSI Incorp., *TSI 3010 Instruction Manual*, St. Paul, Minnesota, September 1994.

Twohy, C.H., and B.W. Gandrud, Electron microscope analysis of residual particles from aircraft contrails, *Geophys. Res. Lett.*, **25**, 1359–1362, 1998.

Twomey, S., *J. Meteor.*, **12**, 81, 1955.

Vali, G., Ice nucleation–A review, *The 14th Int. Conf. On Nucl and Atmos. Aerosol*, Helsinki, Elsevier, Oxford., pp. 271-279, 1996.

Warneck, P., *Chemistry of the Natural Atmosphere*, 382pp, Academic Press, Inc., San Diego, 1988.

Weinheimer, A. J., T.L. Campos, and B.A. Ridley, The in-flight sensitivity of gold-tube NO_y converters to HCN, *Geophys. Res. Lett.*, **25**, 3943–3945, 1998.

Wiedensohler, A., An approximation of the Bipolar Charge Distribution for particles in the submicron size range, *J. Aerosol Sci.*, **19**, 387–389, 1988.

Willeke, K., and P.A. Baron, *Aerosol measurement: Principles, technique, and applications*, Van Nostrand Reinhold, New York, 1993.

Yamato, M., and A. Ono, Chemical and physical properties of stratospheric aerosol particles in the vicinity of tropopause folding, *J. Meteorol. Soc. Jpn.*, **67**, 147–165, 1989.

Yao, Y., M. Massucci, S.L. Clegg, and P.J. Brimblecombe, Equilibrium water partial pressures and salt solubilities in aqueous $(NH_4)_2SO_4$ to low temperatures, *J. Phys. Chem.*, **103**, 3678-3686, 1999.

Young, K.C., *Microphysical Processes in Clouds*, Oxford University Press, New York, 1993.

Young, K.C., The role of contact nucleation in ice phase initiation in clouds, *J. Atmos. Sci.*, **31**, 768–776, 1974.